Too big to grow: self-consistent model for nonlinear saturation in open shear flows

PAR

Vladislav MANTIČ LUGO

To my parents,
to whom I owe everything I am today,

and to my brother,
who has been my soul mate since my earliest memories.

Acknowledgements

It was a sunny day at the end of summer 2011 when I started the journey of my PhD. A huge horizon of possibilities was opening in front of me and I did not know what the future would offer, but I knew that I wanted to work with François, and that EPFL and Lausanne would be my home at least for a while. Since then, for the next four years, life has been full of new and exciting moments – many funny, cheerful and happy, some stressful and hard. However, what made this journey so remarkable are the amazing people I met along these years. To all of them, from whom I learned so much and who helped me to achieve the completion of this work, I would like to express my deepest acknowledgement.

My most sincere gratitude goes to François; for his trust accepting me as part of the early expansion of the LFMI, for his guidance, for his unconditional support and continuous motivation. I would like to thank him for his infinite patience, for his positive attitude during the downs as for his cheerful excitement in the ups and for his advice during the preparation of papers. I admire his vast knowledge of science and fluid dynamics, as well as his love for research. I learned from him not only the complexity of science, but also about life and how to be a better person. Distinctly, I want to thank him for the super-inspiring discussions that helped me to achieve the best results.

I would like to acknowledge Laurette Tuckerman, Benoît Pier and Tobias Schneider for spending the time reading in detail the thesis and for the very profound discussion during the thesis defense. Also I want to thank Dominique Pioletti for presiding over the jury.

I would like to thank Philippe Meliga for the motivating and insightful discussions we had at the early stages of my thesis, Pierre-Yves Lagrée for showing me the secrets of boundary layers, and Jérôme Hoepffner for its enlightening view in different subjects. I want to acknowledge my fluid dynamics professors José Manuel Gordillo, Miguel Pérez-Saborid and Antonio Barrero, for the wonderful lectures they gave me and their ability to create in me such an interest in fluids dynamics. I am grateful to Miguel Fosas de Pando for guiding me in the quest for a PhD.

I would like to thank all the people in the LFMI for their always open and supportive attitude. In particular, I want to acknowledge those who directly helped me during the difficult moments of the project: Cristóbal for his immense support during the project development, for his insightful theoretical discussions about fluids but also for the controversial debates about society, economics, research and particularly for his relaxed and positive viewpoint; Andrea and Edouard for their always available help with the intricacies of programming with FreeFem; Marc-Antoine for his knowledge in numerical simulations; PT for showing me an effective and a practical approach to research and the tricks of illustrator and experiments; Francesco for

Acknowledgements

Abstract

Open flows, such as wakes, jets, separation bubbles, mixing layers, boundary layers, etc., develop in domains where fluid particles are continuously advected downstream. They are encountered in a wide variety of situations, ranging from nature to technology. Such configurations are characterised by the development of strong instabilities resulting in observable unsteady dynamics. They can be categorised as oscillators which present intrinsic dynamics through self-sustained oscillations, or as amplifiers, which exhibit a strong sensitivity to external disturbances through extrinsic dynamics. Over the years, different linear and nonlinear approaches have been adopted to describe the dynamics of oscillators and amplifiers. However, a simplified physical description that accurately accounts for the nonlinear saturation of instabilities in oscillators as well as that of the response to disturbances in stable amplifier flows is still missing.

In this thesis, this question is addressed by introducing a self-consistent semi-linear model. The model is formally constructed by a set of equations where the mean flow is coupled to a linear perturbation equation through the Reynolds stress. The full nonlinear fluctuating motion is thus approximated by a linear equation. The nonlinear dynamics of oscillators is studied in the cylinder wake, where the most unstable eigenmode of finite amplitude is coupled to the instantaneous mean flow for different oscillation amplitudes. This family of solutions provides an instantaneous mean flow evolution as a function of an equivalent slow time. A transient physical picture is formalised, wherein a harmonic perturbation grows and changes the amplitude, frequency, growth-rate and structure due to the modification of the instantaneous mean flow by the Reynolds stress forcing. Eventually this perturbation saturates when the flow is marginally stable. In contrast to standard linear stability analysis around the mean flow, the iterative solution of the model provides *a priori* an accurate prediction of the instantaneous amplitude, frequency and growth rate, as well as the flow fields, without resorting to any input from numerical or experimental data.

Regarding noise amplifiers, the nonlinear saturation of the large linear amplification to external disturbances is studied in the framework of the receptivity analysis of the backward facing step flow. The self-consistent model is first introduced for harmonic forcing and later generalised to stochastic forcing by reformulating it conveniently in frequency domain. The results show an accurate prediction of the response energy as well as the flow fields. Hence, a similar picture is revealed, wherein the Reynolds stress dominates the saturation process. Despite the difference in the dynamics of the described flows, they share the same nonlinear saturation mechanism: the mean flow distortion.

Acknowledgements

Résumé

Les écoulements ouverts, tels que les sillages, jets, bulles de séparation, les couches de mélange, les couches limites, etc., se développent dans les domaines où les particules de fluide sont advectées en aval. On les rencontre dans une grande variété de situations, allant de la nature à la technologie. De telles configurations sont caractérisées par le développement de fortes instabilités résultant en une dynamique instationnaire. Les écoulements peuvent être divisés en deux classes : les oscillateurs qui présentent une dynamique intrinsèque à travers des oscillations auto-entretenues, et les amplificateurs, qui présentent une forte sensibilité aux perturbations extérieures à travers une dynamique extrinsèque. Au fil des ans, différentes approches linéaires et non linéaires ont été adoptées pour décrire la dynamique des oscillateurs et des amplificateurs. Toutefois, une description physique simplifiée qui représente de façon précise la saturation des instabilités non linéaires dans les oscillateurs, ainsi que celle de la réponse à des perturbations dans les écoulements stables, comme les amplificateurs, manque encore à ce jour.

Dans cette thèse, cette question est abordée par l'introduction d'un modèle semi-linéaire auto-cohérent couplé. Le modèle est formellement construit par un ensemble d'équations où l'écoulement moyen instantané est couplé à une équation de perturbation linéaire à travers le tenseur de Reynolds. Le champ de vitesse fluctuant nonlinéaire est donc approximé par une équation linéaire. La dynamique d'un oscillateur nonlinéaire est étudiée.

Le sillage d'un cylindre est étudié comme prototype d'oscillateur non-linéaire, où le mode propre le plus instable est couplé pour différentes amplitudes finies. Cela fournit une variation quasi-statique de l'écoulement moyen instantané en fonction d'un temps lent équivalent. Une image physique transitoire est formalisée, dans laquelle une perturbation harmonique grandit et change d'amplitude, de fréquence, de taux de croissance et de structure en raison de la modification du champ moyen instantané par le forçage du tenseur de Reynolds. Cette perturbation sature finalement lorsque le écoulement moyen est marginalement stable. Contrairement à l'analyse de stabilité linéaire standard autour de l'écoulement moyen, la solution itérative du modèle fournit *a priori* une prédiction précise de l'amplitude instantanée, de la fréquence et du taux de croissance, ainsi que des champs d'écoulement, sans avoir recours à des données simulées ou expérimentales.

En ce qui concerne les amplificateurs de bruit, la saturation nonlinéaire de la forte amplification à des perturbations externes est étudiée dans le cadre de l'analyse de la réceptivité de l'écoulement sur une marche descendante. Le modèle auto-cohérent est d'abord introduit pour un forçage harmonique et ensuite généralisé à un forçage stochastique, en le reformulant

Contents

Contents

1 Introduction

1.1 Open flows

Open flows are characterised by fluid particles continuously advected downstream; entering and leaving the fluid domain. A common feature of open flows is that they present strong instabilities (Drazin & Reid (1981); Drazin (2002); Chomaz (2005); Charru (2011)). The concept of stability of a physical state of a system was clearly expressed already back in the nineteenth century by Clerk Maxwell (see Campbell & Garnett (1882)).

> [...] When the state of things is such that an infinitely small variation of the present state will alter only by an infinitely small quantity the state at some future time, the condition of the system, whether at rest or in motion, is said to be stable; but when an infinitely small variation in the present state may bring about a finite difference in the state of the system in a finite time, the condition of the system is said to be unstable. [...]

Therefore, the unstable nature of open flows yields a high sensitivity to perturbations that results in an unobservable unstable steady state (Drazin (2002)), and an observable unsteady dynamics with time varying coherent structures that eventually evolve into turbulence.

Open flows encompass many different configurations, i.e. wakes, jets, separation bubbles, mixing layers, Poiseuille flow, Couette flow, boundary layers, and also Rayleigh-Benard convection with through flow or Taylor-Couette flow with axial advection. These archetypes characterise open flows that are encountered in a wide variety of situations, ranging from nature to technology. Some examples of unstable open flows that we can find in nature are the shear layer instability that appears due to wind cross flow as visualised by clouds in Fig. 1.1(a) or the well known von-Karman vortex street that appears due to a strong wind passing around an island as visualised by clouds in Fig. 1.1(b). Other examples are found in flows passing around basic geometrical shapes like the von-Karman vortex street that appears in the flow around a cylinder illustrated in Fig. 1.1(c) or the flow around a sphere depicted in Fig. 1.1(d). These simplified configurations serve as canonical study cases that are used to describe and
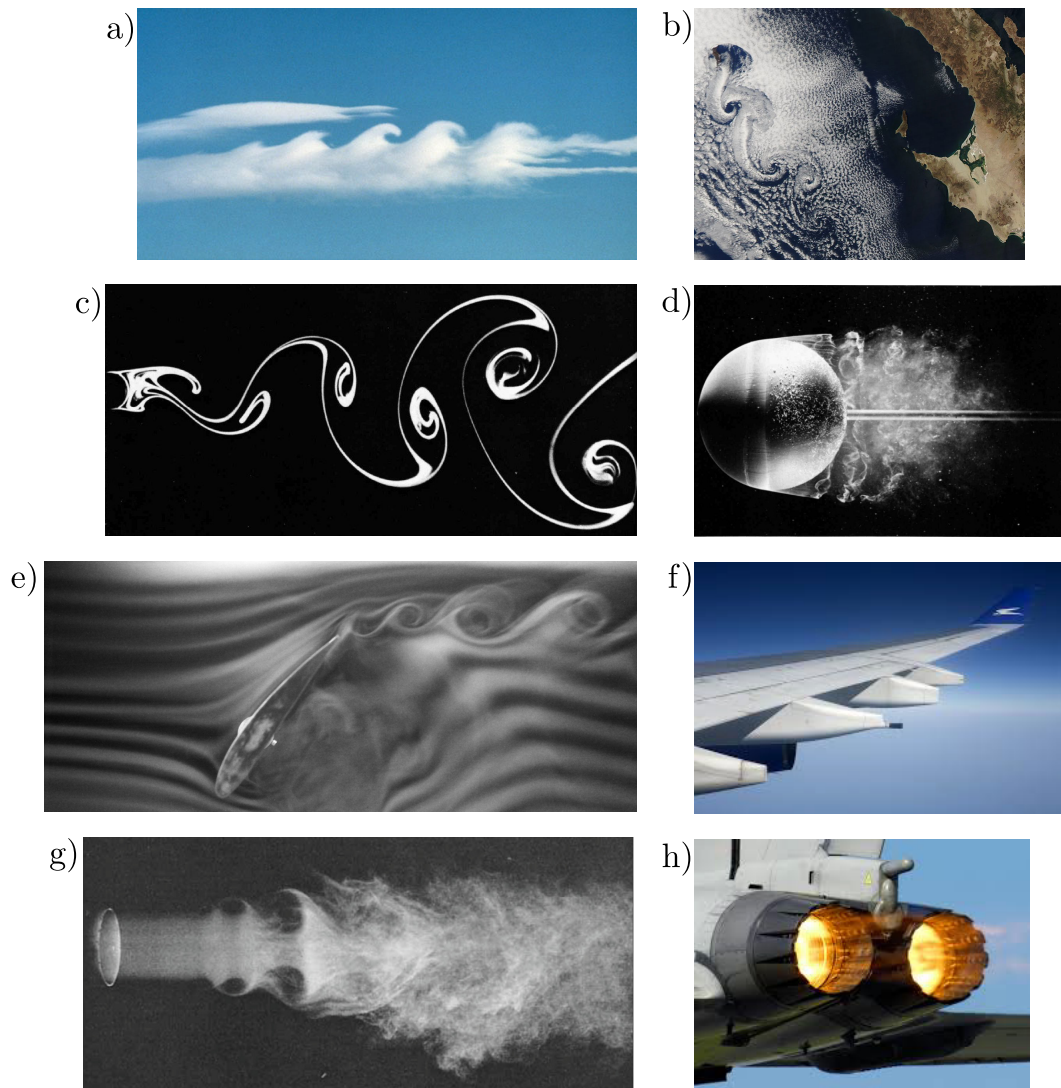
Figure 1.1 – Open flows in nature and technology. (a) Cloud visualisation of a shear layer flow. (b) Von-Karman vortex street visualised by clouds around an island. (c) Unstable flow around a cylinder, the Von-Karman vortex street is visualised by dye (Sadatoshy Taneda in Van Dyke (1988)). (d) Flow passing around a sphere (Werle (1980); Van Dyke (1988)). (e,f) Smoke visualisation Unstable separated flow around an airfoil (GmbH (2010)) with industrial application in wings. (g,h) Smoke visualisation of a jet flow (Crow & Champagne (1971)) with industrial application in turbojets.

understand the physical behaviour of the flow in more complex geometries encountered in practical problems like the flow around an airfoil illustrated in Fig. 1.1(e,f) or the jet flow shown in Fig. 1.1(g,h) .

The ubiquitous nature of these flows highlights the importance of understanding their dynamics. The description of the dynamics should consider:

- the spatial evolution of the base or mean flow (in general inhomogeneous)

- the perturbations introduced

- the evolution and advection of the perturbations

- the control of the instability, what enhances or reduces the unstable behaviour

- the nonlinearities involved intrinsic to the Navier-Stokes equations (NSE)

among others (Chomaz (2005)). These are some of the questions that need to be addressed in order to improve the prediction of natural phenomena as well as to control the flow behaviour, advantageous for technology development.

1.2 Linear dynamical characterisation and non-normality in open flows

Open flows characterised by their unstable nature can be categorised as oscillators, which present intrinsic dynamics (self-sustained oscillations), or as amplifiers, which exhibit a strong sensitivity to external disturbances through extrinsic dynamics (noise driven perturbations) (Chomaz (2005); Huerre & Monkewitz (1990)). The dynamical analysis of the evolution of the perturbations can be approached from two different point of views, either local, at each streamwise location or global, in the whole domain.

Local stability analysis

The local point of view is natural for weakly nonparallel flows which assume a steady base or mean flow that varies slowly on a long length scale when compared to the shorter instability waves (Schmid & Henningson (2001); Chomaz (2005); Charru (2011)). Then, locally at each streamwise station of the slowly varying steady base flow, the evolution of the perturbation is represented as a superposition of instability waves of the associated parallel (homogeneous) base flow, illustrated in Fig. 1.2 (Drazin & Reid (1981)). Therefore, the linear stability at each station is based on the evolution of the response to an impulse perturbation of the linearised equations that describe the flow dynamics. This response exhibits three different types of behaviour as illustrated in Fig. 1.3 . The flow is *linearly stable* when any infinitesimal perturbation decays in time to zero for $t \to \infty$ (Fig. 1.3(a)). Otherwise, if the infinitesimal perturbation grows then the flow is *linearly unstable*. For an unstable flow two types of instability can be distinguished, formalised as *absolute* and *convective* instability, depending on the competition between the local instability and the basic advection (Bers (1975); Huerre & Monkewitz (1985)). A flow is *convectively unstable* when the perturbation, in addition to being amplified, is advected downstream and moves far from the initial point (Fig. 1.3(b)). In this case the advection of the base flow is stronger than the instability growth. On the other hand, a flow is *absolutely unstable* when the impulse grows to infinity at the initial location due to a stronger growth of the instability than the advection (Fig. 1.3 (c)).
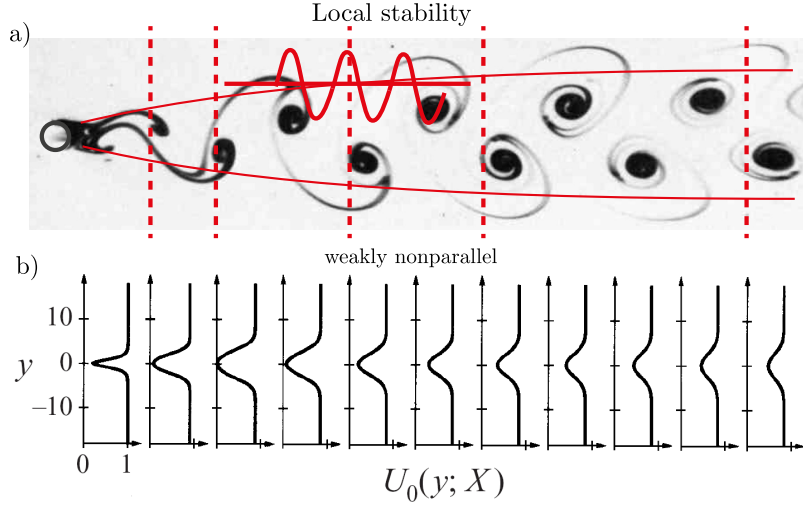
Figure 1.2 – Local stability analysis studies the development of instability waves independently at each station in the streamwise direction assuming a parallel base flow $U_0(y; X)$. (a) Wake behind a cylinder at $Re = 105$ (experiment of Sadatoshy Taneda illustrated in Van Dyke (1988)). (b) Synthetic weakly nonparallel wake to model real wakes (Pier & Huerre (2001)).
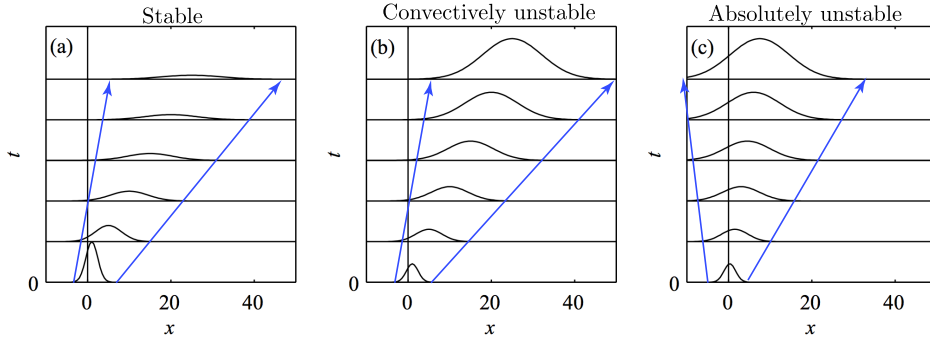
Figure 1.3 – Evolution in the space-time plane (x, t) of a perturbation located close to $x = 0$ at time $t = 0$, for a one dimensional base state with positive advection from left to right. The base flow is (a) stable; (b) convectively unstable; (c) absolutely unstable. Image extracted and modified from (Charru (2011)).

Global stability analysis

In the global approach the instabilities and the base flow have no separated length scales and the dynamics of the perturbation result from the interactions between global modes extended over the whole physical domain. The global behaviour of the flow depends on the interactions of the local behaviour of different zones; stable, convective or absolutely unstable. Thus an open flow can be globally stable but locally convectively unstable, since perturbations are continuously advected while growing (see Fig. 1.4(b)). Such flows behave as amplifiers with no intrinsic instability and presenting high sensitivity to external forcing (Chomaz (2005); Schmid (2007)). An example of an amplifier is the jet flow, as illustrated in

Fig. 1.1(g) and Fig. 1.4(b) where small harmonic excitations result in large coherent structures (Crow & Champagne (1971)). In contrast, a globally unstable flow will present a large enough region of local absolute instability (see Fig. 1.4(a)). In general, this kind of open flow displays intrinsic nonlinear dynamics and develops self-sustained oscillations, (Huerre & Monkewitz (1985); Chomaz *et al.* (1988); Chomaz (2005)), for example, the flow behind a cylinder. This resonance results in a clear peak in the frequency spectrum of the flow in the wake representing the frequency of the vortex shedding (see Fig. 1.4(c)). In contrast, amplifiers present a broad frequency spectrum without any specific frequency selection (Nichols & Lele (2010)); however, there is a frequency region where the external noise amplification is stronger as appreciated in Fig. 1.4(d).

Traditionally, linear stability analysis is concerned with a quantitative description of the flow dynamics involving the evolution to the infinite time horizon of the perturbations. The description of this long term behaviour is inferred from the eigenvalues and eigenmodes of the linear operator $\mathscr{L}$, that is obtained from the linearised Navier-Stokes equations around a steady solution or base flow. The operator $\mathscr{L}$ governs the linear dynamics of the flow formalised as

$$\frac{d\boldsymbol{u}}{dt} = \mathscr{L}\boldsymbol{u},\tag{1.1}$$

where $\boldsymbol{u}$ is the state vector of the flow field. The modal analysis is able to predict the onset of instabilities in supercritical flows or oscillators, when a dominant unstable eigenmode appears. The unstable mode describes the initial structure and frequency of the perturbation as it starts growing (see Fig. 1.4(e) (Theofilis (2011))), before its amplitude is too big and nonlinear interactions start to be important (Barkley (2006)). However, modal analysis fails to describe the dynamics of stable flows like amplifiers showing stable spectrum with no predominant eigenmodes (see Fig. 1.4 (f) and Garnaud *et al.* (2013)). The amplifying potential of these flows is best understood by drawing attention to the non-normality of the linear operator $\mathscr{L}$, produced by the strong streamwise advection of the base flow, or steady solution of NSE. This feature dictates the nature of the dynamics in self-sustained oscillators and noise amplifiers.

Non-normality

Recently it started to become clear that for non-normal linear operators, the spectrum is not sufficient to characterise the dynamics of the flow (Farrell & Ioannou (1996); Trefethen *et al.* (1993); Schmid & Henningson (2001); Chomaz (2005); Schmid (2007)). It is well known that since the eigenmode basis is not orthogonal, then even for a stable operator, whose eigenmodes all decay in time, small initial perturbations may experience very large transient growth. The time evolution of the perturbations is dictated by the solution of the homogeneous equation (1.1) under initial perturbations. Therefore, the dynamics of the least stable mode is in many cases entirely irrelevant to the temporal behaviour of the linear system at finite time.
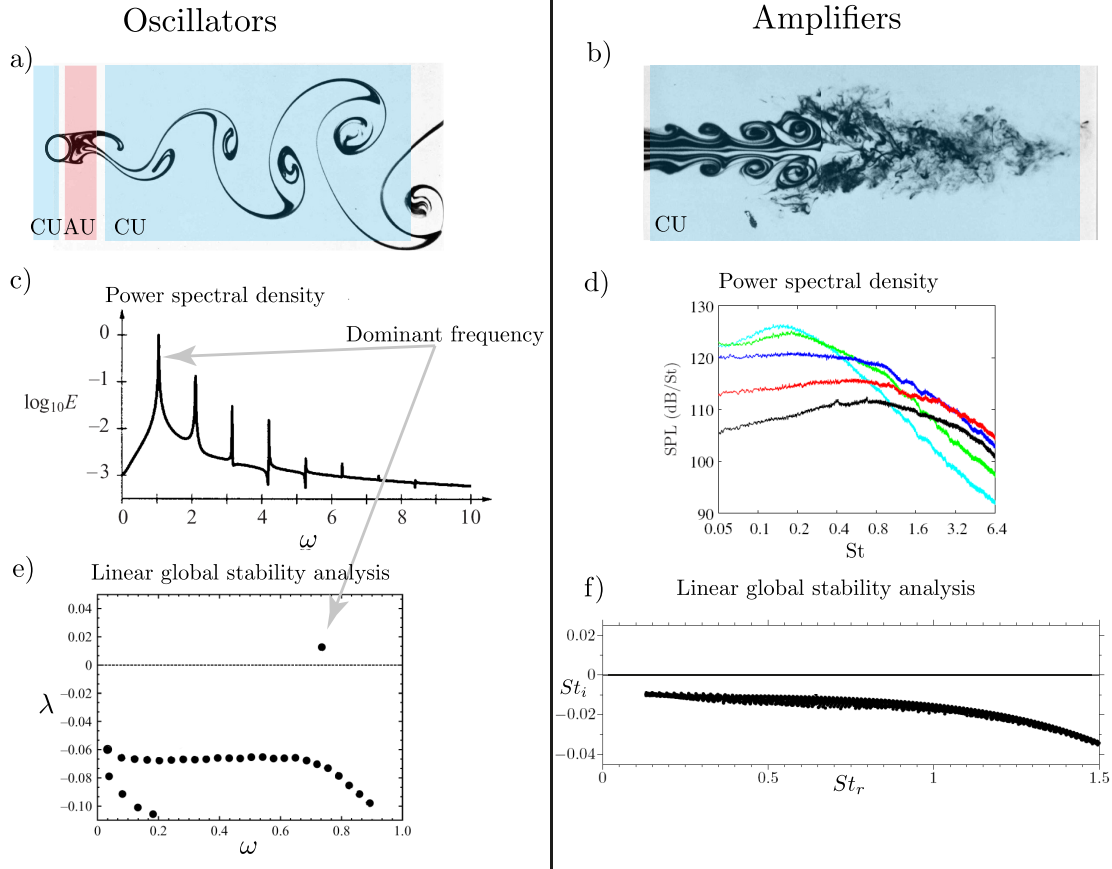
Figure 1.4 – Comparison of oscillators and amplifiers in their main characteristics. (a) Absolute (AU) and convectively (CU) unstable regions in an oscillator, there is a large enough absolutely unstable region to present global instability as in the flow around a cylinder for Re=140 (figure modified from Van Dyke (1988)). (b) Amplifiers present a convectively unstable region that amplifies strongly external noise even for a globally stable flow as in a turbulent jet (figure modified from Van Dyke (1988)). (c) Power spectral density function extracted from a signal in the cylinder wake, showing a clear peaked frequency associated to the von-Karman vortex street (Pier (2002)). (d) Power spectral density function extracted from a signal in a turbulent jet, showing a response to noise in a preferred region in frequency (Barré *et al.* (2006)). (e) Global linear stability analysis around an unstable base flow in the cylinder flow showing a clear unstable mode. (f) Global linear stability on the mean flow of a turbulent jet showing a flat stable spectrum without any unstable mode (Nichols & Lele (2010)).

Consequently one of the standard approaches to characterise the dynamics in amplifiers is to look at initial disturbances which lead to the maximum growth and follow the evolution of these perturbations in time. The maximally amplified initial conditions are described by the leading singular vectors of the time propagator $e^{\mathscr{L} t}$, (Trefethen *et al.* (1993); Farrell & Ioannou (1996); Schmid & Henningson (2001); Schmid (2007)).

Furthermore, non-normality leads also to an extreme sensitivity to forcing. This forcing can

be created due to different sources like free-stream turbulence, wall roughness, or other non-smooth geometries, body forces, or even neglected terms, such as nonlinearities. The response to harmonic forcing at frequency ω is governed by the resolvent operator $\mathscr{R} = (i\omega I + \mathscr{L})^{-1}$ for a stable $\mathscr{L}$. It corresponds to the particular solution of the linear equation

$$\frac{d\boldsymbol{u}}{dt} = \mathscr{L}\boldsymbol{u} + \boldsymbol{f}e^{i\omega t}, \tag{1.2}$$

forced by $\boldsymbol{f}$. When $\mathscr{L}$ is non-normal the response to forcing is much larger than the least damped eigenvalue and is given by its pseudospectrum (Schmid & Henningson (2001); Chomaz (2005); Schmid (2007); Farrell & Ioannou (1996)). In addition, the spatial structure of the response does not resemble the shape of the forcing. The strong sensitivity to noise in amplifiers is thus interpreted by the non-normality of the operator $\mathscr{L}$. The study of the response to forcing or receptivity analysis is common for noise amplifiers, for which one of the relevant procedures is to find the optimal harmonic forcing structures that at frequency ω lead to the most energetic responses. The optimal forcing and corresponding response structures are provided by the singular vector of the resolvent operator $\mathscr{R}$, as described in Farrell & Ioannou (1996); Schmid (2007); Garnaud *et al.* (2013); Dergham *et al.* (2013); Boujo & Gallaire (2015) among others.

Large transient growth and response to forcing are thus interpreted by the non-normality of the operator $\mathscr{L}$, whose direct eigenmodes are not orthogonal to each other and whose direct and adjoint normal bases do not coincide (Chomaz (2005); Marquet *et al.* (2009); Schmid (2007)). The non-normal behaviour can be characterised by two different physical mechanisms (Marquet *et al.* (2009)). The lift-up non-normality differentiates the direct and adjoint modes by their components: the direct is dominated by the streamwise component and the adjoint by the cross-stream component, common in parallel flows. The convective non-normality results in a different localisation of the direct and adjoint global modes, downstream and upstream respectively.

Finally, the non-normality of the linear operator $\mathscr{L}$ creates a large sensitivity of its spectrum to perturbations in the operator, $\Delta\mathscr{L}$. In other words, small perturbations in the operator $\Delta\mathscr{L}$ may induce very large variations in the spectrum (Trefethen *et al.* (1993); Schmid & Henningson (2001); Chomaz (2005)). Therefore, small variations in the base flow around which the linear operator $\mathscr{L}$ has been computed may create large variations in the linear dynamics, arguing for the importance of sensitivity analysis (e.g.Bottaro *et al.* (2003)), which is also relevant for flow control (Camarri (2015)).

As a final note, the strong noise sensitivity coupled to the sensitivity of the linear operator to perturbations legitimise the relevance of nonlinear studies. In other words, small disturbances in the flow may lead to large responses which modify the base state around which the linear operator $\mathscr{L}$ has been computed, and thus varying the spectrum of the non-normal operator $\mathscr{L}$ that describes the dynamics of the perturbations, allowing the flow to escape from linearly stable solutions in certain cases. This bypass mechanism has been postulated as an interpre-
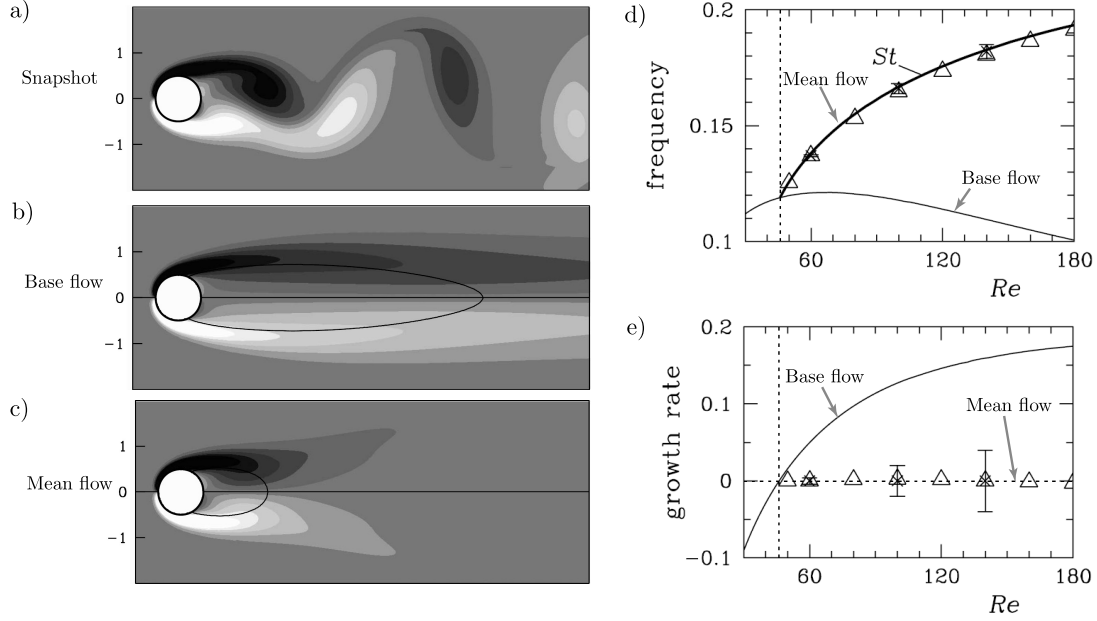
Figure 1.5 – Results from Barkley (2006). (a) Snapshot of the unstable vortex shedding, (b) base flow and (c) mean flow vorticity contours. (d) Frequencies (Strouhal) and (e) growth rates as a function of Reynolds number. In (d) frequency of the vortex shedding dark curve. Triangles are obtained from the stability analysis around the mean flow, and thin line shows the stability analysis around the base flow.

tation for the transition to turbulence in stable flows (Schmid & Henningson (2001); Schmid (2007)).

1.3 Nonlinear dynamics of oscillators and amplifiers

There are many situations for which the linear analysis fails to describe the main characteristics of the flow due to the intrinsic nonlinearity of the Navier-Stokes equations. Therefore, in this section we will introduce some of the concepts that have been developed along the years trying to describe the behaviour in flows for which the nonlinear dynamics plays a key role.

1.3.1 Oscillators

One of the most common supercritical flows is the wake flow that appears behind bluff bodies. The flow develops a strong intrinsic instability resulting in a von-Karman vortex street (von Karman (1911)), as illustrated in Fig. 1.1(b,c,e,f). An extensively studied prototype for bluff-body wakes is the flow past a circular cylinder. The laminar flow becomes absolutely unstable through a Hopf bifurcation for Reynolds number above $Re > 47$ (von Karman (1911); Jackson (1987); Provansal *et al.* (1987); Williamson (1988)), defined as $Re = U_\infty D/\nu$, where ν is the kinematic viscosity, U_∞ the free-stream velocity and D the cylinder diameter (see Fig. 1.5 (a)).
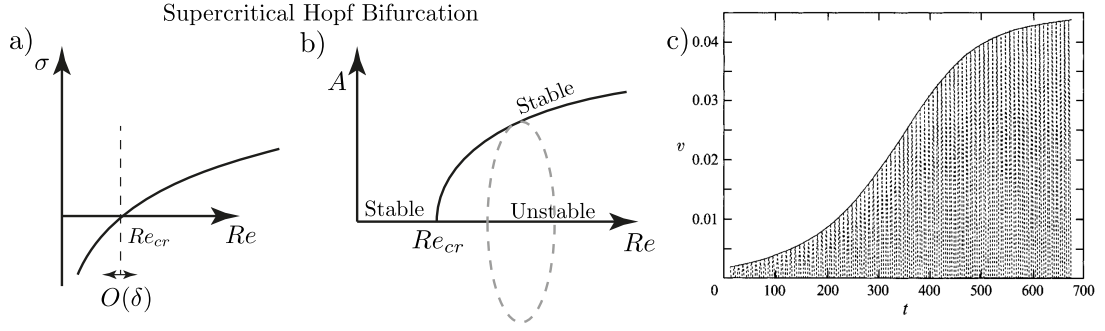
Figure 1.6 – Sketch of the supercritical Hopf bifurcation. (a) sketch of the transition from stable to unstable given by a positive growth rate σ at the critical Reynolds number Re_{cr} and (b) sketch of the evolution with Reynolds number Re of the amplitude A of the periodic fluctuations which is modelled by the Stuart-Landau amplitude equation (Stuart (1960)). (c) Evolution of the amplitude of the fluctuation in time t extracted from the signal in the unstable cylinder wake at $Re = 48$ (Dušek *et al.* (1994)).

As described in Fig. 1.4(c) the oscillations of the vortex street are dominated by a fundamental frequency when compared to higher harmonics, even in the fully saturated regime (Dušek *et al.* (1994); Pier & Huerre (2001); Pier (2002)).

The first natural approach is to try to describe the flow dynamics by linear stability analysis around the base flow which is the solution of the steady NSE. Global stability analysis around the base flow, depicted in Fig. 1.5(d) as thin line, provides an accurate frequency and spatial structure prediction of the dynamics only close to the threshold, while it fails to predict the frequency of the vortex shedding at Reynolds number beyond the critical value $Re > 47$ (Zebib (1987); Jackson (1987); Pier (2002); Noack *et al.* (2003); Barkley (2006); Sipp & Lebedev (2007)). However, stability analysis around the mean flow, defined as the time average value of the full NSE solution, provides a more accurate description of the dynamics in terms of frequency and spatial structure of the oscillations yielding a close to zero growth rate (Triantafyllou *et al.* (1986); Hammond & Redekopp (1997); Pier (2002); Barkley (2006)), see Fig. 1.5(e), although the saturation process and the amplitude of the oscillations are not described.

Nonlinear interactions and mean flow limitations

The incapability of the base flow linear stability analysis to predict the fluctuating frequency seems to be related to the nonlinearity (Waleffe (1995)) captured by the Reynolds stress which modifies the base flow into the mean flow, also reported in other flows by Maurel *et al.* (1995). Hence the use of nonlinear simple models as the Stuart-Landau amplitude equation (Stuart (1960)),

$$\frac{dA}{dt} = \lambda A - (\mu + \nu) A |A|^2, \tag{1.3}$$

9

for a complex amplitude A and whose complex coefficients (λ, μ, ν) depend on the Reynolds number ((Dušek *et al.* (1994); Sipp & Lebedev (2007)). These models are able to describe qualitative aspects of the saturation of the instability. The Stuart-Landau amplitude equation is capable of describing the saturation mechanism in supercritical Hopf bifurcations (Fig. 1.6(a,b)) as the flow passes from stable to unstable, providing an accurate estimation of the time evolution of the instability amplitude as illustrated in Fig. 1.6(c) for the cylinder flow at the critical Reynolds $Re_{cr} = 48$. The multiple-scale expansion study presented by Sipp & Lebedev (2007), for the base flow at the critical Reynolds number, shows the relation between the accurate description of the flow dynamics by the mean flow stability and the nonlinear coefficients of the simple amplitude equation. Therefore it relates the nonlinearity hidden in the mean flow through the Reynolds stress and the nonlinear saturation. A weakly nonlinear mode expansion for different bodies has been carried out by Meliga *et al.* (2009*a*,*b*). However, the perturbative nature of all these derivations limit their validity only very close to threshold.

The underlying dynamics are understood as a base flow that is globally unstable and therefore develops an instability which grows and modifies the underlying mean flow (Maurel *et al.* (1995); Zielinska *et al.* (1997)) through the Reynolds stress. This mean flow variation reduces the instability growth rate, by means of the nonlinear Reynolds stress terms as suggested initially by Stuart (1958) and later, described in the work on the transient evolution of the cylinder instability by Thiria & Wesfreid (2009) and Thiria *et al.* (2015). Eventually the perturbation is saturated in a marginally stable periodic cycle with zero growth rate around a stable mean flow in the spirit of Malkus (1956).

As described above, mean flow linear stability analysis includes part of the nonlinearities gathered in the Reynolds stress term. That is why acceptable predictions in terms of frequency and structure were obtained by performing mean flow stability analysis on high Reynolds number turbulent wake flow using RANS and LES turbulent models applying local analysis in Meliga *et al.* (2009*c*) and using the global approach in Meliga *et al.* (2012). However, when there is a strong interaction between harmonics or the temporal spectrum is broad, the stability around the mean flow fails (Meliga *et al.* (2009*c*, 2012)), which is interpreted as the lack of nonlinear interaction between the fluctuation with itself in the mean flow stability. These ideas are confirmed in Turton *et al.* (2015) where instabilities in thermosolutal convection are reported. The mean flow stability of the traveling waves, characterised by a peaked temporal power spectrum, yields an eigenvalue whose real part is almost zero and whose imaginary part corresponds very closely to the nonlinear frequency. In contrast, linear stability on the mean field of the standing waves, characterised by a broad power spectrum, yields neither zero growth nor the correct nonlinear frequency. All these results suggest that the frequency of any quasi-monochromatic oscillation can be predicted from its temporal stability of the mean, a property coined RZIF (Real zero imaginary frequency) by L. Tuckerman in Turton *et al.* (2015).
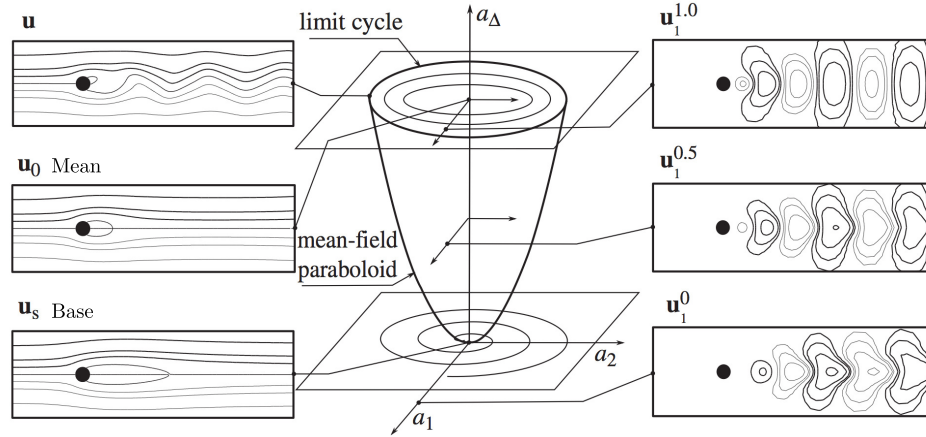
Figure 1.7 – Sketch of the transient wake dynamics from Tadmor *et al.* (2011). The figure illustrates on the left insets the deformation between the base flow and the mean flow accounted for by the shift mode, in vertical Δa (Noack *et al.* (2003)), which is not contained in the basis of the unstable base flow modes $(a_1 \, a_2)$. The unstable mode deformation along the transient is depicted on the right insets.

Reduced order models

One of the motivations to understand in details how the fluid systems behave is to create simpler models for flow control. These low-order models are addressed in the least-order Galerkin framework (Noack *et al.* (2003); Tadmor *et al.* (2010, 2011)). Initially the models are based on a fixed set of dominant coherent structures obtained from the linear dynamics around the base flow. The range of validity of these simple models is restricted because they ignore mode deformations during transients as it happens in the saturation of the cylinder wake. These limitations are addressed by introducing the shift mode (Noack *et al.* (2003)) as a least-order Galerkin representation of the mean flow variations as depicted in vertical in Fig. 1.7, where the shift mode is represented out of the space of the base flow mode basis, which is depicted as a horizontal plane. The described bilateral coupling between variations in the fluctuation growth rate and mean flow variations in the NSE is described in Tadmor *et al.* (2010). The low dimensional models based on proper orthogonal decomposition (POD) (Noack *et al.* (2003) Tadmor *et al.* (2010) Tadmor *et al.* (2011)) are then able to predict the mean flow behaviour as well as the transient from steady base flow to the developed periodic oscillatory flow. The nonlinear structure of the Reynolds stress is described in terms of the POD harmonics extracted from the mean flow providing a very good description of the system dynamics.

Full nonlinear approach

All the pieces of work presented so far introduce the nonlinear terms *a posteriori*, resorting to the exact DNS results to extract information of the nonlinear behaviour. In a different
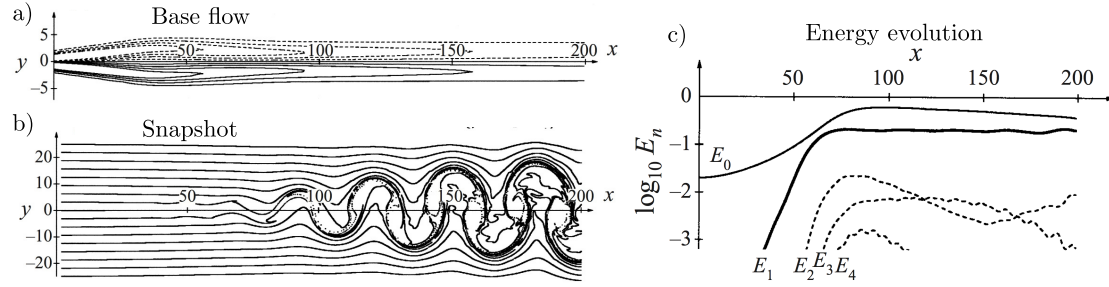
Figure 1.8 – (a) Shows the base flow of the synthetic two-dimensional wake. (b) Illustrates the fluctuations of the von-Karman vortex street (c) Shows the energy evolution of the different modes, illustrating the mean flow modification and the first harmonic as the most energetic. Figures extracted from the work of Pier & Huerre (2001).

approach, looking back to the local stability introduced above, Pier & Huerre (2001) study the nonlinear saturation and frequency selection of the vortex shedding on a synthetic weakly non-parallel wake Fig. 1.8(a). From the previous study (Pier & Huerre (1998)) it is known that the frequency of the whole nonlinear wave train described as a steep global mode is dictated by the marginal stability criterion of the absolute real frequency at the local transition station between convectively unstable and absolutely unstable (see Fig. 1.3 (a)). The relevance of the study in Pier & Huerre (2001) is based on the *a priori* non-linear approach where interaction of different modes at different wave numbers create a nonlinear dispersion relation, in the context of temporal analysis. Imposing the selected frequency in the dispersion relation, it is possible to obtain the correct wave number providing the fluctuating structure and thus the description of the whole nonlinear dynamics. A detailed analysis of the dynamics reveals that the mode corresponding to the zeroth wave number is associated to the mean flow modification from the base flow created by the nonlinear Reynolds stress forcing. Furthermore, observe how the full nonlinear saturated oscillations is well approximated by the first harmonic around the mean flow, illustrated in Fig. 1.8(c) where the first harmonic clearly dominates the fluctuating energy. This very same frequency selection criterion is applied to the cylinder wake in Pier (2002) showing a fair estimation of the vortex shedding frequency, even in this strongly non-parallel flow, although the linear stability around the mean flow performs better.

Summarising, the reported studies suggest the nonlinear Reynolds stress term and the first harmonic of the saturated state as the key ingredients to describe the strongly nonlinear saturation occurring in supercritical flows.

1.3.2 Amplifiers

An example of a convectively unstable flow with strong advection of the perturbation is the jet flow. Jets can present coherent oscillating structures that come from amplification of the incoming perturbation as noise at the inlet (Crow & Champagne (1971); Garnaud (2012); Garnaud *et al.* (2013)) and illustrated in Fig. 1.9 for laminar and turbulent jets (Garnaud *et al.*

(2013)). Trying to account for certain nonlinearity, Nichols & Lele (2010) and Garnaud (2012);
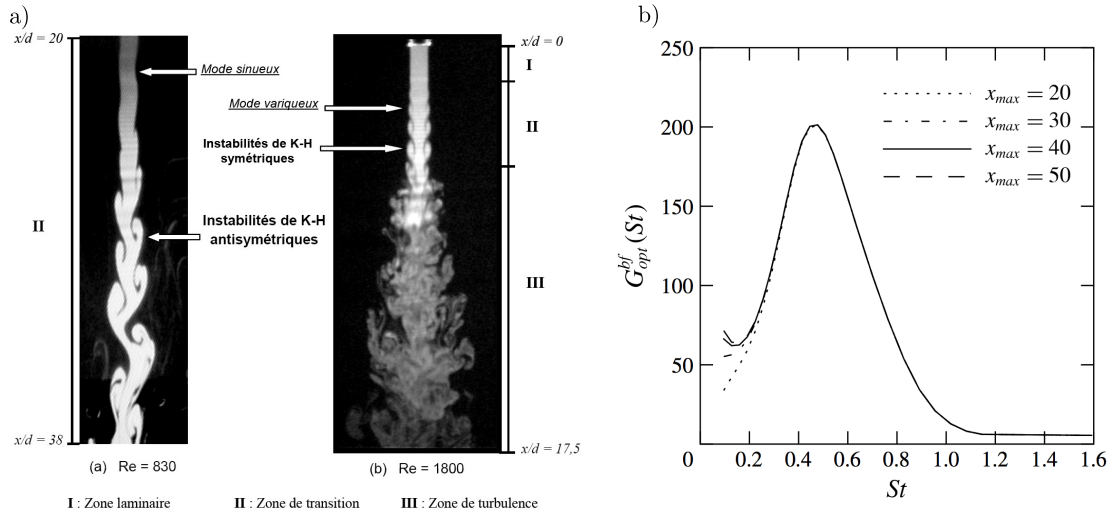
Figure 1.9 – (a) Experiment of a laminar and turbulent jet illustrating the coherent perturbation structures that appear at relatively low Reynolds due to the Kelvin-Helmholtz instability in axisymmetric jets, Zaouali *et al.* (2009). (b) Optimal gain at each frequency for an optimal forcing/response around a mean flow of a modelled turbulent jet (Garnaud *et al.* (2013)).

Garnaud *et al.* (2013) performed linear stability analyses around the mean flow in turbulent jets instead of the base flow and showed that all eigenvalues have negative growth rate as depicted in Fig. 1.4(f). This convective nature of the jet flow, with no intrinsic instability, defines the jet as a selective amplifier.

The authors took a different approach and conducted a study of optimal linear frequency response to forcing on the model mean flow of a turbulent jet at high Reynolds number using a global approach. It was found that a frequency selection mechanism exists, yielding a system with higher gain or equivalently larger resolvent operator norm at certain frequency range, see Fig. 1.9(b). Optimal body forcing and boundary condition forcing were used with similar results for the preferred frequency and response structures, showing a clear connection between body and boundary forcing.

Another example of an amplifier is the backward-facing step, showing stable two-dimensional modes for Reynolds number at least up to $Re \sim 1500$ and exhibiting the first three-dimensional unstable mode at $Re_{cr} \sim 748$ (Barkley *et al.* (2002) and Lanzerstorfer & Kuhlmann (2012)). Receptivity analyses on the base flows have been performed by Marquet & Sipp (2010); Boujo & Gallaire (2015); Marquet *et al.* (2010) showing a very strong amplification to optimal forcing in a narrow range of frequency. In addition, Blackburn *et al.* (2008) also study the transient growth of the globally stable backward-facing step presenting a very large time amplification as illustrated in Fig. 1.10. Results of Blackburn *et al.* (2008) for the three-dimensional backward facing step under stochastic forcing at the inlet shows a predominantly two dimensional response structure, very similar to the linear optimal growth perturbations. In addition, the

13

a) Perturbation evolution
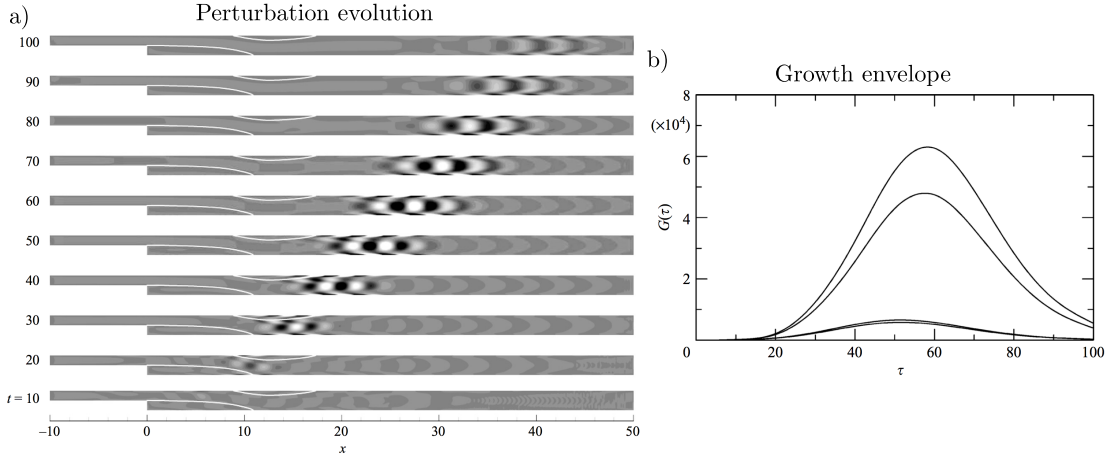
b) Growth envelope

Figure 1.10 – (a) Sequence of the linear perturbation vorticity developed from the global optimum disturbance initial condition. The characteristic space-time dynamics of a local convective instability is clear. (b) Growth envelopes of the optimal and some leading sub-optimal two-dimensional disturbances. Two-dimensional backward-facing step at $Re = 500$ (Blackburn *et al.* (2008)).

response shows a very narrow frequency range, in line with the linear predictions.

Coupled systems: mean flow - fluctuation

It should be highlighted that these studies are linear and do not account for any sort of nonlinearity that might appear due to the large amplifications. In fact, large amplifications of external disturbances added to the sensitivity of the linear operator allows the flow to escape from linearly stable solutions as seen in transition to turbulence. This scenario is studied by means of nonlinear or semi-linear models. The stochastic structural stability theory (SSST) has been introduced by Farrell & Ioannou (1993) to describe the appearance of coherent structures in stable flows. The theory is formalised in the stochastic framework, assuming that the flow is forced by white noise to model turbulence and external disturbances. SSST consists in rewriting the full NSE forced by white noise, δ-correlated in space and time, in a system of equations where the linear response to white noise is coupled to the time varying ensemble average mean flow by means of the nonlinear Reynolds stress. The stochastic linear response to forcing is reformulated as the covariance matrix that describes the statistically steady state of the response as a Lyapunov equation. The coupled dynamical system is written as

$$\frac{d\boldsymbol{U}}{dt} = \mathcal{N}(\boldsymbol{U}) + F(\boldsymbol{C}), \tag{1.4a}$$

$$\frac{d\boldsymbol{C}}{dt} = \mathcal{L}_{\boldsymbol{U}}\boldsymbol{C} + \boldsymbol{C}\mathcal{L}_{\boldsymbol{U}}^{\dagger} + \boldsymbol{Q}, \tag{1.4b}$$

where $\boldsymbol{U}$ is the ensemble averaged mean flow, $\boldsymbol{C}$ is the covariance matrix of the response statistics, $\boldsymbol{Q}$ defines the spatial distribution of the white noise forcing, $F(\boldsymbol{C})$ is the Reynolds

stress forcing contracted from the fluctuating response and $\mathcal{N}$ and $\mathcal{L}$ are the nonlinear and linear operators respectively, extracted from the NSE.
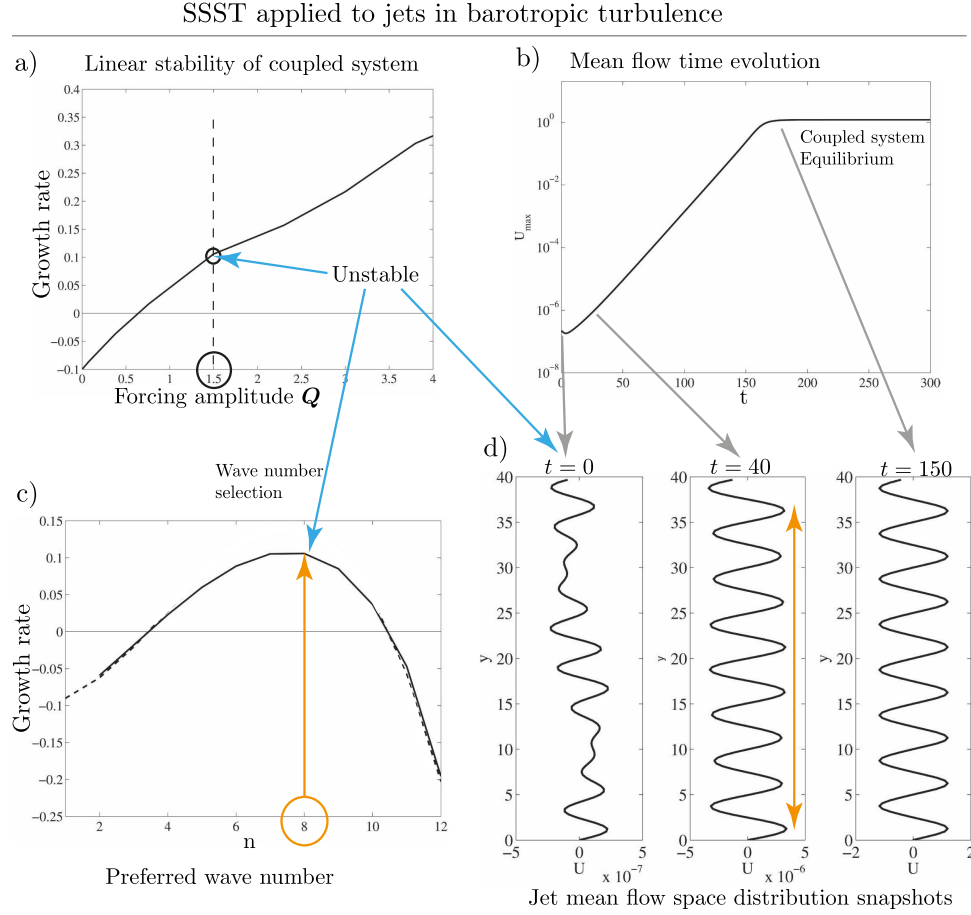
Figure 1.11 – SSST theory applied to jets in barotropic turbulence (Farrell & Ioannou (2007)). a) Linear stability of the coupled system (1.4) around the equilibrium states at different white noise forcing Q, b) for a forcing of amplitude Q = 1.5 the system is unstable and starts evolving nonlinearly to a new equilibrium state. c) The preferred wave number of the most unstable mode is selected n = 8 and appears in the saturated state. d) Snapshot of the mean flow as it evolves from unstable equilibrium perturbed t = 0, then the most unstable mode starts to grow t = 40 and it settles in a new steady equilibrium state $t > 150$.

The traditional concept of flow stability addresses the stability of eddy perturbations C assuming a mean flow structure U. Stability in this sense is determined by the eigenvalue of the operator $\mathcal{L}$ with the greatest real part as described above. However, the time-dependent system (1.4) allows for excursions of $[C, U]$ that are transiently unstable, in other words, the linear operator $\mathcal{L}$ can be stable but the linearised coupled system (1.4) can be structurally unstable for certain values of the forcing. This scenario is represented in Fig. 1.11 for the description of turbulent jets that appear in the atmosphere. The linear operator $\mathcal{L}$ around the mean flow U is always stable, however the steady solution of the coupled system becomes un-

stable for certain value of the background turbulence forcing Q (Fig. 1.11(a)) with a preferred wave number of the unstable eigenmode illustrated in Fig. 1.11(b). The system escapes from the initial equilibrium solution to another equilibrium through a transient Fig. 1.11(b,c). This example is one of the situations in which the SSST was applied to describe the appearance of coherent structures in turbulent atmospheric flows that are linearly stable in the traditional sense, as described in Farrell & Ioannou (2003, 2007, 2009*a,b*), among other works.
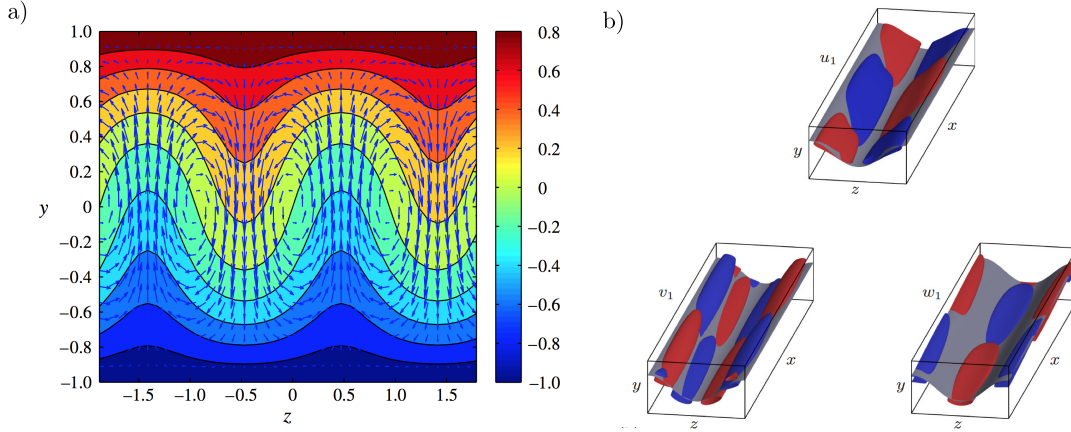
Figure 1.12 – a) The finite-amplitude streamwise roll and streak that result from the equilibration of the eigenmode of the SSST system (1.4) for Couette flow (Farrell & Ioannou (2012)). It shows the streamwise-averaged mean flow velocity in streamwise direction U (contours) and the spanwise velocities V, W (vectors). Consistent with the lift-up mechanism, positive V is associated with a decrease in U. b) Three-dimensional illustration of the fluctuating flow associated with the Couette flow at $Re \simeq 1500$ (Beaume *et al.* (2015)). The surfaces represented in colour correspond to the fluctuating velocities around the mean flow. The grey surface represents the critical layer of the zero value of the streamwise averaged mean flow.

A very important property of the coupled equations (1.4) is their global stability, that is, that both the perturbations field covariances and the mean flow remain bounded for all times as proven in Farrell & Ioannou (2003). This global stability property of the coupled equations implies that even if the velocity profiles become transiently exponentially unstable the fluxes induced by the perturbation fields equilibrate the instabilities maintaining perturbation fields of finite variance and mean flow. These coupled equations can thus produce a time-dependent equilibration of instabilities in a turbulent environment and constitute a stochastic alternative to the deterministic Landau equation paradigm for stabilisation of unstable systems (Farrell & Ioannou (2003)).

Furthermore, the generality of the SSST allows it to describe sustained coherent structures of interactions between Rolls and Streaks that appear during the transition to turbulence in the three-dimensional Couette flow (Farrell & Ioannou (2012)), and depicted in Fig. 1.12(a). An extension of this theory, called the restricted nonlinear model (RNL) simplifies the calculations and has been applied more recently also to the description of transient dynamics in the Couette

flow (Thomas *et al.* (2014)).

Another example of these models that describe the nonlinear instability in linearly stable flows is presented by Beaume *et al.* (2015). The model consists in a system of the mean flow equation coupled by the nonlinear Reynolds stress forcing to the linear equation of the response to external forcing around this mean flow. The model is coupled iteratively and is able to describe the coherent structures, illustrated in Fig. 1.12(b), that appear due to hydrodynamic instability in the transition to turbulence in the Couette flow (Drazin & Reid (1981); Waleffe (1997)). These quasilinear models provide a complementary point of view to the tracking of fully nonlinear states see Schneider *et al.* (2010) for a very recent contribution and references therein.

1.4 Present work

Different linear and nonlinear approaches have been used for local and global stability analysis over the past years. As documented above, to describe the dynamics of certain stable and unstable flow configurations, it is of crucial importance to retain some nonlinear terms, as in the simple model of the Stuart-Landau equation (Stuart (1960)) used for the description of supercritical instabilities. In unstable flows, the key role of the nonlinearity hidden in the mean flow through the Reynolds stress has been highlighted in the description of the flow dynamics in the unstable wake (Triantafyllou *et al.* (1986); Hammond & Redekopp (1997); Pier (2002); Pier & Huerre (2001); Barkley (2006); Noack *et al.* (2003); Tadmor *et al.* (2010); Maurel *et al.* (1995); Thiria & Wesfreid (2009); Thiria *et al.* (2015); Meliga *et al.* (2009*c*)), while in stable configurations, the nonlinear coupling of linear response and mean flow serves to describe the coherent structures during the transition to turbulence (Waleffe (1995); Farrell & Ioannou (2003, 2007); Bakas & Ioannou (2011); Farrell & Ioannou (2012); Thomas *et al.* (2014); Beaume *et al.* (2015)).

A simplified physical description that accurately accounts for the nonlinear saturation of the instability in unstable flows as well as for the saturation of the response to disturbances in stable flows is still missing. This opens the question of whether one could formulate a simplified set of equations to capture the physical picture that describes the saturation dynamics of oscillators and amplifiers far from threshold (Stuart (1958, 1960); Waleffe (1995)).

This thesis aims at answering this question by introducing a coupled self-consistent semi-linear model. Inspired by the works of Stuart (1960); Sipp & Lebedev (2007); Pier & Huerre (2001); Farrell & Ioannou (2003); Barkley (2006) the model consists in a mean flow equation coupled with a linear fluctuating equation by means of the Reynolds stress feedback. The model is first introduced in an unstable flow, the benchmark cylinder flow, and subsequently applied to a stable amplifier flow, the backward-facing step flow. A similar mechanism of the saturation dynamics happens in both flows.

1.5   Outline

The outline of this thesis is the following.

Chapter 2 briefly introduces the self consistent model in the unstable cylinder flow describing the von-Karman vortex street and the mean flow of the saturated regime formalising the key ingredients that govern the saturation.

Chapter 3 revisits the saturated flow in the cylinder case providing more details on the nonlinear dynamics as well as of the iterative procedure used to couple the system. Furthermore, the transient of the saturation is described by the self-consistent model.

Chapter 4 introduces the self-consistent model applied to an amplifier; the backward-facing step forced by optimal harmonic forcing. First, it is presented an asymptotic analysis to describe the influence of the different nonlinear interactions and then the nonlinear dynamics of the saturation is reported.

In **Chapter 5** the self-consistent model is extended to an amplifier excited by white noise forcing, applying the model to an approximation of stochastic forcing/response in the frequency domain.

In **Chapter 6** a discussion is presented, showing the advantages and drawbacks of the model.

Finally in **Chapter 7** short conclusions are drawn and possible future works are described.

Appendix A describes some of the critical aspects of the self-consistent model and its implementation.

2 Mean flow stability for an unstable open flow

This chapter presents a first attempt to understand better the nonlinear saturation mechanism in the cylinder wake flow. A semi-linear self-consistent model is introduced and validated answering the question why the mean flow linear stability analysis is relevant for the description of the dynamics and highlighting the role of the nonlinear Reynolds stresses in the saturation process.

Paper: *A self-consistent mean flow description of the nonlinear saturation of the vortex shedding in the cylinder wake*

A self-consistent mean flow description of the nonlinear saturation of the vortex shedding in the cylinder wake

Vladislav Mantič-Lugo[1], Cristóbal Arratia[1] and François Gallaire[1]

1) LFMI, École Polytechnique Fédérale de Lausanne, CH-1015 Lausanne, Switzerland

The Bénard-von Karman vortex shedding instability in the wake of a cylinder is perhaps the best known example of a supercritical Hopf bifurcation in fluid dynamics. However, a simplified physical description that accurately accounts for the saturation amplitude of the instability is still missing. Here we present a simple self-consistent model that provides a clear description of the saturation mechanism and quantitatively predicts the saturated amplitude and flow fields. The model is formally constructed by a set of coupled equations governing the mean flow together with its most unstable eigenmode with finite size. The saturation amplitude is determined by requiring the mean flow to be neutrally stable. Without requiring any input from numerical or experimental data, the resolution of the model provides a good prediction of the amplitude and frequency of the vortex shedding, as well as the spatial structure of the mean flow and the Reynolds stress.

PACS numbers: 47.20.Ky, 47.15.Fe, 47.27.-i, 47.32.-y

2.1 Introduction

Simple models are essential to our understanding of complex nonlinear phenomena. The van der Pol oscillator, for example, demonstrates how nonlinear oscillations can be described by the appearance of a limit cycle (Charru (2011)). In large dimensional systems, however, these simple models do not entirely reveal the mechanisms that determine relevant parameters like the dominant frequency or saturation amplitude. For supercritical instabilities in fluid dynamics, the mean flow has been proposed as a key element to explain the origin of the dominant frequency (Triantafyllou *et al.* (1986); Hammond & Redekopp (1997); Pier (2002); Barkley (2006)) and the physical mechanism of the saturation process (Stuart (1958); Maurel *et al.* (1995); Barkley (2006)). The physical picture thus invoked to understand the saturation is the following: perturbations feeding on an unstable flow induce mean flow modifications that increase while perturbations grow, up to the point where the mean flow becomes neutrally stable and perturbations stop growing and saturate. The present Letter aims at assessing this scenario.

An early formulation of this concept of marginal stability of the mean flow was given by (Malkus

(1956)) in the context of turbulent flows. Shortly after, aiming for an equation describing the saturation of supercritical instabilities, (Stuart (1958)) devised a simplified closed system wherein the mean flow was only affected by the Reynolds stress divergence of its leading eigenmode. By further assuming that the eigenmode was given by the unperturbed base flow, Stuart managed to obtain an equation for the saturation amplitude through the exact balance between the dissipation of the perturbation and the energy transfer from the mean flow. It wasn't until after two more years, through a more rigorous perturbative analysis close to threshold, that he mathematically derived an amplitude equation, the Stuart-Landau equation, directly from the Navier-Stokes equations (Stuart (1960)).

Despite the beauty and consistency of the multiple-scale expansion method, its perturbative nature implies that the spatial structure of the growing unstable mode is in large part fixed by the unperturbed base flow. However, there are cases in which the spatial structure of the saturated mode differs considerably from that of the linear mode, limiting the validity of the usual Stuart-Landau amplitude equation (Dušek *et al.* (1994); Noack *et al.* (2003)). This opens the question of whether one can formulate a more accurate prediction of the saturation amplitude by retaining some of the spatial degrees of freedom.

The purpose of the present Letter is to propose a model that physically describes the saturation mechanism of an unstable flow, shedding some light on the nonlinear effects that are relevant for the coupling of the perturbation and the mean flow equations. The coupled equations are solved in a self-consistent way, through a quasi-linear single harmonic approximation of the perturbation, allowing to determine *a priori* the mean flow and the frequency and structure of the dominant harmonic perturbation, without resorting *a posteriori* to linear stability analysis of mean flows averaged from DNS or experimental data. In addition, the method yields a prediction of the perturbation amplitude.

A widely studied archetype of a supercritical instability in fluid flows is the flow past a circular cylinder (Williamson (1988)), characterized by the non-dimensional Reynolds number $Re = U_\infty D/\nu$, where ν is the kinematic viscosity, U_∞ the free-stream velocity and D the cylinder diameter. As the Reynolds number increases, a Hopf bifurcation occurs at $Re \sim 47$(Provansal *et al.* (1987)) and the flow dynamics changes from a steady symmetric state to an oscillating time periodic configuration presenting the Bénard-von Karman vortex street (von Karman (1911)). The contribution of the fundamental harmonic is dominant compared to the higher harmonics even in the fully saturated regime(Dušek *et al.* (1994)).

Linear stability analyses describes well this instability by predicting the value of the threshold as well as the shedding frequency at threshold (Zebib (1987); Jackson (1987); Noack *et al.* (2003)). However, as noticed in Pier (2002) and Barkley (2006), the frequency prediction based on the leading eigenvalue of the base flow does not match the experiments as one departs from threshold. In contrast, the stability analysis around the mean flow shows a remarkably good frequency prediction with almost zero growth rate, supporting the validity of Malkus' marginal stability criterion. However, these linear stability analyses cannot provide any information

about the perturbation amplitude.

Qualitative aspects of the saturation of the instability are well described by a Stuart-Landau amplitude equation, the coefficients of which could be obtained both empirically (Dušek *et al.* (1994) =)and using the multiple-scale expansion, as done by Sipp & Lebedev (2007). However, due to the perturbative nature of its derivation, this model is quantitatively valid only very close to threshold. We therefore focus on the supercritical regime of the flow past a cylinder, for $Re > 47$ and propose a non-perturbative quasilinear model coupling the mean flow equation to a linear harmonic disturbance, consistently accounting for the mean flow distortion. In this approach, the mean flow comes as a result of the model instead of being required as an input.

2.2   The physical concept of the self-consistent model

The starting point of the model is the Reynolds decomposition $\boldsymbol{u}(\boldsymbol{x}, t) = \boldsymbol{U}(\boldsymbol{x}) + \boldsymbol{u}'(\boldsymbol{x}, t)$ of the instantaneous flow in mean $\boldsymbol{U} = \langle \boldsymbol{u} \rangle$ and perturbation $\boldsymbol{u}'$, where $\langle\rangle$ denotes time-averaging and where $\langle \boldsymbol{u}' \rangle = 0$ by construction. Because of incompressibility, it is understood in what follows that all velocity fields must be divergence free; we will not write this condition explicitly. This decomposition can be introduced in the 2D incompressible Navier-Stokes equations to yield

$$N(\boldsymbol{U}) = -\langle (\boldsymbol{u}' \cdot \nabla) \boldsymbol{u}' \rangle \tag{2.1a}$$

$$\partial_t \boldsymbol{u}' + L_{\boldsymbol{U}}(\boldsymbol{u}') = -(\boldsymbol{u}' \cdot \nabla) \boldsymbol{u}' + \langle (\boldsymbol{u}' \cdot \nabla) \boldsymbol{u}' \rangle \tag{2.1b}$$

where

$$N(\boldsymbol{U}) \equiv (\boldsymbol{U} \cdot \nabla) \boldsymbol{U} + \nabla P - Re^{-1} \Delta \boldsymbol{U}, \tag{2.2}$$

corresponds to the advective, pressure gradient and diffusive terms of the Navier-Stokes equations (NSE) and $L_{\boldsymbol{U}}(\boldsymbol{u}')$ is the corresponding operator for the NSE linearized around $\boldsymbol{U}$, i.e.

$$L_{\boldsymbol{U}}(\boldsymbol{u}') \equiv (\boldsymbol{U} \cdot \nabla) \boldsymbol{u}' + (\boldsymbol{u}' \cdot \nabla) \boldsymbol{U} + \nabla p' - Re^{-1} \Delta \boldsymbol{u}'. \tag{2.3}$$

P and p' are the pressure fields required to impose incompressibility on $\boldsymbol{U}$ and $\boldsymbol{u}'$, respectively. No approximation has been performed so far.

Different nonlinear effects can be identified in (2.1). The right hand side (RHS) of (2.1a) corresponds to minus the Reynolds stress divergence $\langle (\boldsymbol{u}' \cdot \nabla) \boldsymbol{u}' \rangle$, a forcing of $\boldsymbol{u}'$ on $\boldsymbol{U}$ which can be also viewed as the body force required for the mean flow $\boldsymbol{U}$ to become a stationary solution of the NSE (Barkley (2006)). The effect of the mean flow $\boldsymbol{U}$ back on the fluctuating part $\boldsymbol{u}'$ is contained in the nonlinear advection terms of the linearized operator $L_{\boldsymbol{U}}(\boldsymbol{u}')$; with $\boldsymbol{U}$ prescribed by experimental or computational data, these are the terms that are taken into account in mean flow stability analyses. The RHS of (2.1b) contains the nonlinear terms that allow interactions of $\boldsymbol{u}'$ at different frequencies and generate different harmonics. In
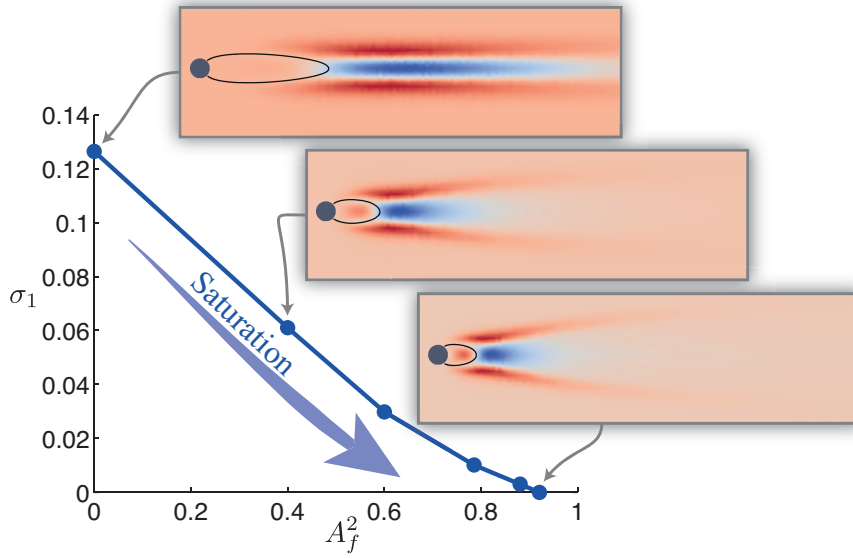
Figure 2.1 – Growth rate σ_1 for the converged coupled system of equations of the self-consistent model (2.4) for different Reynolds stress forcing amplitudes A_f^2 at $Re = 100$. The insets show the spatial distribution of the divergence of the Reynolds stress in the x-direction and the boundary of the recirculation region for different A_f^2, as indicated in the figure.

the present case of the cylinder, the power spectra of the vortex shedding signal is strongly dominated by a single frequency, the fundamental harmonic of the vortex shedding (Dušek *et al.* (1994)). Neglecting the nonlinear terms in the RHS, Eq. (2.1b) becomes linear in $\boldsymbol{u}'$. The linearized Navier-Stokes operator can be diagonalized and the perturbation can be therefore expanded into the basis of its eigenmodes $\boldsymbol{u}'_n = \boldsymbol{u}_n \exp(\lambda_n t) + \bar{\boldsymbol{u}}_n \exp(\bar{\lambda}_n t)$, where the overbar represents the complex conjugate. Focusing on the least stable eigenmode pair $n = 1$, one obtains

$$N(\boldsymbol{U}) = -2A^2 \Re\left((\bar{\boldsymbol{u}}_1 \cdot \nabla)\boldsymbol{u}_1\right), \tag{2.4a}$$

$$\lambda_1 \boldsymbol{u}_1 + L_{\boldsymbol{U}}(\boldsymbol{u}_1) = 0, \tag{2.4b}$$

where $\boldsymbol{u}_1$ is the least stable eigenmode of the model mean flow $\boldsymbol{U}$ as computed from (2.4b), $\lambda_1 = \sigma_1 + i\omega_1$ is its associated eigenvalue and A is a real constant that represents the amplitude of the first eigenmode as normalized by its L^2 norm. $\Re(\cdot)$ in (2.4a) denotes the real part. In the computation of the Reynolds stress divergence, the time variation associated to the real part of the eigenvalue σ_1 is neglected. Therefore, Eq. (2.4a) can be seen as a quasi-static approximation of the mean flow in which the slow time scale dynamics associated to the growth of the unstable mode is slaved to the amplitude A, which may be then treated as an external parameter.

The straightforward solution of (2.4) for $A = 0$, corresponds to the base flow $\boldsymbol{U}_B$, i.e. the stationary solution of the NSE together with its corresponding unstable eigenmode $\boldsymbol{u}_{1,B}$,
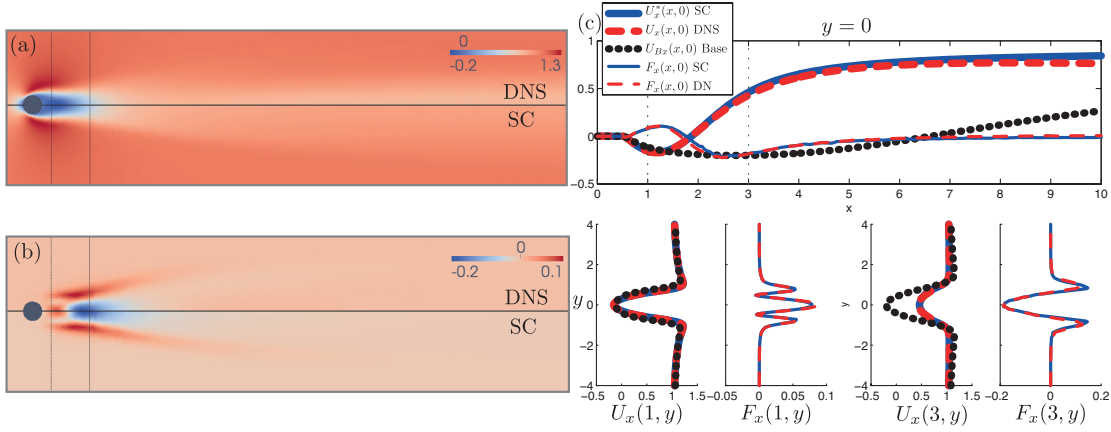
Figure 2.2 – Comparison of the x-component of the mean flows (a) and the Reynolds stress divergence (b) for $Re = 100$ computed from DNS (top half) and predicted from (2.5) (bottom half, SC). Plot (c) shows horizontal and vertical cuts for y=0 (top), x=1 (bottom left), and x=3 (bottom right), for the x-component of the mean flows ($\boldsymbol{U}, \boldsymbol{U}^*$), the base flow ($\boldsymbol{U}_B$) and Reynolds stress divergence ($\boldsymbol{F} = \langle(\boldsymbol{u}' \cdot \nabla)\boldsymbol{u}'\rangle$), as detailed in the legend.

which represents the initial perturbation growing at a rate $\sigma_{1,B}$ and frequency $\omega_{1,B}$. If the amplitude A is increased, the unstable mode turns the initial base flow into an increasingly modified mean flow through the divergence of the Reynolds stress in (2.4a). In the process, the mean flow modifications simultaneously change the eigenmode structure and eigenvalue through the linearized perturbation equation (2.4b). One can expect that, from small to moderate values of the amplitude A, there exists a solution to the coupled perturbation–mean flow equations (2.4), meaning that the perturbation structure $\boldsymbol{u}_1$ is the one that forces the mean flow $\boldsymbol{U}$ by the Reynolds stress divergence in such a particular way that the mean flow generates the aforementioned perturbation structure $\boldsymbol{u}_1$. Associated to this solution there will be a certain growth rate σ_1 and frequency ω_1, creating an implicit relation between the growth rate and amplitude $\sigma_1(A)$.

For a finite amplitude A, the software FreeFem++ is used to discretize (2.4) and solve (2.4a) for a given $\boldsymbol{u}_1$, while SLEPC is used for the eigenvalue problem (2.4b) with a given $\boldsymbol{U}$. These two equations are then coupled through an iterative scheme until convergence is achieved. The eigenmode of an initial guess for the mean flow $\boldsymbol{U}_g$ (the base flow $\boldsymbol{U}_B$ or a solution of (2.4) for a smaller amplitude) is used for the Reynolds stress forcing in (2.4a), allowing to solve for a mean flow correction $\boldsymbol{U}_c$ which serves to generate a new guess $\boldsymbol{U}_{ng} = \gamma \boldsymbol{U}_c + (1 - \gamma)\boldsymbol{U}_g$ where $0 < \gamma < 1$. The leading eigenmode of the new guess is then computed and the process is repeated until convergence is achieved. We have found that this procedure converges robustly provided the eigenmode is normalized by its associated Reynolds stress divergence, i.e. when $A_f^2 \equiv A^2 \|2\Re((\bar{\boldsymbol{u}}_1 \cdot \nabla)\boldsymbol{u}_1)\|_{L^2} / \|\boldsymbol{u}_1\|_{L^2}^2$ is fixed. This is natural since variations of the amplitude A_f directly control the magnitude of the forcing term (RHS in 2.4a).

As shown in Fig. 2.1, the growth rate σ_1 resulting from these computations decreases as the
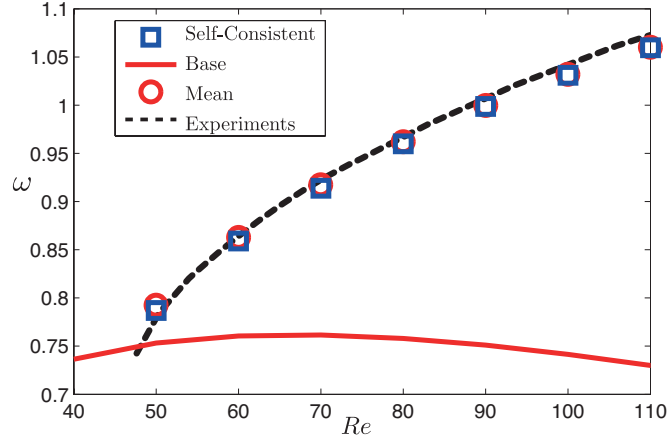
Figure 2.3 – Comparison of the frequency predictions of the self-consistent model for different Reynolds numbers. Vortex shedding frequency from experiments byWilliamson (1988) (dashed black line), the present result (blue triangles), the most unstable mode of the base flow (solid red line) and the mean flow obtained from DNS (red squares).

amplitude of the Reynolds stress increases. At the same time, the structure of the Reynolds stress forcing computed from the most unstable eigenmode moves upstream with increasing amplitude A_f, (insets in Fig. 2.1) continuously modifying the mean flow and stabilizing it. The upstream migration of the Reynolds stress forcing follows the shortening of the recirculation region of the corresponding mean flow, indicated by the black line in each inset of Fig. 2.1. This length reduction of the recirculation region is totally in line with previous descriptions of the differences between the base and the mean flow (Barkley (2006); Noack *et al.* (2003)), and it has been proposed as a key feature for the instability saturation mechanism (Zielinska *et al.* (1997)).

A clear physical picture emerges: the base flow $\boldsymbol{U}_B$ first develops its instability which grows and forces the underlying flow through the Reynolds stress divergence $2A^2\Re\left((\bar{\boldsymbol{u}}_1 \cdot \nabla)\boldsymbol{u}_1\right)$, modifying it towards the mean flow. If one is to imagine that the evolution given by the NSE linearized around the model's mean flow (2.4b) could approximate the evolution of the vortex shedding around the exact mean flow, then one requires the leading eigenmode to oscillate in a purely sinusoidal way. This corresponds to the marginal stability criterion, consistent with the results of Barkley (2006) and with the stabilizing effect of the growing perturbations on $\sigma_1(A)$ through the mean flow distortion (see Fig. 2.1). Therefore, we look for a particular amplitude A^* for which there is a marginally stable mean flow $\boldsymbol{U}^*$ such that $\sigma_1^*(A^*) = 0$. This amplitude A^*, which is not known a priori, will correspond to the saturation amplitude of the self-consistent model:

$$N(\boldsymbol{U}^*) = -2A^{*2}\Re\left((\bar{\boldsymbol{u}}_1^* \cdot \nabla)\boldsymbol{u}_1^*\right), \tag{2.5a}$$

$$i\omega_1^*\hat{\boldsymbol{u}}_1^* + L_{\boldsymbol{U}^*}(\hat{\boldsymbol{u}}_1^*) = 0. \tag{2.5b}$$

25
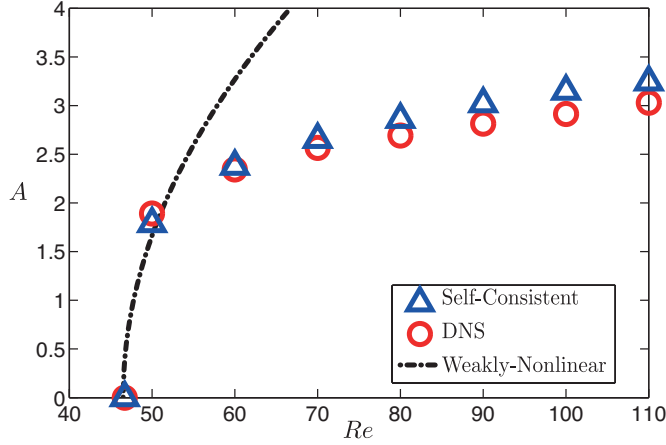
Figure 2.4 – Comparison of the vortex shedding amplitude predictions of the self-consistent model for different Reynolds numbers. Saturation amplitude obtained from DNS (red circles), predicted by the self-consistent model (blue triangles) and as given according to weakly nonlinear expansion around threshold (dash-dotted line).

2.3 Self-consistent model for the mean flow calculation

Fig. 2.2(a) compares the converged mean flow $\boldsymbol{U}^*$ obtained by the present model (bottom half) with the mean flow of the nonlinear DNS (top half), showing that the approximation of the mean flow x-direction velocity is remarkable, with a length and minimum velocity of the recirculation region about 2% from the equivalent values of the full DNS. Moreover, the similarity of the Reynolds stress divergence of the model, calculated from the leading eigenmode $\boldsymbol{u}_1$, and that of the fully nonlinear time-averaged DNS is striking (Fig. 2.2(b)). A more quantitative comparison is given in Fig. 2.2(c). It should be highlighted that the full DNS Reynolds stress divergence is built by all the harmonics whereas in the self-consistent model it is constituted only by the leading eigenmode of the mean flow, which is approximatively neutrally stable. Both, the self-consistent and fully nonlinear Reynolds stress divergence present similar amplitude and spatial distribution concentrating the forcing close to the cylinder. The Reynolds stress forcing acts on their corresponding mean flows by pushing downstream the recirculation region of the base flow (Fig. 2.1) thus reducing its streamwise length, consistent with the recirculation length difference between the mean and the base flow (Noack *et al.* (2003); Barkley (2006); Zielinska *et al.* (1997)).

Fig. 2.3 compares the frequency predicted by the present self-consistent saturation model with experimental and DNS data for different Reynolds number. Due to the ressemblance of the model and exact mean flows, it does not come as a surprise that the leading eigenfrequency of the present model falls onto the experimental data, as does the eigenfrequency of the linearly least stable mode of the real mean flow, as described by Barkley (2006). On the contrary, the unstable base flow considerably underestimates the experimental frequency.

The amplitude of the perturbation, defined as $A = \|\boldsymbol{u}'\|_{L^2}$, varying with the Reynolds number is compared in Fig. 2.4 for the DNS, self-consistent and the amplitude approximation of the weakly nonlinear theory. The weakly nonlinear theory is valid only close to the critical Reynolds number as it start to diverge from both the DNS and self-consistent results for $Re > 50$. This is because the weakly nonlinear theory is based on a perturbative expansion around threshold (Sipp & Lebedev (2007)), which is unsuitable to describe spatial variations of the oscillating mode (Dušek *et al.* (1994)) and yields an overestimated amplitude at saturation. In the self-consistent model this limitation is relaxed and the resulting amplitude follows the DNS results, indicating that the main nonlinear effects responsible for saturation are well captured in the coupling of the mean flow and perturbation equations in (2.5). As the Reynolds number increases, however, the number of iterations required for our direct method to converge to $\sigma_1^* = 0$ becomes increasingly large. Similar issues for converging to steady solutions of the NSE when increasing Re have been reported in the literature, see (Fornberg (1980)) for instance.

2.4 Discussion and conclusions

The resolution of system (2.5) provides an excellent approximation of the mean flow velocity field and the perturbation's amplitude, frequency and spatial structure of the Reynolds stress forcing. Moreover, Eqs. (2.4) constitute a self-consistent model which formalizes and supports the idea of an instability saturation process wherein the perturbation, given by the most unstable eigenmode, grows around the mean flow and modifies it, saturating when the mean flow is marginally stable (Stuart (1958); Maurel *et al.* (1995); Barkley (2006)), in a way reminiscent to Malkus (1956) notions.

Note that some flows present positive growth rate when linear stability is computed around the mean flow (Sipp & Lebedev (2007)), probably due to the neglected nonlinear terms in the perturbation equation (2.4) and the presence of higher harmonics. Nonetheless, the present model is expected to work for other laminar globally unstable flows dominated by a single harmonic and with a marginally stable mean flow. This includes flows reaching limit cycles above the bifurcation e.g. wakes, hot jets, mixing layers with counterflow, swirling jets, etc. but this excludes aperiodic, chaotic and turbulent flows. In addition, the model can be generalized to harmonic forcing response in stable cases. This can be done by applying a source term in the RHS of (2.5b) and replacing the unstable mode by the linear response to the forcing at a given frequency in (2.5a). This methodology can be used to include higher harmonics in the present case, adding linear equations for the higher harmonics as forced by the nonlinear interactions of the unstable mode.

The present quasi-linear self-consistent model is, for laminar flows, a deterministic counterpart of similar stochastic models recently developed to describe coherent structures in turbulent flows (Farrell & Ioannou (2012); Bakas & Ioannou (2014)). It may open new possibilities as a model reduction for flow control (Noack *et al.* (2003)), since the coupled mean

flow–perturbation equations are solved as a closed system independent of time, allowing the calculation of a mean flow approximation *a priori* without requiring the full time evolution simulation for the a posteriori mean flow extraction.

3 | Revisited mean flow and transient dynamics for an unstable open flow

In this chapter, we revisit the self-consistent model applied to the cylinder flow providing more details of the saturated flow, interpreting the mean flow as a phase average. This new view allows the amplitude A of the unstable mode, which links the manifold of the coupled solutions of the self-consistent model from the base flow to the mean flow, to be reinterpreted as a slow time variation. The instantaneous mean flow along with its corresponding unstable mode are thereby evolving in a slow time scale compared to the oscillations.

Paper: *A self-consistent model for the saturation dynamics of the vortex shedding around the mean flow in the unstable cylinder wake*

A self-consistent model for the saturation dynamics of the vortex shedding around the mean flow in the unstable cylinder wake

Vladislav Mantič-Lugo[1], Cristóbal Arratia[1,2] and François Gallaire[1]

1) LFMI, École Polytechnique Fédérale de Lausanne, CH-1015 Lausanne, Switzerland

2) Departamento de Fsíca, FCFM, Universidad de Chile, Casilla 487-3, Santiago, Chile

The supercritical instability leading to the Bénard-von Karman vortex street in a cylinder wake is a well known example of supercritical Hopf bifurcation: the steady solution becomes linearly unstable and saturates into a periodic limit cycle. Nonetheless, a simplified physical formulation accurately predicting the transition dynamics of the saturation process is lacking. Building upon our previous work, we present here a simple self-consistent model that provides a clear description of the saturation mechanism in a quasi-steady manner by means of coupling the instantaneous mean flow with its most unstable eigenmode and its instantaneous amplitude through the Reynolds stress. The system is coupled for different oscillation amplitudes, providing an instantaneous mean flow as function of an equivalent time. A transient physical picture is described, wherein a harmonic perturbation grows and changes in amplitude, frequency and structure due to the modification of the mean flow by the Reynolds stress forcing, saturating when the flow is marginally stable. Comparisons with direct numerical simulations show an accurate prediction of the instantaneous amplitude, frequency and growth rate, as well as the saturated mean flow, the oscillation amplitude, frequency and the resulting mean Reynolds stresses.

3.1 Introduction

The onset of the Bénard-von Karman (von Karman (1911)) vortex street in the cylinder wake is a classical example of supercritical Hopf bifurcation: above the critical threshold of $Re = 47$ (Provansal *et al.* (1987)), a self-sustained time-periodic pattern of regularly spaced alternated vortices emerges, which is shed at a well-defined frequency. This threshold could be retrieved theoretically (Zebib (1987); Jackson (1987); Noack *et al.* (2003)) using a linear stability analysis around the base flow, the steady solution of the Navier-Stokes equations (NSE), which provided in addition an accurate frequency prediction at the critical Reynolds number. However, the linear frequency prediction departs immediately after threshold from the experimental measurements or direct numerical simulations (DNS) of the full nonlinear Navier-Stokes equations.

More generally this instability is an archetypical test case for developing formulations and theoretical concepts. Some examples are the computation of the instability threshold on

numerically obtained solutions of the Navier-Stokes equations (Zebib (1987); Jackson (1987)), the experimental determination of the Landau constants for the description of the bifurcation with an amplitude equation (Provansal *et al.* (1987)), the understanding of the appearance of the global instability as the development of a region of absolute instability (Triantafyllou *et al.* (1986); Chomaz *et al.* (1988)), the construction of reduced models for flow control (Noack *et al.* (2003); Tadmor *et al.* (2010)) as well as an interesting test-bed for sensitivity analysis and optimal open loop control design (Strykowski & Sreenivasan (1990); Giannetti & Luchini (2007); Marquet *et al.* (2008); Boujo & Gallaire (2014)).

A key ingredient to a correct description of the dynamics above threshold is to properly capture the effective mean flow that results from the additional distortion caused by the retro-action of the quadratic contributions (the Reynolds stresses) of the fluctuating structures onto the steady flow component (Barkley (2006); Stuart (1958); Maurel *et al.* (1995)). In the cylinder wake flow above threshold, the frequency prediction based on the linear stability analysis of the mean flow outperforms the frequency prediction of the dominant eigenmode of the base flow solving the NSE (Triantafyllou *et al.* (1986); Hammond & Redekopp (1997); Pier (2002); Barkley (2006); Mittal (2008)). In addition, it also sheds light on the nonlinear saturation mechanism: perturbations to the unstable flow induce mean flow modifications that increase while perturbations grow, until the point at which the mean flow becomes neutrally stable (Barkley (2006); Mittal (2008)) and perturbations saturate, as formulated early by Malkus (1956) in the context of turbulent flows. This is also the main idea behind Stuart's (Stuart (1958)) initial simplified model wherein the mean flow is only affected by the Reynolds stress divergence of the most unstable eigenmode of the unperturbed base flow. This focus on the mean flow distortion by finite perturbations was later dropped by Stuart in favor of a more rigorous perturbative analysis of the Navier-Stokes equations close to threshold (Stuart (1960)), which yields the well-known Stuart-Landau amplitude equation.

The rigorous application of Stuart's mutiple-scale expansion method to the cylinder wake flow by Sipp & Lebedev (2007) yields a Stuart-Landau amplitude equation that captures well the nascent nonlinear saturation mechanisms and correctly predicts the nonlinear frequency correction in the vicinity of the instability threshold $Re = 47$. The absence of any adjustable parameter is remarkable in comparison to the empirical approach where the Stuart-Landau amplitude equation is chosen so as to reproduce the qualitative aspects of the saturation of the instability with empirically-tuned coefficients (Dušek *et al.* (1994)). Sipp & Lebedev (2007) also showed that the marginal stability property of the mean flow was not generic but intimately linked to the dominance of the fundamental harmonic in the periodic signal.

However, despite the elegance and rigorousness of the multiple-scale expansion method, its perturbative nature limits its validity to the immediate vicinity of the threshold. Thus, it quickly fails to capture the saturated flow since the perturbation of the amplitude equation is fixed around the unperturbed base flow (Dušek *et al.* (1994); Noack *et al.* (2003).) More precisely, it fails to provide correct nonlinear frequency corrections at Reynolds numbers which are only 10% above the bifurcation threshold. This opens the question of whether one can formulate a

consistent and accurate prediction of the saturation amplitude and perturbation by retaining some of the nonlinear terms, or if only direct numerical simulations of the full nonlinear Navier-Stokes equations or careful experiments can provide an accurate description of the dynamics.

Recently, building on Malkus' marginal stability criterion and on Barkley's observation, the authors proposed a quasilinear self-consistent model: the full nonlinear distortion of the mean flow caused by the Reynolds stresses is taken into account but the fluctuation structure is obtained from a linearized disturbance equation (Mantič-Lugo *et al.* (2014)). These two equations are solved together in a self-consistent coupled way, with the scalar amplitude A of the disturbance as sole free parameter. For a specific value of the amplitude A^*, the mean flow is found to be marginally stable, yielding an approximation of the mean flow as well as the fluctuating structure, its frequency and amplitude. The predicted frequency compared very well to that obtained from DNS, for Reynolds number as high as $Re = 100$.

In this description of the stationary limit cycle (Mantič-Lugo *et al.* (2014)), the amplitude A was treated as an external parameter controlling the amplitude of the leading eigenmode. In the present paper, we consider A as a dynamical variable reflecting the evolution in time of the amplitude of the leading eigenmode, whose instantaneous growth rate is given by the real part of its leading eigenvalue. The purpose of this paper is therefore two-fold: (i) first, we quantify the accuracy of the approximation of the limit-cycle by the marginal self-consistent solution $(\mathbf{U}^*, \mathbf{u}'^*, \omega^*, A^*)$. (ii) Second, we show that the family of self-consistent solutions can also be used to describe the transient evolution of the flow starting from a small disturbance added to the base flow at time $t = 0$ and reaching the limit-cycle after the transient has died out. This amounts to a quasi-static approximation where the amplitude of the mode grows according to its instantaneous growth-rate until it saturates. In contrast to the approach of Thiria *et al.* (2015), who have shown the relevance of this quasi-static approach using a weakly non parallel stability analysis of the instantaneous mean flow, averaged on the fly from DNS data, the quasi-static mean flow is here rather obtained as a result of the model.

Section II introduces the formulation used throughout the whole paper and presents the quasi-linear model in a general setting. Section III defines the physical domain and the numerical framework in which the model is applied. Section IV describes the method developed to solve the model. The results of the cylinder mean flow calculation and the transient dynamics are presented in Secs. V and VI, ending with comments and conclusions.

3.2 Formulation and self-consistent quasi-linear model

3.2.1 Instability onset and transient dynamics

We consider a two dimensional (2D) flow with uniform velocity $U_\infty \boldsymbol{e}_x$ and viscosity ν incident on a cylinder of diameter D centered at the origin. The flow is governed by the 2D

incompressible Navier-Stokes equations (NSE)

$$\partial_t \boldsymbol{u} + N(\boldsymbol{u}) = 0, \tag{3.1}$$

where

$$N(\boldsymbol{u}) \equiv (\boldsymbol{u} \cdot \nabla)\boldsymbol{u} + \nabla p - Re^{-1}\Delta \boldsymbol{u}, \tag{3.2}$$

corresponds to advection, diffusion and the gradient of the pressure p required to impose incompressibility

$$\nabla \cdot \boldsymbol{u} = 0. \tag{3.3}$$

Throughout the article, all the variables are non-dimensionalized using length D and velocity U_∞ as reference scales, and the sole physical parameter is the Reynolds number $Re \equiv U_\infty D/\nu$. The NSE can be equivalently written for the velocity $\boldsymbol{u}' = \boldsymbol{u} - \overline{\boldsymbol{U}}$ relative to some stationary reference flow $\overline{\boldsymbol{U}}$, i.e.

$$\partial_t \boldsymbol{u}' + L_{\overline{\boldsymbol{U}}}(\boldsymbol{u}') + N(\overline{\boldsymbol{U}}) = -(\boldsymbol{u}' \cdot \nabla)\boldsymbol{u}', \tag{3.4}$$

where

$$L_{\overline{\boldsymbol{U}}}(\boldsymbol{u}') \equiv (\overline{\boldsymbol{U}} \cdot \nabla)\boldsymbol{u}' + (\boldsymbol{u}' \cdot \nabla)\overline{\boldsymbol{U}} + \nabla p' - Re^{-1}\Delta \boldsymbol{u}', \tag{3.5}$$

is the operator for the NSE linearized around $\overline{\boldsymbol{U}}$.

The onset of the vortex shedding instability can be understood from linear stability analysis, in which $\overline{\boldsymbol{U}}$ corresponds to a steady solution $\boldsymbol{U}_B$ of the NSE

$$N(\boldsymbol{U}_B) = 0, \tag{3.6}$$

which is called the base flow, and $\boldsymbol{u}'$ is considered sufficiently small so that (3.4) becomes

$$\partial_t \boldsymbol{u}'_B + L_{\boldsymbol{U}_B}(\boldsymbol{u}'_B) = 0. \tag{3.7}$$

The solutions of this linearized perturbation equation can be expanded in the basis of eigenmodes $\boldsymbol{u}_{nB}$ with their corresponding eigenvalues $\lambda_{nB} = \sigma_{nB} + i\omega_{nB}$, $n = 1, 2, \ldots, \infty$ sorted by decreasing real part. The (large-time asymptotic) growth rate σ is given by the most unstable eigenvalue pair $(\lambda_1, \bar{\lambda}_1)$ as $\sigma \equiv \sigma_1 = \Re(\lambda_1)$, while the frequency corresponds to the imaginary part $\omega \equiv \omega_1 = \Im(\lambda_1)$, the overbar represents complex conjugate. The linear equation (3.7) yields $\boldsymbol{u}'_{1B} = A_0 \boldsymbol{u}_{1B} e^{(\lambda_{1B} t + i\phi_0)} + A_0 \bar{\boldsymbol{u}}_{1B} e^{(\bar{\lambda}_{1B} t - i\phi_0)}$, as solution for an initial condition based on the most unstable eigenmode $\boldsymbol{u}'_0 = A_0 \boldsymbol{u}_{1B} e^{i\phi_0} + A_0 \bar{\boldsymbol{u}}_{1B} e^{-i\phi_0}$, which will be used throughout the paper, where ϕ_0 in $[0, 2\pi]$ is the phase determined in the initial condition. The amplitude of $\boldsymbol{u}'_0$ is A_0 since $\boldsymbol{u}_{1B}$ is normalized as $\sqrt{2}\|\boldsymbol{u}_{1B}\| = 1$. The norm $\|.\|$ is an L^2 norm determined by the Hermitian inner product $(\boldsymbol{a}|\boldsymbol{b}) = \int_\Omega \overline{\boldsymbol{a}} \cdot \boldsymbol{b} d\Omega = \int_\Omega \boldsymbol{a}^H \cdot \boldsymbol{b} d\Omega$, for complex fields in the

domain Ω.
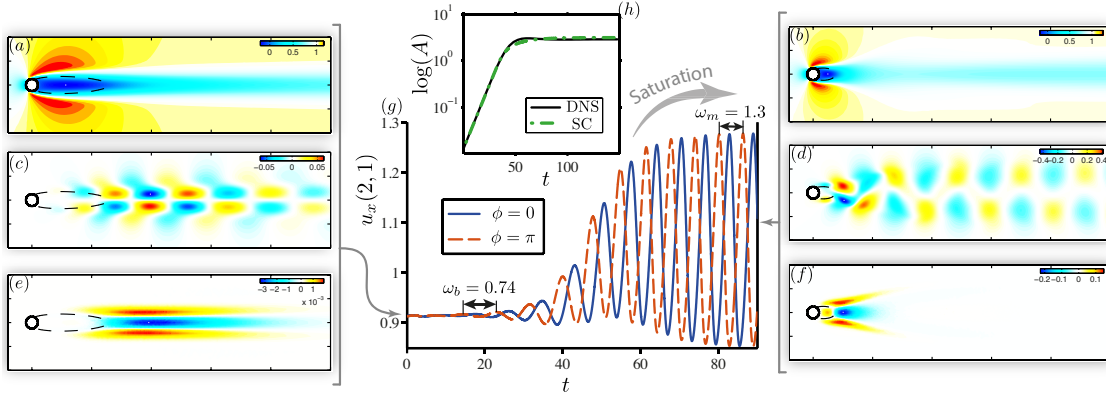
Figure 3.1 – Velocity fields in x-direction; (a) base flow $\boldsymbol{U}_{Bx}$ and (b) mean flow $\boldsymbol{U}_x$. (c) The most unstable eigenmode $\boldsymbol{u}_{1Bx}$ from stability analysis (3.7) around base flow $\boldsymbol{U}_B$. (d) Fluctuation snapshot $\boldsymbol{u}'$ around the saturated mean flow $\boldsymbol{U}$. Reynolds stress divergence $\langle(\boldsymbol{u}'\cdot\nabla)\boldsymbol{u}'\rangle$, x-direction component for the: (e) eigenmode of the base flow and (f) fluctuation around the mean flow. (g) Transient of velocity in the x-direction at the point ($x=2, y=1$) for two initial conditions shifted by π. The change of frequency is marked by the arrow length. (h) Transient evolution of the fluctuation amplitude amplitude $A(t)$ for the DNS (solid line) and self-consistent model (dashed line). All solutions are for $Re = 100$.

At threshold $Re_{cr} \approx 47$ the growth rate σ turns positive, the base flow becomes unstable (Jackson (1987); Zebib (1987)) and the system undergoes a supercritical Hopf bifurcation (Provansal *et al.* (1987)). The development of the instability for $Re = 100$ is shown in Fig. 3.1. The unstable global mode of the base flow (shown in Fig. 3.1(c)) is the infinitesimal structure that grows from the base flow solution (Fig. 3.1a). As it evolves in time (see Fig. 3.1g) and the nonlinear terms in the right-hand side (RHS) of (3.4) become important, this unstable structure gets modified in space and saturates in a time periodic solution with a new frequency and a finite amplitude. Above threshold, the system eventually settles in a limit cycle with a frequency and spatial structure which are different from the initial perturbation (Dušek *et al.* (1994)), as can be seen in Figs. 3.1(b) and 3.1(d) showing the mean flow and a snapshot of the corresponding $\boldsymbol{u}'$ as defined below.

Fig. 3.1(g) displays the transient of the x-direction velocity at the point ($x=2, y=1$) for two initial conditions composed of the eigenmode with different phase ϕ_0 and the same amplitude A_0. There are two different time scales involved in the development of the instability: a fast time scale associated to the shedding of alternating vortices and a slower one associated to the growth in amplitude of the corresponding velocity oscillations. These two time scales are initially given by the inverse of the real and imaginary parts of the unstable eigenmode; this scale separation becomes arbitrarily large as the Reynolds number Re approaches threshold. As done by Sipp & Lebedev (2007), this can be used to perform a weakly nonlinear perturbative expansion leading to a Stuart-Landau equation for the amplitude of the unstable mode, which is valid only close to threshold (Fig. 3.9).

The present description of the transient development and the saturated flow of the instability also exploits this separation of scales: it is performed by means of a Reynolds decomposition. We define $\boldsymbol{U}(t)$ as the phase averaged mean flow $\boldsymbol{U} = \langle \boldsymbol{u} \rangle$, where $\langle \cdot \rangle$ denotes the average on the phase ϕ_0 of the fluctuation. By construction, the fluctuation $\boldsymbol{u}'$ is such that $\langle \boldsymbol{u}' \rangle = 0$. This phase average corresponds to an integral over the oscillation (fast) scale only, and allows a simple separation of time scales during the transient while being equivalent to a time average in the saturated regime. Thereby, in practice, for a given specific time τ the corresponding instantaneous mean flow $\boldsymbol{U}(\tau)$, or average over the phase, is given by averaging along the full velocity $\boldsymbol{u}(\tau)$ of several DNS simulations with initial conditions $\boldsymbol{u}'_0$ of the same amplitude A_0 and shifted in ϕ_0 as depicted in Fig. 3.1(g) for two ϕ_0 shifted by π.

Inserting this mean flow decomposition $\boldsymbol{u} = \boldsymbol{U} + \boldsymbol{u}'$ in the 2D NSE yields

$$N(\boldsymbol{U}) = -\langle (\boldsymbol{u}' \cdot \nabla) \boldsymbol{u}' \rangle, \tag{3.8a}$$

$$\partial_t \boldsymbol{u}' + L_{\boldsymbol{U}}(\boldsymbol{u}') = -(\boldsymbol{u}' \cdot \nabla) \boldsymbol{u}' + \langle (\boldsymbol{u}' \cdot \nabla) \boldsymbol{u}' \rangle, \tag{3.8b}$$

where the time derivative term $\partial_t \boldsymbol{U}$ on the left-hand side (LHS) of (3.8a) has been neglected. This term reflects the slow deformation of the mean flow which is null in the stationary regime and small but non-zero during the transient; neglecting this term amounts to a quasi-static approximation slaving the mean flow $\boldsymbol{U}$ to the forcing by $\boldsymbol{u}'$ given in the RHS of (3.8a). Note, however, that the fluctuation $\boldsymbol{u}'$ does not have to be small compared to the mean $\boldsymbol{U}$. The amplitude of the fluctuation is defined as the square root of the phase averaged kinetic energy,

$$A = \sqrt{\frac{1}{2\pi} \int_0^{2\pi} \int_\Omega \boldsymbol{u}'^2 \, d\Omega \, d\phi_0} = \sqrt{\langle \int_\Omega \boldsymbol{u}'^2 \, d\Omega \rangle}, \tag{3.9}$$

which corresponds to a temporal average over a period for a harmonic fluctuation. The amplitude A at $t = 0$ coincides with the amplitude of the initial condition A_0 explaining the choice of $\sqrt{2} \| \boldsymbol{u}_{1B} \| = 1$.

The system (3.8) is composed of two coupled equations. In the stationary regime, the mean flow $\boldsymbol{U}$ is a solution of the steady mean flow equation (3.8a), while the fluctuation equation (3.8b) describes the fluctuating field $\boldsymbol{u}'$. As described briefly in Mantič-Lugo *et al.* (2014), there are different nonlinear effects in (3.8), two of which are dominant for the development of the instability.

- First, the RHS of (3.8a) corresponds to minus the Reynolds stress divergence $\langle (\boldsymbol{u}' \cdot \nabla) \boldsymbol{u}' \rangle$, a nonlinear mean momentum addition of the time dependent fluctuation $\boldsymbol{u}'$ on $\boldsymbol{U}$. The x-component of this forcing term is shown in Fig. 3.1 for the initial $\boldsymbol{u}'$ given by the unstable eigenmode of the base flow (Fig. 3.1(e)) and for the final periodic state (Fig. 3.1(f)). This momentum addition can be also viewed as the body force required for the mean flow $\boldsymbol{U}$ to become a stationary solution of the NSE. Fig. 3.1(b) shows that the mean flow $\boldsymbol{U}$ prevailing once the limit cycle has been reached, presents a much shorter

recirculation bubble and less shear in the wake than the base flow U_B (Fig. 3.1(a)), (Maurel *et al.* (1995)).

- The second nonlinear effect in (3.8) which is relevant for the instability is that of the mean flow U on u', which is contained in the advection terms of $L_U(u')$ present in the fluctuation equation (3.8b). This includes the advection of u' by U (i.e. $(U \cdot \nabla)u$) and the source terms $((u \cdot \nabla)U)$ responsible for the energy transfer associated to the growth in amplitude of the fluctuations. These effects are included in the various linear stabiliy analyses performed around mean flows (Triantafyllou *et al.* (1986); Hammond & Redekopp (1997); Pier (2002); Barkley (2006); Mittal (2008)), which neglect the RHS of (3.8b) and in practice ignore (3.8a), since the mean flow is usually obtained from DNS or experimental data. As remarked by Barkley (2006), such a linear stability analysis performed globally around the mean flow U provides a very good frequency prediction with a growth rate very close to zero.

- The third nonlinear effect, seen in the RHS of (3.8b), $(u' \cdot \nabla)u' - \langle (u' \cdot \nabla)u' \rangle$, represents the time dependent, zero mean, momentum addition from the nonlinear interactions of u' at different frequencies, resulting from the nonlinear interactions between higher harmonics.

Neglecting this last nonlinear term as a consequence of the very harmonic nature of the periodic limit cycle, the flow dynamics can be understood as a base flow that develops an instability which grows and forces the underlying flow through the Reynolds stress divergence $\langle (u' \cdot \nabla)u' \rangle$. Initially, the Reynolds stress divergence of the unstable global mode, depicted in Fig. 3.1(e), forces the base flow (Fig. 3.1(a)) modifying it towards the mean flow (Fig. 3.1(b)), until the point at which the mean flow is (almost) marginally stable and the perturbation saturates into a limit cycle with a certain amplitude and frequency. In this process, the Reynolds stress forcing of the initial perturbation (Fig. 3.1(e)) is modified and migrates upstream, as can be seen by comparing it with the Reynolds stress of the saturated flow in Fig.3.1(f).

Because the mean flow provides a very good prediction of the vortex shedding frequency with an essentially zero growth rate, it is tempting to imagine that the NSE linearized around the instantaneous mean flow (3.7) could approximate the instantaneous frequency and growth-rate of the evolving vortex shedding. Thiria *et al.* (2015) have indeed confirmed this suggestion, using a weakly non parallel stability analysis of instantaneous mean flows obtained from DNS simulations. It must be noted, however, that there is no amplitude information in such a linear approach. The objective of the present paper is to show that the self-consistent model (Mantič-Lugo *et al.* (2014)) provides a fairly accurate and fully consistent description of the transient dynamics involved in the passage from the unstable base flow (Fig. 3.1(a,c,e)) to the fully saturated mean flow with vortex shedding (Fig. 3.1(b,d,f)).

3.2.2 Self-consistent model

As introduced by Mantič-Lugo *et al.* (2014) the self-consistent model relies on the much larger amplitude of the fundamental compared to the rest of harmonics. For the present case of the cylinder, Fig. 3.2 shows the structures of the velocity and energy of the fundamental and second harmonic extracted from the fluctuation field $\boldsymbol{u}'$ around the mean flow computed from DNS (from now on denoted $\boldsymbol{U}_{DNS}$, leaving $\boldsymbol{U}$ for the mean flow of the model). The leading terms of the Fourier series are computed from the DNS' temporal signal at each spatial point to extract the dominant frequencies. The power spectra of the vortex shedding signal is strongly dominated by the fundamental frequency, with decaying energy of the higher harmonics (Dušek *et al.* (1994)). This fundamental frequency dominance can also be seen in Fig. 3.2, where the energy of the second harmonic is less than 3% of the fundamental.
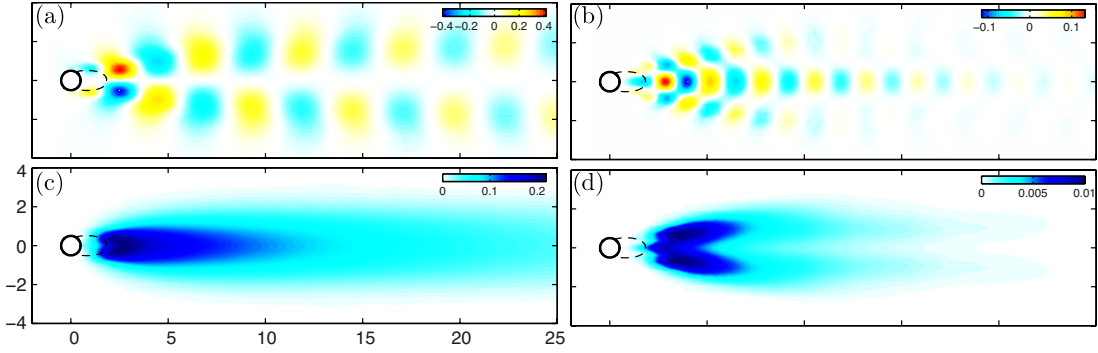
Figure 3.2 – Fluctuation velocity in x-direction u_x; (a) fundamental frequency ω and (b) second harmonic 2ω extracted from the fully nonlinear DNS fluctuating field $\boldsymbol{u}'(\boldsymbol{x}, t)$ by Fourier series. Energy of the fluctuation; (c) fundamental frequency ω, $E_\omega = \int_\Omega \boldsymbol{u}_\omega^2 d\Omega = 7.6$ and (d) second harmonic 2ω, $E_{2\omega} = \int_\Omega \boldsymbol{u}_{2\omega}^2 d\Omega = 0.16$. $Re = 100$.

This dominance of the fundamental harmonic supports that the RHS of (3.8b), which is responsible for energy transfers between different frequencies, is of limited importance and is therefore neglected in the model (Mantič-Lugo *et al.* (2014)). Hence, the perturbation equation (3.8b) is simplified neglecting the nonlinear RHS, corresponding to a global linear stability analysis around the mean flow. Furthermore, the model assumes that this fundamental frequency structure is directly given by the most unstable mode of the linear stability analysis around the mean flow. In addition, the mean flow is not extracted from DNS or experimental values, but given from (3.8a) with the forcing of the most unstable eigenmode, forming a closed system of interactions. The resulting self-consistent quasilinear model is written:

$$N(\boldsymbol{U}) = -2A^2 \Re\left((\bar{\boldsymbol{u}}_1 \cdot \nabla)\boldsymbol{u}_1\right), \tag{3.10a}$$

$$\lambda_1 \boldsymbol{u}_1 + L_{\boldsymbol{U}}(\boldsymbol{u}_1) = 0, \tag{3.10b}$$

where $\Re(\cdot)$ denotes the real part and $A > 0$ is the instantaneous amplitude in the L^2 norm (3.9) of the first eigenmode pair. Thus, the full instantaneous velocity field is approximated as
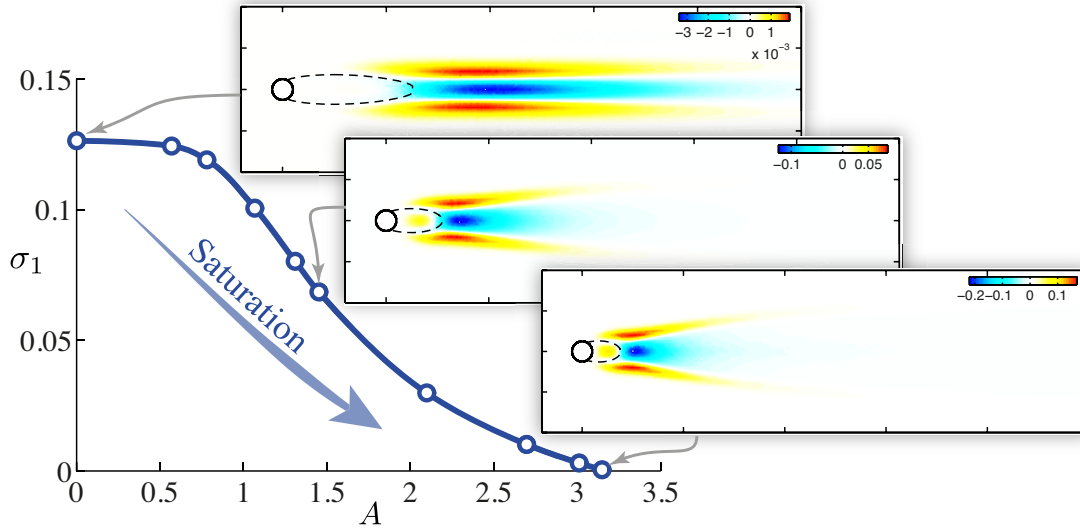
Figure 3.3 – Growth rate σ_1 for the converged coupled system of equations of the SC model (3.10) for different perturbation $\boldsymbol{u}_1$ amplitude A at $Re = 100$. The insets show the structure of the Reynolds stress divergence $2A^2 \Re((\bar{\boldsymbol{u}}_1 \cdot \nabla)\boldsymbol{u}_1)$ in the x-direction and the boundary of the recirculation bubble.

$\boldsymbol{u}(x, t) = \boldsymbol{U}_{DNS}(x) + \boldsymbol{u}'(x, t) \simeq \boldsymbol{U}(x) + \boldsymbol{u}'_1(x, t)$, where $\boldsymbol{u}'_1(x, t) = A\boldsymbol{u}_1(x)e^{((\sigma_1 + i\omega_1)t)} + cc.$ with ω_1 the frequency and σ_1 the growth-rate.

The solution of (3.10) for a given A proceeds exactly as in Mantič-Lugo *et al.* (2014), also described in more detail in section 3.4. The amplitude A of the leading eigenmode $\boldsymbol{u}'_1$ of $\boldsymbol{U}$ is initially treated as an external parameter allowing us to find a family of coupled mean flow $\boldsymbol{U}(A)$ and perturbation $\boldsymbol{u}_1(A)$ solutions with their corresponding growth rate $\sigma_1(A)$ as function of the amplitude A (Fig. 3.3).

Following the physical saturation process previously described, the growth rate σ_1 resulting from these computations decreases with the amplitude increase A, as shown in Fig. 3.3. Simultaneously, the Reynolds stress forcing constructed from the most unstable eigenmode migrates upstream with increasing amplitude A (insets in Fig. 3.3) progressively reshaping the mean flow and stabilizing it. The upstream relocation of the Reynolds stress divergence forces the contraction of the recirculation region on the corresponding mean flow, marked by a dashed line in the insets. The recirculation bubble shortening was reported in previous descriptions of the differences between the base and the mean flow (Barkley (2006); Noack *et al.* (2003)) and has been argued to be as a critical factor in the instability saturation mechanism (Zielinska *et al.* (1997)).

Subsequently, the amplitude $A = A(t)$ can be also interpreted as a dynamical variable reflecting the evolution in time of the amplitude of the leading eigenmode, whose instantaneous growth rate is given by the leading eigenvalue as $\sigma_1 = \Re(\lambda_1)$. That is, the self-consistent model (3.10)

is extended to account for the transient dynamics by adding the equation

$$\frac{dA(t)}{dt} = A(t)\sigma_1(A),\tag{3.11}$$

which links, through the growth rate $\sigma_1(A)$ (Fig. 3.3), the family of $(\boldsymbol{U}, \boldsymbol{u}_1)$ solutions of (3.10) for different A to the development in time of the instability.

The relevant range of the amplitude A goes from $A = 0$, which corresponds to the base flow solution $\boldsymbol{U}_B$ with its unstable eigenmode, up to an amplitude A^* such that $\sigma_1(A^*) = 0$, which yields a stationary solution of (3.11) that corresponds to the saturated vortex shedding state. The problem of finding the amplitude A^* corresponding to this saturated state can be rewritten by adding the constraint $\sigma_1 = 0$ in (3.10) and we get

Find: $A^* > 0$ such that: $\sigma_1^* = 0$, for
$$N(\boldsymbol{U}^*) = -2A^{*2}\Re\left((\bar{\boldsymbol{u}}_1^* \cdot \nabla)\boldsymbol{u}_1^*\right),\tag{3.12a}$$
$$i\omega_1^* \boldsymbol{u}_1^* + L_{\boldsymbol{U}^*}(\boldsymbol{u}_1^*) = 0.\tag{3.12b}$$

Summarizing, the system (3.10) together with (3.11) constitute a self-consistent closed model of the base flow stabilization process from the unstable base flow $\boldsymbol{U}_B$ to a marginally stable mean flow $\boldsymbol{U}^*$ given by (3.12). It approximates the slow time evolution of the transient dynamics by means of a quasi-static approximation of the instantaneous mean flow $\boldsymbol{U}(A(t))$, which is parametrized by the amplitude A. The model is based on the nonlinear coupling between the mean flow equations and the linear stability equations through the Reynolds stress.

3.3 Computational details

The computational domain is defined in Cartesian coordinates with center in the cylinder, its nominal size is characterized by $x_{-\infty} = y_\infty = y_{-\infty} = 20D$ distance to upstream, upper and lower boundaries respectively and $x_\infty = 40D$ distance to the outlet boundary. The nominal mesh, C_3 in Tab. 3.1, has 13322 cells and 6731 vertices being locally clustered around the cylinder and the wake region. The Dirichlet boundary condition $(u_x, u_y) = (1, 0)$ is used at the inlet $x = x_{-\infty}$, upper $y = y_\infty$ and lower $y = y_{-\infty}$ side boundaries. No-slip condition $(u_x, u_y) = (0, 0)$ is applied on the cylinder boundary $x^2 + y^2 = D^2/4$ and outflow boundary condition is applied at the outlet $x = x_\infty$.

The linear and nonlinear Navier-Stokes equations are discretized and solved using the finite element method. Taylor-Hood (P2,P2,P1) elements are used representing (u_x, u_y, p) for the spatial discretization. The time discretization of the DNS (Direct Numerical Simulation) of NSE solution is done applying an implicit first-order time scheme based on Characteristics-Galerkin method with a $\delta t = 0.02s$. FreeFEM++ is used to handle and solve the linear and nonlinear systems of equations and to build the matrices of the generalized eigenvalue problem which is solved by means of the SLEPc software.

Mesh	$x_{-\infty} = y_\infty$	x_∞	N nodes	Base flow, Re=60, λ_B
C1	20	20	2867	$0.0488 + 0.761i$
C2	20	40	4755	$0.0490 + 0.761i$
C3	20	40	6731	$0.0491 + 0.761i$
C4	20	40	15862	$0.0493 + 0.760i$
C5	30	80	10390	$0.0478 + 0.752i$
C6	40	120	68215	$0.0472 + 0.748i$
C7	30	200	123412	$0.0474 + 0.750i$
Barkley (2006)				$0.0496 + 0.757i$

Table 3.1 – Comparison of the most unstable eigenvalue λ_B of the linear global stability analysis (3.7) on the base flow U_B at $Re = 60$ for different mesh size and resolution.

The numerical approach is validated comparing in Tab. 3.1 the unstable eigenvalue of the base flow at $Re = 60$ for seven meshes with different resolution and sizes and the results obtained in Barkley (2006). Based on the good agreement between the values in Tab. 3.1 the mesh C3 is selected to be the nominal mesh as its resolution is deemed to be enough. In addition, the critical Reynolds number for the mesh C3 is $Re_{cr} = 46.7$ varying less than 1% compared to $Re_{cr} = 46.3$ presented in Barkley (2006), which base flow and mean flow are also compared to the present approach in Fig. 3.9a together with experimental results for different Reynolds number showing an excellent agreement. Having in mind that the aim of this paper is physical analysis and model presentation, the mesh selection is a compromise between sufficient mesh resolution and computational costs due to the large amount of linear stability computations required to converge the coupled equations.

3.4 Model solution

The core of the model and the most difficult part of solving it is given by the coupled system of equations (3.10), which for each amplitude A requires finding a mean flow which is generated by the Reynolds stress divergence of its own leading eigenmode. This is a non-standard problem, but once it is solved and the growth rate $\sigma(A)$ known in the relevant range of amplitudes, solving (3.12) to obtain the transient dynamics is straightforward. The solution of the model is found by means of two nested iterative loops: an inner loop to solve (3.10) for a particular value of A, and an outer loop to solve (3.12) by increasing A from 0 to A^* required to advance from the unstable base flow U_B to the marginally stable mean flow U while capturing the transient dynamics.

Inner loop: equation coupling $\lambda_1(A)$ The iterative solution of (3.10) starts with an initial guess for U, in this case the base flow U_B. The corresponding eigenmode u_1 is computed from (3.10b), which is then inserted in (3.10a) to compute a new U using the Newton-Raphson

method. This new $\boldsymbol{U}$ is used with a relaxation factor (as described in detail inTab. 3.2) to update the previous guess for a new iteration. This iterative algorithm converges robustly to a solution of (3.10) if the system is controlled by fixing the amplitude of the Reynolds stress forcing $A_f \equiv A^2 \| 2\Re ((\bar{\boldsymbol{u}}_1 \cdot \nabla) \boldsymbol{u}_1) \|$ instead of the amplitude A of the perturbation.

This is intuitive since the amplitude A_f directly governs the size of the forcing term in the RHS in (3.10), which in terms of A_f becomes

$$A^2 2\Re ((\bar{\boldsymbol{u}}_1 \cdot \nabla) \boldsymbol{u}_1) = A_f \frac{2\Re ((\bar{\boldsymbol{u}}_1 \cdot \nabla) \boldsymbol{u}_1)}{\| 2\Re ((\bar{\boldsymbol{u}}_1 \cdot \nabla) \boldsymbol{u}_1) \|}, \tag{3.13}$$

and where we recall that u_1 is of unit L^2 norm (3.9). If the system is controlled by fixing A, the change in shape of $\boldsymbol{u}_1$ between iterations influences the norm of the Reynolds stress $\| 2\Re ((\bar{\boldsymbol{u}}_1 \cdot \nabla) \boldsymbol{u}_1) \|$ which involves derivatives, thus changing the size of the RHS of (3.10) and hindering convergence. In contrast, by fixing A_f the norm of the RHS of (3.10) is kept constant despite changes in the shape of $\boldsymbol{u}_1$. Note that this change in normalization of the Reynolds stress forcing is only due to convergence issues and thus it does not have any influence on the physics of the results, since there is a fixed relation between A and A_f for the converged system (3.10) at each amplitude step A or equivalently A_f.

With fixed A_f, this iterative procedure converges while reducing the growth rate σ_1 and increasing the frequency ω_1, as can be seen in Fig. 3.4a for a case in which a marginally stable region is reached. The residuals Rs are defined as the L^2 norm on the domain Ω of the relative variation of the fields between two consecutive steps $Rs = \| \boldsymbol{U}^{n+1} - \boldsymbol{U}^n \| / \| \boldsymbol{U}^n \|$. They reduce while iterating Fig. 3.4b assuming the solution to be converged when all the residuals are less than $Rs < 10^{-4}$.

Outer loop: amplitude A^*. This parameterizes the slow time evolution of the instantaneous mean along the transient by means of the amplitude A_f of the Reynolds stress forcing and equivalently the amplitude A of the perturbation $\boldsymbol{u}_1$ as it is the free parameter in (3.10). We assume that eventually for a particular value A^* (or A_f^* (3.13)), which is not known a priory, the system (3.12) is marginally stable similarly to the DNS mean flow.

For each amplitude A there is a nonlinear solution of the coupled perturbation-mean flow system (3.10) with a certain growth rate σ_1, frequency ω_1 and perturbation structure $\boldsymbol{u}_1$, with its corresponding Reynolds Stress divergence $2A^2\Re ((\bar{\boldsymbol{u}}_1 \cdot \nabla) \boldsymbol{u}_1)$. Fig. 3.3 presents several of these system solutions for different amplitudes A showing the relation of the growth rate and the amplitude $\sigma_1(A)$.

The growth rate $\sigma_1(A_f)$ for each amplitude A_f is not known until the nonlinear system (3.10) is coupled iteratively. Therefore, in order to asses the transient dynamics and achieve the marginally stable solution $\boldsymbol{U}^*, \boldsymbol{u}_1^*$ with ω_1^*, several steps in A_f are required closing the system (3.10) at each step, in order to obtain the evolution $\sigma_1(A), \boldsymbol{U}(A), \omega_1(A), \boldsymbol{u}_1(A)$.

Coupled system solution. The perturbation-mean flow system (3.12) is solved as described in Tab. 3.2. The relaxation factor required to have a stable convergence in the inner loop

- $U^{n=1} = U_B$ initial condition.
- Select small A_f arbitrarily.
  1. Solve linear stability (3.10b), $U^n \rightarrow u_1^n$
  2. Calculate Reynolds stress forcing, $2\Re((\bar{u}_1 \cdot \nabla)u_1)$
  3. Solve the forced Mean flow equation (3.10a), $u_1^n \rightarrow U^{n+1/2}$
  4. Calculate the new mean flow U^{n+1} to input into the linear stability equation, $U^{n+1} = U^{n+1/2}\gamma + (1-\gamma)U^n$ where $0 \leq \gamma \leq 1$ is a relaxation factor. Residuals Rs should reduce at each step.
  5. Go to Step 1 and repeat till converged: $Rs <$ Tolerance
- If $\sigma_1 > 0$, increase amplitude A_f, go to Step 1, until $\sigma_1^* = 0$, so that $A_f \rightarrow A_f^*$

Table 3.2 – The full double nested iterative procedure that obtains the transient quasi-steady relations of $U(A), u_1(A), \sigma_1(A), \omega_1(A)$ from (3.10) and finds the saturated flow of the self-consistent model $A^*, \omega^*, U^*, u_1^*$, solving the coupled system (3.12).
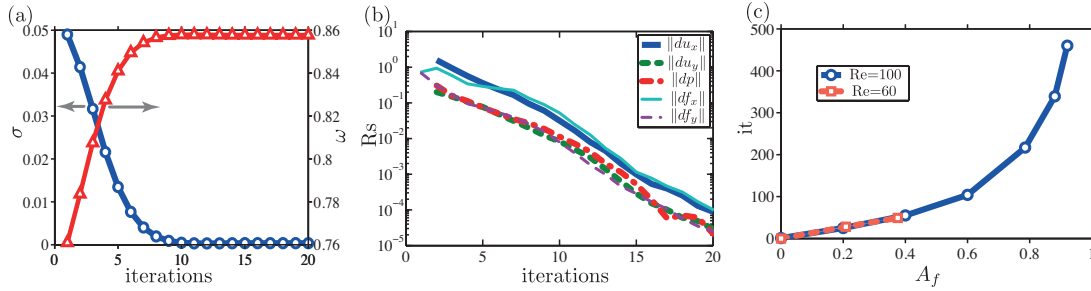
Figure 3.4 – (a) Growth rate and frequency evolution during convergence of the inner loop with fixed Amplitude $A_f = 0.35$ and relaxation factor $\gamma = 0.5$ for $Re = 60$. (b) Residuals Rs of the velocity U, pressure p and Reynolds stress divergence f decrease during converge of (a). (c) Iterations (it) required to converge at different Reynolds number $Re = 60$ and $Re = 100$.

varies from $\gamma = 0.5$ for $Re = 60$ to $\gamma = 0.1$ for the large amplitudes A_f for $Re = 100$. This difference is related to the increased difficulty to converge for $\sigma_1^* = 0$ as the Reynolds number increase as shown in Fig. 3.4c. Similar issues for converging to steady solutions of the NSE when increasing Re have been reported in the literature, see Fornberg (1980) for instance. The required amplitude A^* to saturate the base flow grows with the Reynolds number, entailing an increased number of iterations (it), (Fig. 3.4c). For Reynolds higher than $Re > 110$ the number of iterations required to converge increase rapidly, therefore only partial convergence was achieved for $Re = 120$. Different initial conditions and relaxation values have been tried, all converging to the same marginally stable mean flow solution U^*, showing that the solution to the coupled system (3.12), $A^*, \omega_1^*, U^*, u_1^*$ is not path dependent.

3.5 Saturated flow

3.5.1 Mean flow and base flow

The converged mean flow $\boldsymbol{U}^*$ obtained from the self-consistent model predicts very accurately the DNS result showing the same recirculation bubble length with a similar wake distribution as presented in Fig. 3.5 for $Re = 60$ and $Re = 100$.
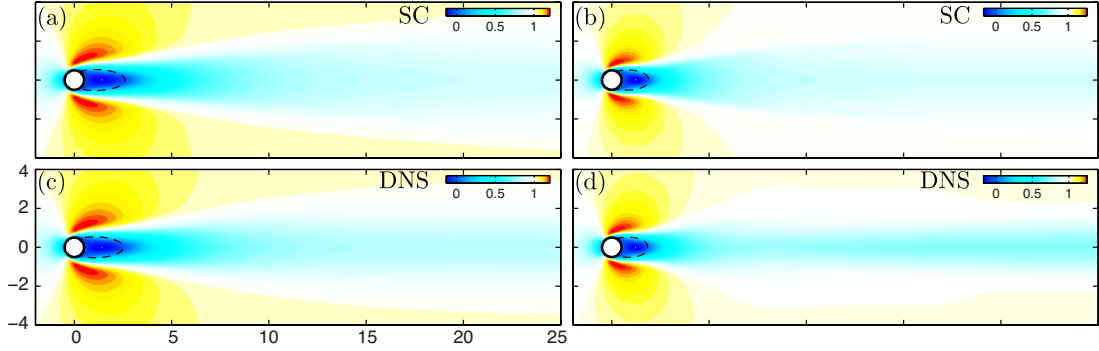
Figure 3.5 – $Re = 100$ and Re=60 Self-consistent (a,b) and DNS (c,d) comparison of the mean flow velocity $\boldsymbol{U}^*$ for the x-direction. For $Re = 60$ (a) self-consistent and (c) DNS. For $Re = 100$ (b) self-consistent and (d) DNS.

A more quantitative comparison to DNS results is presented in Fig. 3.6. The model provides an excellent prediction of the mean flow recirculation bubble for all Reynolds numbers (Fig. 3.6a), exhibiting a recirculation length L_x that is much shorter than in the wake of the base flow $\boldsymbol{U}_B$.

Fig. 3.6b shows the relative difference between the model's mean flow $\boldsymbol{U}^*$ and the 'exact' mean flow from DNS $\boldsymbol{U}_{DNS}$, as well as the corresponding difference associated with using the steady base flow $\boldsymbol{U}_B$ as approximation of the mean flow. The relative difference between a steady flow $\boldsymbol{U}$ (the base flow $\boldsymbol{U}_B$ or the model's mean flow $\boldsymbol{U}^*$) and the mean flow from DNS is defined as the norm of their difference normalized by the velocity deficit $\boldsymbol{U}_\delta \equiv \boldsymbol{U}_{DNS} - 1e_x$ of the DNS mean flow, i.e. Diff($\boldsymbol{U}$) = $\|\boldsymbol{U} - \boldsymbol{U}_{DNS}\| / \|\boldsymbol{U}_\delta\|$; this difference is independent of the domain size. As it can be seen in Fig. 3.6b, the relative difference of the model's mean flow $\boldsymbol{U}^*$ stays below 10%, while the difference of the base flow $\boldsymbol{U}_B$ increases up to 100%.

As can be seen from Fig. 3.5(b-d), the difference between $\boldsymbol{U}^*$ and $\boldsymbol{U}_{DNS}$ is in large part located far downstream, a region in which the flow dynamics consists mainly in the advection and diffusion of the shed vortices. In the case of the mean flow from DNS (Fig. 3.5(d)), the advected vortices lead to a relatively strong and concentrated velocity deficit in the wake as compared to the model's prediction (Fig. 3.5(b)), in which the velocity deficit seems blurred. As it will be seen below, this seemingly minor difference between the mean flows has important consequences for the respective leading eigenmodes and their associated Reynolds stress.
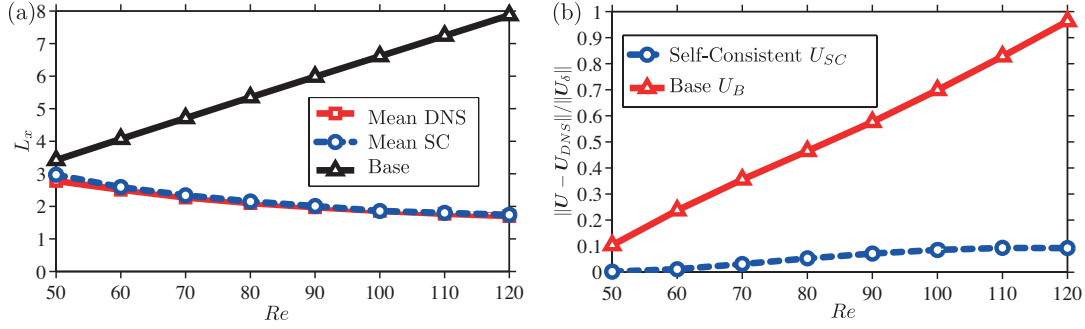
Figure 3.6 – (a) Base flow (triangles) and mean flow recirculation bubble length L_x variation with the Reynolds number Re for the self-consistent model (circles) and DNS (squares). (b) Relative difference of the self consistent model results $\boldsymbol{U}^*$ (circles) and the base flow $\boldsymbol{U}_B$ (triangles) compared to the exact DNS mean flow $\boldsymbol{U}_{DNS}$. The relative difference is defined as $\|\boldsymbol{U} - \boldsymbol{U}_{DNS}\| / \|\boldsymbol{U}_\delta\|$.

3.5.2 Fluctuation and perturbation

In the left of Fig. 3.7, the x-velocity component of the perturbation $\boldsymbol{u}_1'^*$ from the leading eigenmodes of the self-consistent model $\boldsymbol{u}_1^*$ (Fig. 3.7(a)) and the perturbation velocity $\boldsymbol{u}_{1DNS}'$ of the leading eigenmode $\boldsymbol{u}_{1DNS}$ around the DNS mean flow (Fig. 3.7(e)) are compared to a snapshot of the corresponding fluctuating velocity component of the fully nonlinear DNS $\boldsymbol{u}'$ (Fig. 3.7(c)). The least stable eigenmode $\boldsymbol{u}_1^*$ of the self-consistent model presents a wavelength of the vortex shedding that is very similar to that of the DNS snapshot $\boldsymbol{u}'$, as illustrated more quantitatively in Fig. 3.8a where the contrast with the wavelength of base flow eigenmode $\boldsymbol{u}_{1B}$ can be also appreciated. This resemblance is also well captured by the eigenmode $\boldsymbol{u}_{1DNS}$ of the exact DNS mean flow $\boldsymbol{U}_{DNS}$, shown in Fig. 3.7(e) and also Fig. 3.8a; this was highlighted by Barkley (2006) and also by Mittal (2008), who has mentioned the relationship of this streamwise wavelength to the (accurate) frequency prediction of the eigenmode of the mean flow.

Besides this similarity, there are important differences between the eigenmode of the self-consistent model $\boldsymbol{u}_1^*$ and that of the DNS mean flow $\boldsymbol{u}_{1DNS}$. The present model solution $\boldsymbol{u}_1^*$ captures also important features of the spatial distribution of the vortex shedding, since the amplitude of the corresponding streamwise oscillations peaks close to the cylinder and decreases quickly downstream, similar to the fully nonlinear snapshot (Fig. 3.7(c)). This trend is illustrated in more detail in Fig. 3.8b, which shows the energy distribution of the fluctuating velocity integrated in the y-direction, illustrating how far are the energy distribution of the base flow and mean flow eigenmodes from the exact DNS. For the eigenmode of the DNS mean flow $\boldsymbol{u}_{1DNS}$, the peak in amplitude of the streamwise oscillations is followed by a much weaker decay downstream, resulting in a flow structure that is much more elongated than the actual vortex shedding. In addition, the nodal lines of the model's eigenmode are mostly aligned to the y-direction in the downstream region (Fig. 3.7(a)), similar to the nonlinear fluctuations from DNS (Fig. 3.7(c)) and unlike the oblique structures of $\boldsymbol{u}_{1DNS}$ (Fig. 3.7(e)). These
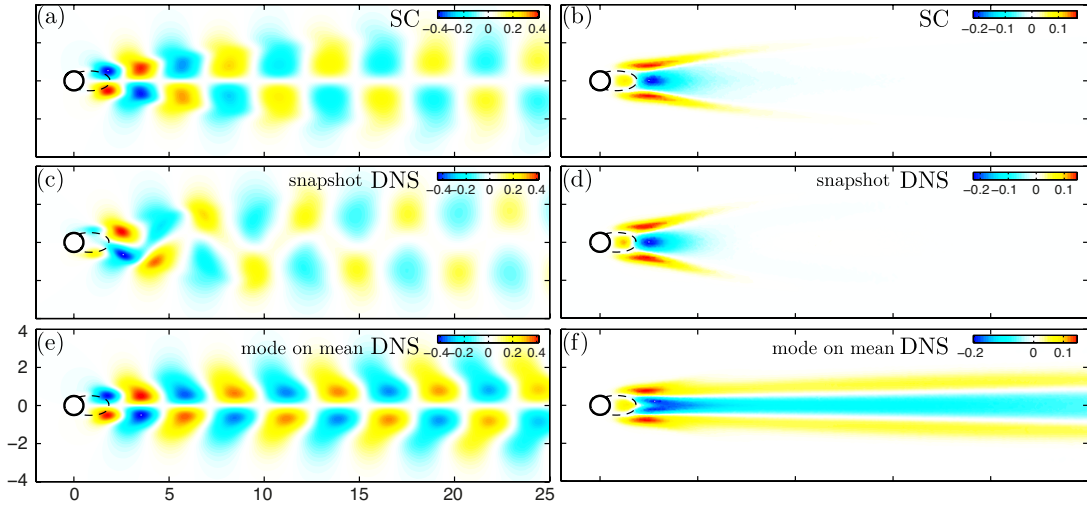
Figure 3.7 – $Re = 100$ Self-consistent and DNS comparison for the perturbation and fluctuation velocity (a,c,e) and Reynolds stress divergence (b,d,f) in the x-direction. (a) Perturbation velocity of the self consistent model calculated by the most unstable eigenmode $\boldsymbol{u}_1'^*$, (c) Snapshot of the DNS fluctuation velocity $\boldsymbol{u}'$ and (e) perturbation velocity $\boldsymbol{u}_{1DNS}'$ by the most unstable eigenmode of the DNS mean flow with the same amplitude as the DNS snapshot. (b) Reynolds stress divergence of the self-consistent model $2A^{*2}\Re\left((\bar{\boldsymbol{u}}_1^* \cdot \nabla)\boldsymbol{u}_1^*\right)$, (d) Reynolds stress divergence of the full nonlinear DNS $\langle(\boldsymbol{u}' \cdot \nabla)\boldsymbol{u}'\rangle$ and (f) Reynolds stress divergence build by the least stable eigenmode of the DNS mean flow $2\Re\left((\bar{\boldsymbol{u}}_{1DNS} \cdot \nabla)\boldsymbol{u}_{1DNS}\right)$ enforcing the amplitude to be the same as the DNS Reynolds stress.

two differences between $\boldsymbol{u}_1^*$ and $\boldsymbol{u}_{1DNS}$ can be directly traced to the previously mentioned difference between the model's ($\boldsymbol{U}^*$) and the DNS ($\boldsymbol{U}_{DNS}$) mean flows regarding the more concentrated velocity deficit of $\boldsymbol{U}_{DNS}$ in the region far downstream (Fig. 3.5(d)). The relatively strong shear associated to the more concentrated velocity deficit in the downstream region of $\boldsymbol{U}_{DNS}$ coincides with the larger amplitude of the streamwise oscillations as well as with the oblique structures of $\boldsymbol{u}_{1DNS}$, which are tilted against the shear of $\boldsymbol{U}_{DNS}$. This subtle failure of $\boldsymbol{U}^*$ in correctly approximating the mean flow from DNS appears as necessary for a better approximation of the vortex shedding structure with a single mode.

The comparison between the Reynolds stresses shown on the right of Fig. 3.7 is striking. The Reynolds stress divergence calculated from the leading eigenmode of the model (Fig. 3.7(b)) $2A^{*2}\Re\left((\bar{\boldsymbol{u}}_1^* \cdot \nabla)\boldsymbol{u}_1^*\right)$ is remarkably similar to that of the fully nonlinear time-averaged DNS $\langle(\boldsymbol{u}' \cdot \nabla)\boldsymbol{u}'\rangle$ (Fig. 3.7(d)). Both, the self-consistent and fully nonlinear DNS Reynolds stress present similar amplitude and spatial distribution concentrating the forcing close to the cylinder. On the contrary, the Reynolds stress based on the most unstable eigenmode $\boldsymbol{u}_{1DNS}$ around the time averaged DNS (Fig. 3.7(f)) presents an elongated structure with the forcing spread further downstream. The different spatial structures of the Reynolds stresses of the two eigenmodes (model and mean-flow) are a direct result of the different spatial structures of the respective modes described above (Figs. 3.7(a) and 3.7(e)). It should be noted that

45
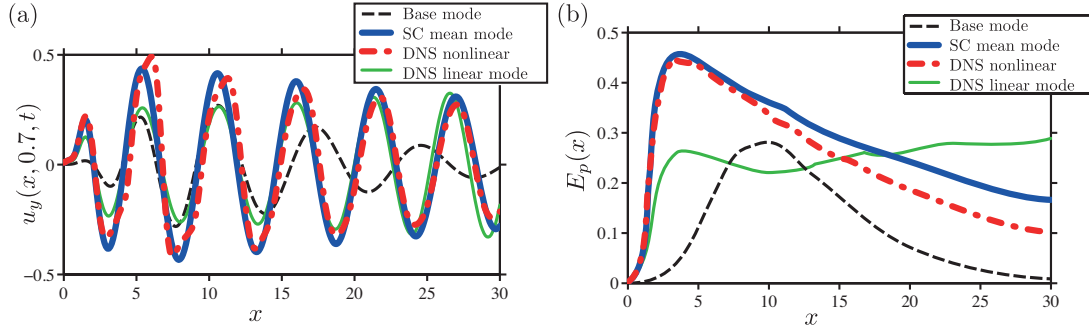
Figure 3.8 – $Re = 100$ (a) Stream-wise cut of the fluctuation velocity u'_y in the y-direction at $y = 0.7$ and (b) energy integral in y-direction averaged over one period, $E_p(x) = T^{-1} \int_0^T \int_{-\infty}^{\infty} u'^2(x, y, t)\,dy\,dt$. Base flow linear perturbation (dashed line), perturbation velocity of the self consistent model calculated by the most unstable eigenmode u'^*_1 (thick solid line), snapshot of the DNS fluctuation velocity u' (dashed-dotted line), and the velocity from the most unstable eigenmode of the DNS mean flow u_{1DNS} (thin solid line); the base flow and DNS mean flow eigenmode amplitudes are fixed to be the same as the DNS snapshot.

the shape of the Reynolds stress divergence completely determines the mean flow in the self-consistent model and in DNS, and unlike the linear solution around the DNS mean flow. This is because the self-consistent result U^*, u_1 comes as a closed system solution where the mean flow and perturbation interact between each other nonlinearly through the Reynolds stress (3.12) in a similar manner as in the full DNS, while the linear solution around the DNS is largely uncoupled (3.7).

Note that the full DNS Reynolds stress divergence is built by all the harmonics u' whereas in the self-consistent model it is constituted only by the neutrally stable eigenmode u^*_1 of the mean flow. Therefore, the amplitude of the higher harmonic contribution decreases more abruptly for the Reynolds stress forcing than for the fluctuation since they scale as $\langle (u' \cdot \nabla) u' \rangle \sim \mathcal{O}(u'^2)$. This scaling difference may explain why the Reynolds stress divergence of the model resembles better the exact DNS solution Fig. 3.7(b-d) than the fluctuating velocity Fig. 3.7(a-c).

Fig. 3.9a shows that the saturated frequency of the vortex shedding from experiments is well approximated by the model converged solution represented by squares in Fig. 3.9a, while at the same time, matching the eigenvalues of the linear stability around the DNS mean flow as previously described by Barkley (2006). The model is valid far from threshold, contrary to the perturbative theory (thin straight line) of the well known amplitude equation (Sipp & Lebedev (2007); Stuart (1960)), capturing the correct frequency shift from the initial base flow (solid line Fig. 3.9a).

The perturbation amplitude predicted by the self-consistent model (squares) follows closely the DNS results (circles), as seen in Fig. 3.9b, capturing well the nonlinear retroaction of the perturbation equation onto the mean flow. However, the model requires a slightly larger perturbation amplitude A^* in order to obtain a marginally stable mean flow. This probably
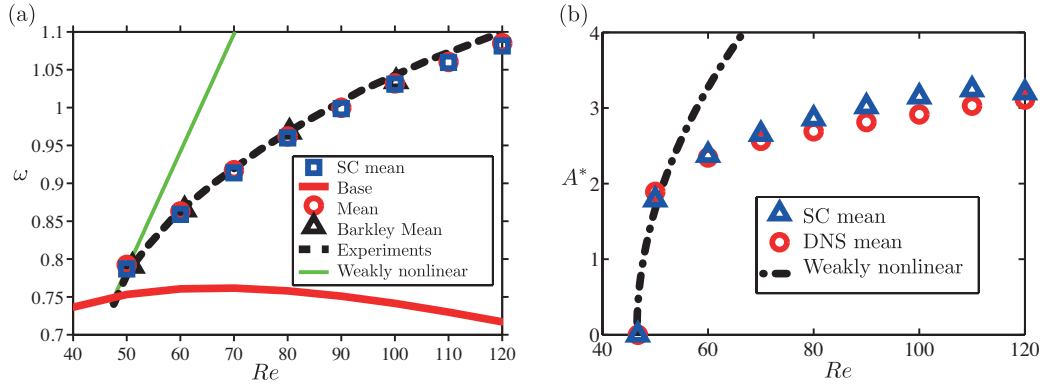
Figure 3.9 – (a) Frequency ω of the least stable eigenmode of the self-consistent model mean flow (squares), steady base flow (solid line) and DNS mean flow (circles) as compared to Barkley (2006) eigenvalues around the mean flow (triangles), experimental frequency (dash line) and the weakly nonlinear theory prediction (Sipp & Lebedev (2007); Stuart (1960)) (thin solid line). (b) Fluctuation and perturbation amplitude A^* variation with Reynolds number for the weakly nonlinear theory (dashed line), converged self-consistent model (squares) and saturated DNS (circles).

because the Reynolds stress forcing is only constructed by one harmonic which has to approximate the spatial information of all harmonics in DNS. The reduced amplitude at $Re = 120$ is related to the partial convergence. Note also how the weakly nonlinear theory is valid only close to the critical Reynolds number as it starts to diverge from DNS and self-consistent results for $Re > 50$, Fig. 3.9. This discrepancy of the weakly nonlinear theory is caused by the lack of coupling between the mean flow variation and the perturbation equation through the Reynolds stress which on the contrary is present in the self-consistent model.

3.5.3 Vorticity fields

In order to complement the description of the flow field behind the cylinder, the vorticity of the fluctuation is presented in Fig. 3.10. The self-consistent vorticity structure from the perturbation $\boldsymbol{u}_1'^*$ illustrated in Fig. 3.10(a) resembles well the fully nonlinear DNS fluctuation $\boldsymbol{u}'$ at the fundamental frequency (ω, Fig. 3.10(c)), showing a similar pattern of horizontally alternated positive and negative vortices with a reflection symmetry about $y = 0$. However, the self-consistent model misses the vertical alternation of vortices gathered in the second harmonic at (2ω, Fig. 3.10(d)) and thus explaining the difference with the total fluctuation snapshot depicted in Fig. 3.10(b). The vorticiy of the perturbation around the mean flow $\boldsymbol{u}_{1DNS}$ shows an even poorer approximation of the DNS snapshot presenting oblique structures in the same fashion as previously described in Fig. 3.7 and Fig. 3.8.

It seems that the loss of symmetry about $y = 0$ is secondary in the wake dynamics and in the saturation process since the self-consistent model is able to capture the correct shape of the
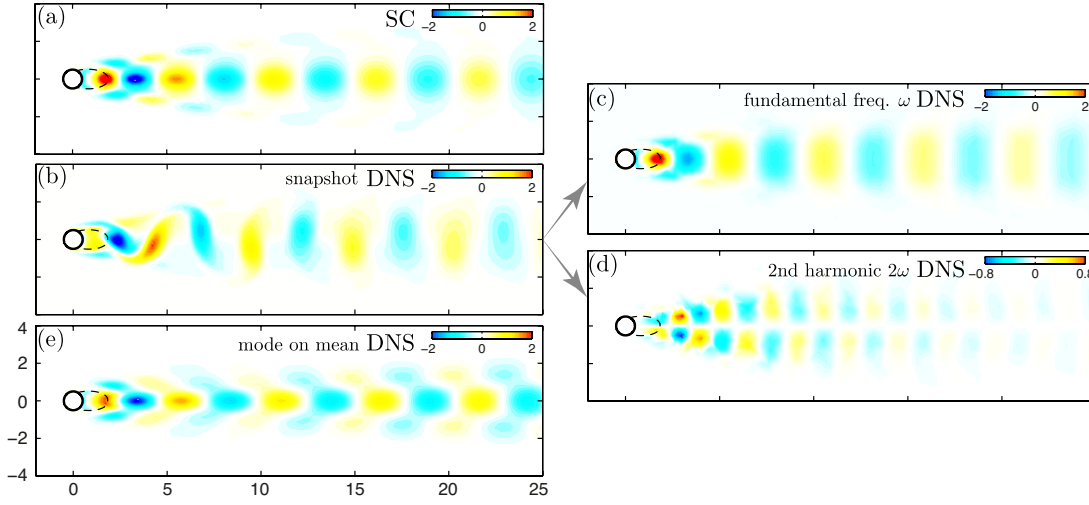
Figure 3.10 – $Re = 100$ Self-consistent and DNS comparison for the vorticity of the fluctuation. (a) Perturbation vorticity of the self consistent model calculated from the most unstable eigenmode $u_1'^*$. (b) Snapshot of the DNS fluctuation vorticity from u', (c) fluctuation vorticity of the fundamental and (d) vorticity distribution of the second harmonic, both extracted from the fully nonlinear DNS fluctuating field $u'(x, t)$ by Fourier series. (e) Perturbation vorticity from the most unstable eigenmode u_{1DNS} of the DNS mean flow with the same amplitude as the DNS snapshot.

Reynolds stress divergence (Fig. 3.7), the mean flow (Fig. 3.5-3.6) and the fluctuation energy distribution (Fig. 3.8(b)) with a symmetric vorticity distribution.

3.6 Transient evolution

The transient evolution of the 2D cylinder flow from the unstable base flow U_B to the marginally stable mean flow $U, \sigma_1 = 0$ is considered by splitting the effects between the fast time-scale of the fluctuation oscillation $u'(t)$ and the slow time evolution of the mean flow U. The evolution in time of the instantaneous mean flow is assessed by calculating the average among DNS with several initial conditions defined as the base flow U_B plus a small perturbation $A_0 u_{1\phi}$, of same amplitude A_0 and a structure of the most unstable eigenmode u_1 and different phase ϕ_0, which allows the selection of the wave phase of the initial perturbation as introduced in 3.2. The initial phase angle span $\phi_0 = [0, 2\pi]$ is divided in $n_\phi = 8$ equal parts providing an instantaneous mean flow approximation at each slow time step equivalent to an average over 8 snapshots of one period in the fast time scale. An average over $n_\phi = 8$ is deemed to be enough as $n_\phi = 4$ and $n_\phi = 8$ provided indistinguishable results.

The phase averaged mean flow evolves in time with an associated change of the fluctuation shape, frequency and amplitude. The saturation of the DNS fluctuation amplitude A_{DNS} (solid line) is presented in Fig. 3.1(h), being calculated from the norm of the instantaneous velocity minus the phase averaged mean, $u' = u - U_{DNS}(t)$. On the other hand, the results
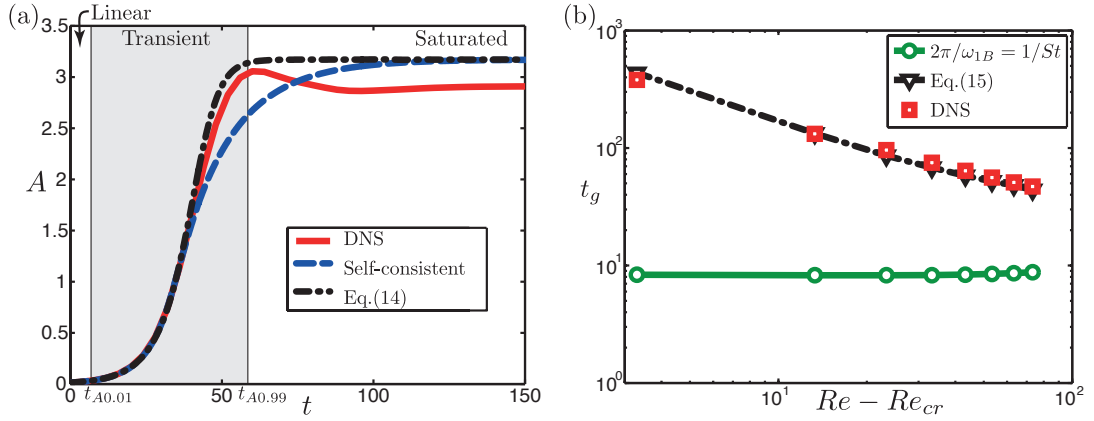
Figure 3.11 – (a) Time evolution of the fluctuation amplitude during the saturation process, DNS (solid line), self-consistent (dashed line) and simplified polynomial relation (3.14) of $\sigma_1(A)$ (dash dotted line) for $Re = 100$. (b) Time for the instability growth ($t_g = t_{A0.99} - t_{A0.01}$) (3.15) as function of the Reynolds number for the DNS (squares) and based on a polynomial approximation (3.14) of the $\sigma_1(A)$ relation (dash dotted line). Characteristic period of the base flow perturbation $1/St$ (circles).

$\boldsymbol{U}(A), \boldsymbol{u}'_1(A), \sigma_1(A), \omega_1(A)$ of the self-consistent model (3.10) for each amplitude A predict, through the evolution equation (3.11), an analogous slow time-scale dynamics which can be compared to the DNS exact transient. Then, knowing the relation $\sigma_1(A)$ from Fig. 3.3, (3.11) is integrated with a fourth order Runge-Kutta method and the corresponding small initial amplitude A_0. The amplitude $A(t)$ as a function of time for the self-consistent model is compared to DNS in Fig. 3.11(a) and in logarithmic scale in Fig. 3.1(h). The model shows a fair agreement with the transient dynamics of the DNS, closely matching the initial evolution up to roughly half the amplitude of saturation, while also capturing the final stage of saturation with the modest difference in final amplitude shown in Fig. 3.9b. There is an overshoot in the transient, also reported inTadmor *et al.* (2010), which the self-consistent model fails to reproduce probably because it is based on a quasi-static approximation.

Indeed at this Reynolds number there is no strict separation of time scales since the transient time based on the base flow growth rate is of similar order of magnitude as the fluctuation period $1/\sigma_{1B} \sim 1/St \sim 8$ for $Re = 100$. However, defining a time for the instability growth t_g as the time between the amplitude 1% and 99% of the saturated mean flow amplitude, the DNS results show that the frequency time scale $1/St$ is much smaller than t_g even for Reynolds numbers as large as $Re = 100$ (Fig. 3.11(b)). Hence, there is time for several oscillations during the growth of the instability, pointing to the relevance of the averaging process involved in the self-consistent model.

A step further in simplification of the transient dynamics is to approximate the function $\sigma_1(A)$ obtained from the self-consistent model in Fig. 3.3 with a simple polynomial of second order

consistent with the Stuart-Landau amplitude equation (Stuart (1960)),

$$\sigma_1(A) \sim \sigma_{1B}\left(1 - \frac{A^2}{A^{*2}}\right), \tag{3.14}$$

where σ_{1B} is the growth rate from the most unstable mode of the linear stability around the base flow, and A^* is the saturated amplitude. Integrating (3.11) from A_0 at $t = 0$ and assuming the polynomial relation (3.14) we obtain an analytical solution which is plotted in Fig. 3.11(a) showing a good approximation of the amplitude evolution when compared to DNS. The time of the transient evolution can be calculated from the relation (3.14) as

$$t_g = \frac{K}{\sigma_{1B}}, \tag{3.15}$$

where $K = \frac{1}{2}\log\left(\frac{0.99^2}{1-0.99^2}\frac{1-0.01^2}{0.01^2}\right)$. The transient time t_g obtained from the crude approximation (3.14) compares well to the DNS transient time as illustrated in Fig. 3.11(b). Thereby relation (3.15) allows to obtain an *a priori* approximation of the transient time t_g independent of the mean flow and just dependent on the base flow growth rate σ_{1B}.

During the transient, the base flow is modified slowly with the progressive saturation of the instability associated to the growth rate reduction with time. The instantaneous growth rate σ of the fluctuating instability $\boldsymbol{u}'$ around the instantaneous mean flow $\boldsymbol{U}_{DNS}(t)$ can be obtained from

$$\sigma(t) = \frac{d\log A_{DNS}(t)}{dt}, \tag{3.16}$$

where the fluctuation amplitude $A_{DNS}(t)$ of the DNS at each slow time step is extracted from Fig. 3.1(h). This nonlinear instantaneous growth rate σ (solid line) is compared in Fig. 3.12(a) to the linear growth rate σ_{1DNS} (circles and triangles) calculated from the linear stability analysis (3.7) around each instantaneous mean, showing a slightly delayed saturation of the linear growth rate but a similar overall evolution. The instantaneous growth rate of the self-consistent model obtained for its equivalent time (dashed line in Fig. 3.12(a)) follows however more closely the exact DNS transition, but misses the overshoot of the DNS before the saturated value.

On the other hand, the linear frequency of the DNS instantaneous mean (circles and triangles) matches better the exact DNS nonlinear frequency (solid line in Fig. 3.12(b)), which is extracted from the time evolution of the x-direction velocity at $(x, y) = (2, 1)$, as depicted in Fig. 3.1(g), when compared to the predicted frequency of the self-consistent model (dashed line) at the equivalent time. A similar remarkable agreement was found already by Thiria *et al.* (2015) using a weakly non parallel stability analysis. We think that this minimal difference might appear because the self-consistent model transient evolution and the DNS correspond to independent dynamical systems. In both cases the growth rate σ and amplitude A are the leading parameters to capture the nonlinear saturation from the base flow $\boldsymbol{U}_B$ to the marginally stable mean flow $\boldsymbol{U}^*$, while the frequency is free to vary.
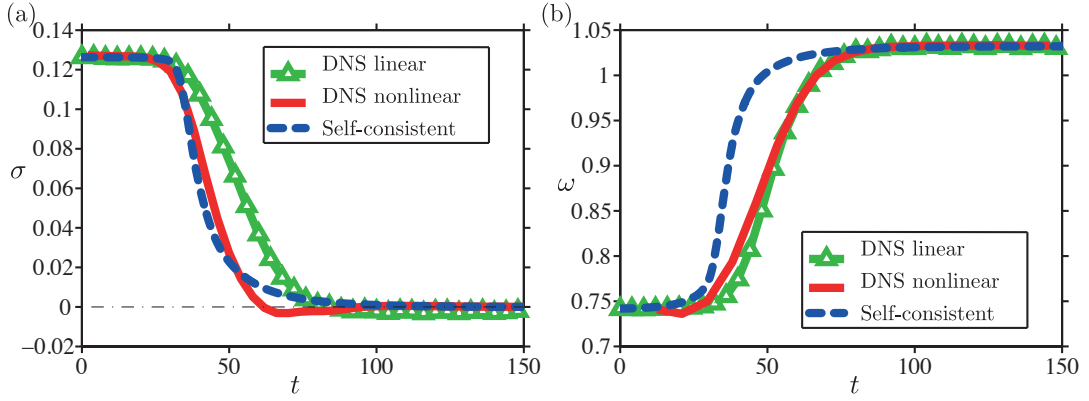
Figure 3.12 – Evolution of the transient growth rate (a) and frequency (b) with time. Comparison between the linear stability prediction around the instantaneous DNS mean (triangles, labeled as linear), the fully nonlinear instantaneous growth rate and frequency of the DNS fluctuation evolution $\boldsymbol{u}'$ (solid line labeled as nonlinear DNS) and Self-consistent approximation of the frequency and growth rate (dashed line) at $Re = 100$.

The Reynolds stress divergence evolution of the DNS and the self-consistent model is compared in Fig. 3.13 for three different linear growth rates $\sigma_1 = 1.27, 0.66, 0$ at their associated times $t_{SC} = 0, 40, 150$ and $t_{DNS} = 0, 50, 150$. Since the same linear growth rate is obtained at different equivalent times, the self-consistent model and the full DNS nonlinear saturation do not follow exactly the same dynamical paths. However, the close matching encountered in the evolution of the spatial structure (Fig. 3.13) suggests a physical relation underlying the Reynolds stress amplitude convergence of the self-consistent model A_f and the transient DNS evolution in the slow time scale. The quasi-steady evolution of the perturbation based on the growth-rate of the unstable eigenmode which is coupled back to the mean flow through the Reynolds stress is enough to capture the slow time evolution of the fully nonlinear DNS saturation. Independently of the exact path of the instantaneous mean flow, the growth rate decreases accompanied by a frequency increase as oscillations grow and saturate.

3.7 Conclusions

We have presented and characterized the self-consistent model (3.12) that describes the saturation process of the vortex shedding instability by coupling the mean flow and the linear perturbation equation. The model provides an excellent prediction of the mean flow and its associated vortex street in terms of frequency, amplitude and spatial structure. This fully nonlinear fluctuating field is approximated by a single harmonic given by the most unstable eigenmode around the mean, which at the same time creates the Reynolds stress that forces back onto the aforementioned mean flow closing the system. The obtained Reynolds stress divergence of the coupled model estimates very well the structure of the exact solution of the full DNS, unlike the one constructed by the most unstable eigenmode of the DNS mean flow since it is largely decoupled. From the vorticity fields it can be inferred that the vertical
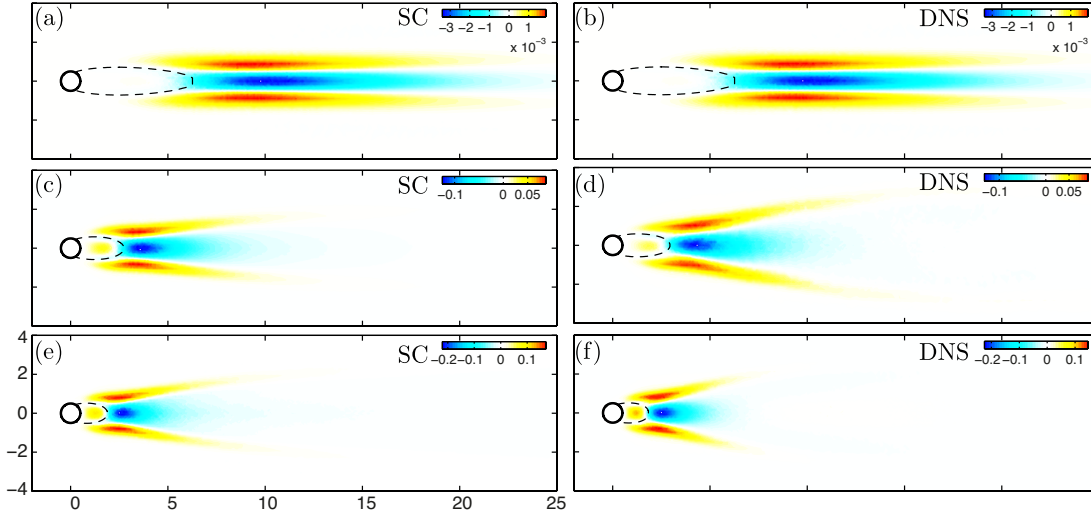
Figure 3.13 – Reynolds stress divergence in x-direction component; (a,c,e) for the Self-consistent model $2A^2\Re\left((\bar{\boldsymbol{u}}_1 \cdot \nabla)\boldsymbol{u}_1\right)$ and (b,d,f) for the full DNS $\langle(\boldsymbol{u}' \cdot \nabla)\boldsymbol{u}'\rangle$, comparison of the transient evolution for $\sigma_1 = 1.27$ (a) self-consistent and (b) DNS, for $\sigma_1 = 0.66$ (c) self-consistent and (d) DNS and for $\sigma_1 = 0$ (e) self-consistent and (f) DNS at $Re = 100$.

alternation of the wake vortices is gathered in the second harmonic and thus missing in the symmetric wake of the model. Therefore, it seems to be a secondary effect not required to capture the saturation process.

In addition to the saturated periodic flow, we have extended the model to describe the transient of the saturation process from the unstable base flow to the marginally stable mean flow. The comparison reveals that the self-consistent model provides the same trends of the instantaneous mean flow as the fully nonlinear DNS obtained by averaging on the phase. The similarities in the evolution of the growth rate, frequency, fluctuation amplitude and Reynolds stress strongly suggest a physical relation between the perturbation amplitude A of the quasi-steady solution of the model and the time evolution of the DNS nonlinear saturation. The model shows that even with a single harmonic linear perturbation the flow evolves to similar saturation structures as the full DNS thanks to the retained Reynolds stress nonlinearity. Furthermore, assuming a simple relation between the growth rate and the fluctuation amplitude, we found a simple and predictive estimate of the characteristic time of the transient that compares well to the exact DNS.

Inspired by the scale separation of the weakly nonlinear theory (Sipp & Lebedev (2007)) the present model formalizes in a self-consistent coupled system the physical picture of an instability saturation process. The perturbation, given by the most unstable eigenmode, grows around the mean flow and modifies it by the Reynolds stress forcing, saturating at the point when the mean flow is marginally stable. This physical picture, which has been put forward in the past by various authors (Maurel *et al.* (1995); Stuart (1958); Barkley (2006)), is mathematically formalized by the present model. The similarities between DNS and the

predictions of the model strongly support the relevance of this saturation mechanism. The predictive capacity of the present model is in no way expected to make it significant as a substitute for the Navier-Stokes equations, rather, it is significant since it shows that this simplified model contains all the essential ingredients to provide a fairly accurate description of the physics. This substantiates the importance of the model.

As already mentioned, the idea of marginal stability of the mean flow was suggested in the 50's by Malkus (1956) for turbulent flows, and by Stuart (1958) for the saturation of supercritical instabilities. The dynamical significance of the mean flow was further suggested by accurate frequency predictions from the stability of mean flows for the vortex shedding instability (Triantafyllou *et al.* (1986); Barkley (2006); Hammond & Redekopp (1997); Pier (2002); Mittal (2008)), making it the obvious test case for our model. But these are also interesting questions for other limit cycles arising from oscillatory instabilities. Recently, the questions of the mean-flow's marginal stability and of frequency prediction from the mean flow have been considered by Turton *et al.* (2015) in a very different case, namely, thermosolutal convection driven by opposing thermal and solutal gradients. Turton *et al.* (2015) study two different types of limit cycles existing in such system, travelling and standing waves. Remarkably, they find that for travelling wave solutions the mean flow (or mean fields in this case involving two extra scalar fields) is nearly marginally stable and the frequency of its leading eigenmode almost matches that of the limit cycle. For the standing wave solutions, on the contrary, the frequency predicted by the mean flow's leading eigenvalue differs considerably from that of the limit cycle, and the mean flow is unstable, which is perhaps not surprising since the standing wave solution is also unstable. More importantly, they show that the key difference between travelling and standing wave solutions lies in their temporal spectra, strongly peaked for travelling waves but not so for standing waves. Moreover, they provide a general discussion for systems with limit cycles and quadratic nonlinearities, and show that when the limit cycle has (almost) a single temporal frequency, the leading eigenvalue of the mean flow necessarily has (almost) the right frequency with (almost) zero growth rate. This points to a broader applicability of our model, although their attempt to implement it based on our previous report (Mantič-Lugo *et al.* (2014)) did not converge (Turton *et al.* (2015)).

In any case, the relevance of this type of self-consistent quasilinear models, which couple a perturbation equation linearized around a mean flow which is itself determined simultaneously from the Reynolds stress of the perturbations, goes well beyond limit cycles. A recent study derives a similar model in order to compute exact coherent structures in the transitional regime of a parallel shear flow (Beaume *et al.* (2015)). Another important application of such models involves the study of turbulent flows by modeling the nonlinear effects of turbulent fluctuations as a stochastic forcing on the linearized fluctuation equations. This has been used, for example, for obtaining statistical solutions leading to analytical expressions of the mean flow for wall bounded turbulence (Nazarenko *et al.* (2000)), or for describing the appearance of coherent structures as a bifurcation of the statistical solution(Farrell & Ioannou (2012); Bouchet *et al.* (2013)). Further development of these ideas may open interesting possibilities for optimization and flow control.

4 Saturation mechanism of the response to harmonic forcing

The nonlinear dynamics of oscillators has been analysed in the two previous chapters by introducing a semi-linear model to describe its saturation. Although amplifiers are linearly stable and therefore do not present intrinsic dynamics, they exhibit very large amplifications to external perturbations, or noise, which irremediably trigger a saturation mechanism that restricts the amplitude of the response to forcing. The purpose of this chapter is to answer the question if the self-consistent semi-linear model successfully applied to the cylinder wake flow can also elucidate the saturation of harmonically forced stable amplifier flow, like the backward-facing step flow.

Paper: *Self-consistent model for the saturation mechanism of the response to harmonic forcing in the backward-facing step flow*

Self-consistent model for the saturation mechanism of the response to harmonic forcing in the backward-facing step flow

Vladislav Mantič-Lugo[1] and François Gallaire[1]

1) LFMI, École Polytechnique Fédérale de Lausanne, CH-1015 Lausanne, Switzerland

Certain flows denominated as amplifiers are characterised by their global linear stability while showing large linear amplifications to sustained perturbations. As the forcing amplitude increases, a strong saturation of the response appears when compared to the linear prediction. However, a predictive model describing the saturation of the response to higher amplitudes of the sustained forcing is still missing. An asymptotic analysis based on the weakly nonlinear theory is first proposed showing how the saturation process is governed by the Reynolds stress nonlinear interaction, thus motivating the introduction of a simple self-consistent model.

The model consists of a decomposition of the full nonlinear Navier-Stokes equations in a mean flow equation together with a linear perturbation equation around the mean flow, which are coupled through the Reynolds stress. The full fluctuating response and the resulting Reynolds stress are approximated by the first harmonic calculated from the linear response to the forcing around the aforementioned mean flow. This closed set of coupled equations is solved in an iterative manner as partial nonlinearity is still preserved in the mean flow equation despite the assumed simplifications.

The results show an accurate prediction of the response energy when compared to Direct Numerical Simulations (DNS). The approximated coupling is strong enough to retain the main nonlinear effects of the saturation process. Hence, a simple physical picture is formalised, wherein the response modifies the mean flow through the Reynolds stress in such a way that the correct response energy is attained.

Keywords: Shear layers, Nonlinear instability, Separated flows

4.1   Introduction

Over the years linear stability theory has been the most classical approach applied to understand and describe bifurcations, instability and eventually transition to turbulence in fluid dynamics (Schmid & Henningson (2001)). It predicts the asymptotic long term response to small initial perturbations and yields a successful estimation of the critical control parameter where the first bifurcation occurs in many flows (Drazin & Reid (2004)), e.g. Rayleigh-Benard convection, Taylor-Couette flow between rotating cylinders, or the flow past a cylinder. Nonetheless,

some flows exhibit bifurcations well below the critical Reynolds number Re_{cr} predicted by the linear stability analysis: parallel flows e.g. Couette and Hagen-Poiseuille (Schmid & Henningson (2001)), as well as non-parallel configurations like jets (Garnaud *et al.* (2013)) or the flow above a backward-facing step (Barkley *et al.* (2002)), among many others.

In the famous Reynolds pipe flow experiment (1883) and other examples, the critical Reynolds number of the bifurcation and eventual transition to turbulence is strongly dependent on the level of external noise. This dependency is interpreted by the non-normality of the Navier-Stokes system of equations, which is thus able to amplify perturbations by means of non-modal mechanisms (Trefethen *et al.* (1993), Chomaz (2005), Schmid (2007)). The nonnormality allows the flow to escape from linearly stable solutions by means of large temporal amplification of initial conditions (transient growth) as well as strong response to harmonic forcing, characterized by large gains.

A substantial body of work has therefore been devoted to the understanding of subcritical flows. While modal analysis focusing primarily on eigenvalues cannot predict the bifurcation threshold, other non-modal techniques stemming from classical linear algebra have shed light on the strong amplification potential of linearly stable flows. These techniques allow to find the optimal perturbations that enforce the largest possible amplification, in other words, the specific perturbation distribution resulting in the maximal transient growth or harmonic gain. Calculations on transient growth in parallel flows have been performed among others by Butler & Farrell (1992), Corbett & Bottaro (2000) and Schmid (2007) and in nonparallel 2D flows by Akervik *et al.* (2008) or Monokrousos *et al.* (2010); Sipp & Marquet (2012); Alizard *et al.* (2009) for spatially developing boundary layers and Blackburn *et al.* (2008) for the backward-facing step among others. Optimal harmonic forcing structures that produce the largest amplifications in response (Farrell & Ioannou (1996), Schmid (2007)) have been for instance studied in parallel plane Couette applying wave number expansion by Jovanović & Bamieh (2005). For several spatially developing open flows Akervik *et al.* (2008); Alizard *et al.* (2009); Sipp & Marquet (2012) have determined the optimal harmonic gain curves, which systematically displayed a preferred frequency. The harmonic response of the shear layer shed by the corner of the 2D backward facing step was then determined by Marquet & Sipp (2010) and later by Boujo & Gallaire (2015) among others.

A related but different approach is the study of the response to white noise, as was introduced for parallel flows by Farrell & Ioannou (1993). For non-parallel flows Dergham *et al.* (2013) present a low dimensional model to approximate the linear response of white noise for the 2D backward-facing step, while Boujo & Gallaire (2015) study the sensitivity and control of the response amplification under stochastic forcing. Whilst most of the non-modal studies presented rely on the linearisation around the stable steady solution of the NSE (Navier-Stokes equations), defined as base flow, an attempt to describe more precisely the actual physics involved in the strong noise amplification exhibited in turbulent jets has been pursued by Garnaud *et al.* (2013), who applied the optimal gain analysis on a model mean flow for globally stable jets.

All these studies rely on the linear response to perturbations, either intrinsic (instability) or externally driven (forcing) and are not able to describe saturation processes or the nonlinear interaction existing between the mean flow and fluctuating coherent structures, thus driving the need of characterizing the nonlinear effects involved. A well known description of the physical mechanism that takes place in the saturation of a supercritical instability close to threshold is presented by the Stuart-Landau amplitude equation introduced back in the 60's (Stuart (1960)). It comes as a result of an earlier Stuart's attempt (Stuart (1958)) to capture the saturation mechanism introducing the mean flow modification through the Reynolds stress constructed by the most unstable eigenmode. In a similar nonlinear spirit, Farrell and Ioannou propose the SSST theory (Farrell & Ioannou (2003)). It consists in writing the linear response to white noise forcing as a Lyapunov equation, and coupling it to the ensemble average mean flow by means of the Reynolds stress. The theory is able to describe the appearance of large coherent fluctuating structures in turbulent atmospheric flows (Farrell & Ioannou (2003)), as well as in the 3D Couette flow (Farrell & Ioannou (2012)), all of them being linearly stable.

Motivated by the work of Farrell and Ioannou and the weakly nonlinear theory used in the amplitude equation, we propose herein a model that captures the saturation of the response at increasingly higher amplitudes of sustained harmonic forcing. The model is specifically applied to the well known backward-facing step case study in 2D since it is globally stable at $Re = 500$ presenting the threshold for 3D global instability at $Re_{cr} \sim 748$ (Barkley *et al.* (2002) and Lanzerstorfer & Kuhlmann (2012)). First, an asymptotic expansion based on the weakly nonlinear theory is applied around the stable base flow, showing the Reynolds stress as the key nonlinear term in the saturation process, at least close to the threshold. Then, the asymptotic results serve as a base to propose a model where the mean flow is coupled with the linear response to harmonic forcing by means of the Reynolds stress, neglecting higher harmonics generation. The results present an accurate prediction of the saturation as much as of the structure of the response and mean flow. The introduced model relates to the model recently proposed by Mantič-Lugo *et al.* (2014), formalizing the importance of the Reynolds stress in the saturation process of unstable supercritical flows, as already discussed by Barkley (2006), Mittal (2008) and Turton *et al.* (2015) among others.

The paper is organized as follows. In section 5.2 the flow configuration is described and the numerical method is explained. Secion 4.3 presents the classical linear response calculation and reveals the difference with the exact DNS. Section 4.4 introduces the weakly nonlinear theory with the asymptotic method around the base flow that motivates the self-consistent model described in section 4.5. Finally the results of the model are compared to the exact DNS in section 4.6 and the conclusions are summarized in section 4.7.
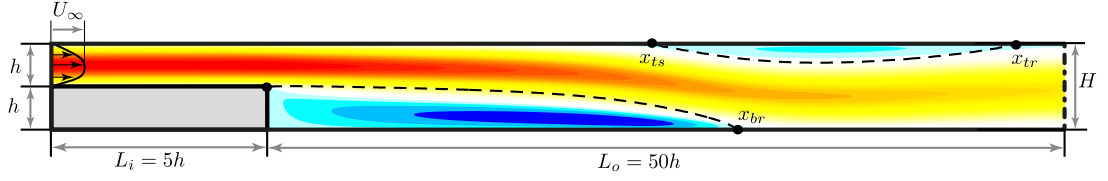
Figure 4.1 – Sketch of the flow configuration superimposed onto the velocity field x-direction of the base flow for the backward facing step at $Re = 500$.

4.2 Problem formulation

4.2.1 Flow geometry and governing equations

The case study selected is the 2D incompressible laminar flow around the backward facing step. The configuration is sketched in Fig. 4.1. It consists of an inlet channel of height h and length $L_i = 5h$ followed by a step of height h entailing a sudden expansion of height H where $H = 2h$ hence the expansion ration is $\Gamma = h/H = 0.5$ as depicted in Fig. 4.1. The Reynolds number is defined as $Re = hU_\infty/\nu$, where h is the inlet channel height, U_∞ the centerline (maximum) velocity of the plane Poiseuille inlet boundary condition and ν the kinematic viscosity. The non-dimensional frequency defined by the Strouhal number is given by $St = fh/(U_\infty) = \omega/(2\pi)$. Throughout the article, all the variables are non-dimensional using length h, density ρ_∞ and velocity U_∞ as reference scales.

The flow is governed by the forced 2D incompressible Navier-Stokes equations (NSE),

$$\partial_t \boldsymbol{u} + \mathcal{N}(\boldsymbol{u}) = \boldsymbol{f}, \tag{4.1}$$

where

$$\mathcal{N}(\boldsymbol{u}) \equiv (\boldsymbol{u} \cdot \nabla)\boldsymbol{u} + \nabla p - Re^{-1}\Delta \boldsymbol{u} \tag{4.2}$$

corresponds to the advective, pressure gradient and diffusive terms. The pressure field p is such that the velocity fields are divergence free $\nabla \cdot \boldsymbol{u} = 0$ following the incompressibility condition. The term $\boldsymbol{f}$ represents a harmonic body forcing of the form $\boldsymbol{f}(x,t) = \boldsymbol{f}_1(x)e^{i\omega t} + cc.$ with a given fixed frequency $St = \omega/(2\pi)$.

4.2.2 Linear transfer function

The steady solution of NSE

$$\mathcal{N}(\boldsymbol{U}_B) = 0, \tag{4.3}$$

is called the base flow $\boldsymbol{U}_B$ and it is linearly stable for the 2D backward-facing step with expansion ratio $\Gamma = 0.5$ at $Re = 500$ with its first unstable mode appearing in 3D for $Re_{cr} \sim 748$

59

(Barkley *et al.* (2002) and Lanzerstorfer & Kuhlmann (2012)). The classical approach is to study the linear response to harmonic forcing around this stable base flow. Fig. 4.1 shows the outline of the base flow of the backward-facing step at $Re = 500$.

The exact nonlinear response can be approximated by the linear response, assuming a small amplitude of the harmonic forcing,

$$[\partial_t \boldsymbol{u}'_{1B} + \mathscr{L}_{\boldsymbol{U}_B}(\boldsymbol{u}'_{1B})] = \boldsymbol{f}, \tag{4.4}$$

where higher order nonlinear terms are neglected as a first approximation, and the operator $\mathscr{L}_{\boldsymbol{U}}(\boldsymbol{u}')$ is the corresponding operator for the NSE linearized around $\boldsymbol{U}$, i.e.

$$\mathscr{L}_{\boldsymbol{U}}(\boldsymbol{u}') \equiv (\boldsymbol{U} \cdot \nabla)\boldsymbol{u}' + (\boldsymbol{u}' \cdot \nabla)\boldsymbol{U} + \nabla p' - Re^{-1}\Delta \boldsymbol{u}'. \tag{4.5}$$

Furthermore, since the forcing is harmonic, the corresponding response $\boldsymbol{u}'(x, t)$ will also be harmonic $\boldsymbol{u}'(x, t) \simeq \boldsymbol{u}'_{1B}(x, t) = \boldsymbol{u}_{1B}(x)e^{i\omega t} + cc.$ and oscillate purely at the forcing frequency, due to the linearity and stability of the operator (4.4).

The linear equation (4.4) can be rewritten formally as $\boldsymbol{u}_{1B} = \mathscr{R}(\omega)\boldsymbol{f}_1$ where $\mathscr{R}(\omega) = (i\omega + \mathscr{L}_{\boldsymbol{U}})^{-1}$ is the resolvent operator. The amplitude of the response in general can be measured as the square root of the kinetic energy of the purely time dependent fluctuation averaged over one period T,

$$B = \sqrt{\frac{1}{T}\int_0^T \int_\Omega \boldsymbol{u}'^2 d\Omega dt}. \tag{4.6}$$

Consequently, the amplitude of the linear response $\boldsymbol{u}'_{1B}$ corresponds to the L^2 norm

$$B = \sqrt{\frac{1}{T}\int_0^T \int_\Omega \boldsymbol{u}'^2_{1B} d\Omega dt} = \sqrt{2}\|\boldsymbol{u}_{1B}\| \tag{4.7}$$

as it is sinusoidal, defining the L^2 norm as determined by the Hermitian inner product $(\boldsymbol{a}|\boldsymbol{b}) = \int_\Omega \overline{\boldsymbol{a}} \cdot \boldsymbol{b} d\Omega = \int_\Omega \boldsymbol{a}^H \cdot \boldsymbol{b} d\Omega$, for complex fields in the domain Ω. In the same fashion, the forcing amplitude is calculated as the L^2 norm of the harmonic forcing

$$A = \sqrt{\frac{1}{T}\int_0^T \int_\Omega \boldsymbol{f}^2 d\Omega dt} = \sqrt{2}\|\boldsymbol{f}_1\|. \tag{4.8}$$

A natural way of measuring the amplification is the gain,

$$G(\omega) = B/A, \tag{4.9}$$

which is defined as the ratio between the amplitude of the response and the amplitude of the

input. Subsequently, for the linear case of harmonic forcing it reads

$$G(\omega) = \|\boldsymbol{u}_{1B}\| / \|\boldsymbol{f}_1\|. \tag{4.10}$$

In particular, it is relevant to determine the largest energy amplification possible at a given frequency or optimal gain $G_{opt}(\omega)$ which is associated to the optimal forcing $\boldsymbol{f}_{opt}$.

$$G_{opt}(\omega) = \max_{\boldsymbol{f}_1} \frac{\|\boldsymbol{u}_{1B}\|}{\|\boldsymbol{f}_1\|} = \frac{\|\mathscr{R}(\omega)\boldsymbol{f}_{opt}\|}{\|\boldsymbol{f}_{opt}\|}. \tag{4.11}$$

Introducing the adjoint of the resolvent operator, the gain can be rewritten as a Rayleigh quotient of the resolvent operator and the forcing,

$$G^2(\omega) = \frac{(\mathscr{R}\boldsymbol{f}_1 | \mathscr{R}\boldsymbol{f}_1)}{(\boldsymbol{f}_1 | \boldsymbol{f}_1)} = \frac{(\mathscr{R}^H \mathscr{R}\boldsymbol{f}_1 | \boldsymbol{f}_1)}{(\boldsymbol{f}_1 | \boldsymbol{f}_1)}. \tag{4.12}$$

Subsequently, the optimal gain and forcing correspond to the leading eigenvalue $\lambda_1 = G_1^2$ and eigenvector $\hat{f}_1$ of the symmetrical eigenvalue problem $\mathscr{R}^H \mathscr{R}\hat{f}_k = \lambda_k \hat{f}_k$. The undertaken procedure to obtain the optimal gain is described in more details in Garnaud *et al.* (2013) and Boujo & Gallaire (2015). Thus, we obtain for each forcing frequency an optimal forcing spatial distribution with its associated gain. A comparison of the optimal gains at different frequencies enables to obtain the overall optimal gain G_{opt} with its corresponding forcing $\boldsymbol{f}_{opt}$. Notice that this optimization is achieved only for the linear equation, and not for the full nonlinear gain of the DNS.

4.2.3 Numerical methods

The linear and nonlinear Navier-Stokes equations are solved applying the Finite Element Method representing the spatial discretization of the flow fields (u_x, u_y, p) by Taylor-Hood (P2,P2,P1) elements. The software FreeFEM++ is used to generate the domain Ω triangulation and to build all the required operators. The linear operators are solved by a Sparse solver implemented directly in FreeFEM++ while the singular value decomposition is solved in Matlab. The nonlinear systems as the steady state solutions are solved by the iterative Newton–Raphson method. The time integration of the DNS (Direct Numerical Simulation) of NSE is calculated applying a time scheme based on Characteristics-Galerkin method as described in Benitez & Bermudez (2011).

The computational domain under consideration is defined in Cartesian coordinates with the origin at the step edge. The nominal domain spans from $x = -5h$ to $x = 50h$ with an inlet $y = (0, h)$ and an outlet $y = (-h, h)$ as depicted in Fig. 4.1 being the same size as in Boujo & Gallaire (2015). A 2D plane Poiseuille profile is imposed as the inlet Dirichlet boundary condition $x_i = -h$. No-slip conditions are imposed at the upper $y = h$ and lower boundary $y = -h$ and outflow boundary condition is imposed at the outlet $x_o = 50h$.

	Mesh	L_i	x_{br}	x_{ts}	x_{tr}
Barkley *et al.* (2002)	-	1	10.87	8.71	17.49
	M2	1	10.9	8.7	17.5
present	**M1**	**5**	**10.8**	**8.6**	**17.4**
	M3	10	10.8	8.6	17.4

Table 4.1 – Comparison of the recirculation bubble position for different domain geometry, variation of inlet length L_i.

Mesh	L_i	L_o	G_{opt}	Difference %	Mesh	L_i	L_o	G_{opt}	Difference %
M4	5	40	7089	5%	M2	1	50	7030	6%
M1	**5**	**50**	**7453**	-	M1	**5**	**50**	**7453**	-
M5	5	60	7464	0.1%	M3	10	50	7493	0.5%

Table 4.2 – Comparison of the linear optimal gain at $St = 0.075$ for different domain geometry.

The size of the domain was chosen after thorough validation. The length of the domain is selected such that the base flow outlet profile reaches the fully developed Poiseuille profile, presenting an relative error between the base flow and the parabolic profile of less than 1% in L^2 and L_∞ norm. The influence of the entrance length on the recirculation bubble is summarized in Tab. 4.1 and compared to Barkley *et al.* (2002), to ensure that the chosen length is large enough and the solutions obtained are general and independent of further increase in domain size. In addition, the length of the recirculation bubble shows an excellent match for the whole range of Reynolds number compared to Barkley *et al.* (2002) and Blackburn *et al.* (2008).

The nominal domain and mesh M1 is of 33814 cells and 155691 DoF (degrees of freedom) obtaining a gain of 7453, which compares quantitatively well to the optimal $G_{opt} = 7480$ computed by Marquet & Sipp (2010) ensuring the quality of the methodology and mesh used. Furthermore, mesh independence is verified by doubling the number of cells by a uniform refinement obtaining M6 with 338247 DoF and 73982 cells, which provides a gain of 7456, thus a relative variation of less than 0.05%.

First and second order methods (Benitez & Bermudez (2011)) are compared for the time integration scheme of the DNS in Tab. 4.3. The second order method is chosen as it presents a much more robust results in terms of gain when compared to the first order in spite of a small increase in the computational time. The DNS time step is chosen by achieving time step independent results in terms of nonlinear gain as sumarized in Tab. 4.3. The selected time step $\delta t = 0.02$ is deemed to be small enough as a trade off between accuracy and computational time since it is located in the time step independent region.

Order	$\delta t = 0.005$	$\delta \mathbf{t} = \mathbf{0.02}$	$\delta t = 0.04$	$\delta t = 0.05$	$\delta t = 0.1$
Gain 1st Order	1622	1563	1492	1456	1276
Gain 2nd Order	1643	**1642**	1653	1663	-

Table 4.3 – Nonlinear saturated gain G of the DNS for different time step δt. The nonlinear solution is forced by the optimal harmonic forcing of amplitude $A = 4 \cdot 10^{-4}$ for $Re = 500$. The selected time scheme is second order and the time step is $\delta t = 0.02$ marked in black.
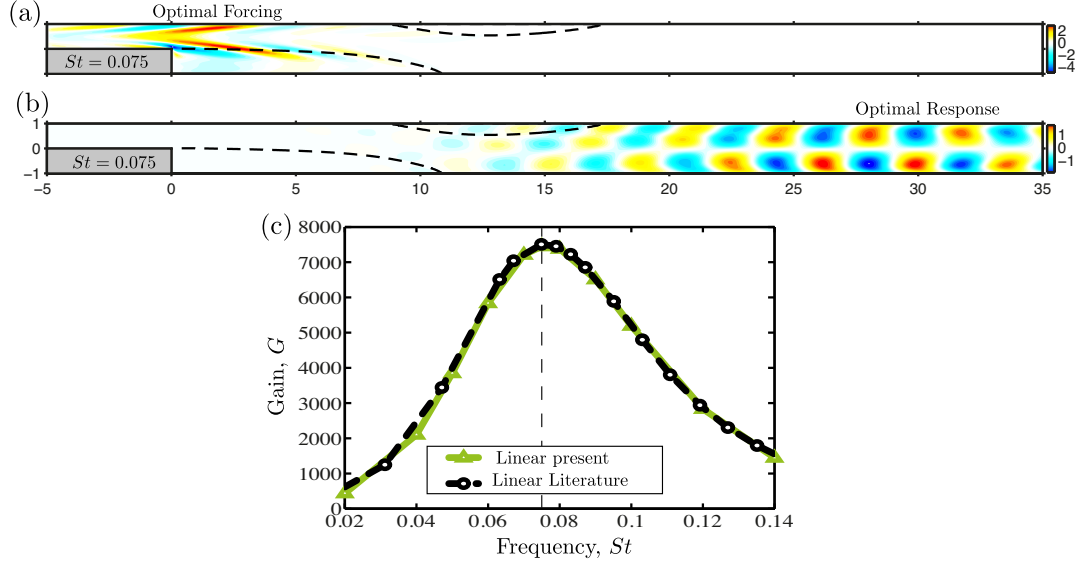
Figure 4.2 – (a) Linear optimal forcing in the x-direction and (b) linear optimal response in the x-direction at overall optimal frequency $St = 0.075$. (c) Linear gain optimal at each forcing frequency St comparison to Marquet & Sipp (2010). All results at $Re = 500$.

4.3 Linear and non-linear response to harmonic forcing

Applying the linear formulation described in Section 5.2.2 to the 2D backward facing step flow, the optimal forcing and response are calculated. The associated optimal gain obtained around the base flow is very large, with an overall optimal gain of $G_{opt} = 4780$ at $Re = 500$, obtained for a non-dimensional frequency of $St = 0.075$ the same as that reported by Marquet & Sipp (2010) and Boujo & Gallaire (2015). This optimal forcing at 0.075 will be used throughout the paper unless stated otherwise $\boldsymbol{f}_1 = \boldsymbol{f}_{opt}$, although the methodology is independent of the shape and frequency of the forcing and any body or boundary harmonic forcing could be used. We chose $Re = 500$ for simplicity of comparison to literature (Boujo & Gallaire (2015), Blackburn *et al.* (2008), Barkley *et al.* (2002), Marquet & Sipp (2010)).

The large optimal gain implies that linear prediction has a small region of validity since the nonlinear effects enter at small forcing amplitudes A as illustrated in Fig. 4.3(a), where the nonlinear gain decreases rapidly with an increase of the forcing amplitude. This effect is exacerbated because the chosen forcing is optimal $\boldsymbol{f}_1 = \boldsymbol{f}_{opt}$ and presents a complex structure

(Fig. 4.2) that can be attained only numerically. Therefore, in any real experiment the forcing would project poorly on the optimal yielding a much weaker linear gain and thus requiring larger forcing amplitude A to achieve such nonlinear saturation.

The same saturation process is represented differently through the response amplitude in Fig. 4.3(b) defined as the square root of the energy of the fluctuation. Note how the strong saturation of the DNS response for large forcing amplitudes A entails a discrepancy of orders of magnitude as compared to the linear response. The insets in Fig. 4.3(b) show snapshots of the fluctuating velocity at different forcing amplitudes. The energy maximum of the response experiences a clear migration upstream during the saturation process reducing the mean recirculation bubble. A similar tendency has been previously encountered in the cylinder flow and described by Zielinska *et al.* (1997). This migration is enforced by the modification of the base flow into the mean flow due to the forcing of the Reynolds stress as described by Barkley (2006) and thoroughly examined in Mantič-Lugo *et al.* (2014). Fig. 4.3(a) illustrates how the Reynolds stress forcing moves also upstream with an increase in harmonic forcing amplitude A along with the modifications of the response that creates it. In other words, increasingly stronger harmonic forcing entail stronger response which in turn creates stronger Reynolds stresses that modify the mean flow and yield saturation which reduces the response in comparison to its linear prediction.

4.4   Asymptotic expansion around the base flow

We introduce an asymptotic expansion keeping terms of higher order in an attempt to capture the dynamics of the response saturation where the classical linear approach fails (Fig. 4.3). The asymptotic expansion is carried around the base flow $\boldsymbol{U}_B = \boldsymbol{U}_0$ in the same fashion as the one used to obtain the amplitude equation for the cylinder flow described in Sipp & Lebedev (2007). In the amplitude equation the small parameter ϵ corresponds to the departure from threshold by the Reynolds number modification. While on the contrary, in the present case the Reynolds number is fixed and the selected small parameter $\epsilon = A$ is the amplitude of the normalized forcing $\boldsymbol{f}_1$ (Section 5.2.2).

For the sake of clarity we separate the steady terms $\boldsymbol{U} = \sum_{n=0}^{\infty} \epsilon^n \boldsymbol{u}_{0,n}$ and unsteady terms $\boldsymbol{u}' = \sum_{n=0}^{\infty} \sum_{p=1}^{\infty} \epsilon^n \boldsymbol{u}_{p,n} e^{ip\omega t}$ of the asymptotic expansion relating them to mean flow and fluctuation modifications. We use the following notation for $\boldsymbol{u}_{p,n}$; the first subindex p corresponds to the frequency and the second subindex n corresponds to the order. Then we need to introduce the Reynolds decomposition $\boldsymbol{u}(\boldsymbol{x}, t) = \boldsymbol{U}(\boldsymbol{x}) + \boldsymbol{u}'(\boldsymbol{x}, t) = \boldsymbol{U}_B(\boldsymbol{x}) + \Delta\boldsymbol{U}(\boldsymbol{x}) + \boldsymbol{u}'(\boldsymbol{x}, t)$. The instantaneous flow is expressed as a mean flow $\boldsymbol{U} = \langle \boldsymbol{u} \rangle$ plus a pure fluctuation $\boldsymbol{u}'$ verifying $\langle \boldsymbol{u}' \rangle = 0$, where $\langle \rangle$ denotes time-averaging and $\Delta\boldsymbol{U}$ corresponds to the base flow modification. Injecting the Reynolds decomposition in the full NSE we obtain a set of two coupled equations,
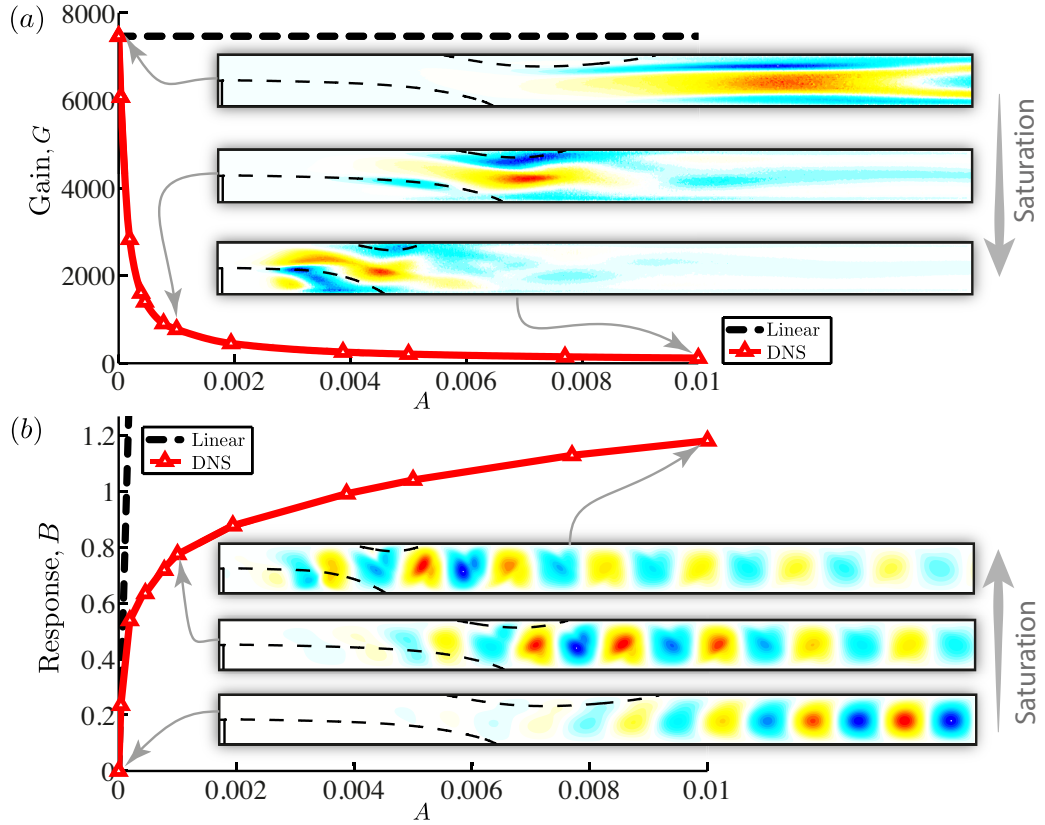
Figure 4.3 – (a) Gain and (b) response of the linear prediction around the base flow compared to the nonlinear saturated DNS for the optimal forcing at $St = 0.075$ and $Re = 500$. The insets show the Reynolds stress divergence in the x-direction and the response or, in other words, the pure fluctuating velocity $\boldsymbol{u}'$ in the y-direction.

$$\mathcal{N}(\boldsymbol{U}) = -\langle(\boldsymbol{u}' \cdot \nabla)\boldsymbol{u}'\rangle \tag{4.13a}$$

$$\partial_t \boldsymbol{u}' + \mathcal{L}_{\boldsymbol{U}}(\boldsymbol{u}') = -(\boldsymbol{u}' \cdot \nabla)\boldsymbol{u}' + \langle(\boldsymbol{u}' \cdot \nabla)\boldsymbol{u}'\rangle + \boldsymbol{f} \tag{4.13b}$$

The mean flow $\boldsymbol{U}$ arises as a result of the steady mean flow equation (4.13a) while the perturbation or forced response equation (4.13b) governs the time dependent field $\boldsymbol{u}'$. Through this decomposition it is possible to isolate easily two significant nonlinear terms of the fluctuation interacting with itself. First, the right hand side (RHS) of (4.13a), which corresponds to the Reynolds stress forcing $\langle(\boldsymbol{u}' \cdot \nabla)\boldsymbol{u}'\rangle$, a mean momentum addition on $\boldsymbol{U}$ due to the nonlinear interaction of the time dependent fluctuation $\boldsymbol{u}'$. Second, the nonlinear RHS of (4.13b), $(\boldsymbol{u}' \cdot \nabla)\boldsymbol{u}' - \langle(\boldsymbol{u}' \cdot \nabla)\boldsymbol{u}'\rangle$, represents the time dependent, zero mean, momentum addition from the nonlinear interactions of different harmonics in $\boldsymbol{u}'$. Note that the coupled equations are exact as no simplification was performed at this stage, and the time dependent perturbation $\boldsymbol{u}'$ does not have to be small compared to the mean $\boldsymbol{U}$.

65

4.4.1 Zeroth order

The zeroth order corresponds to the base flow $\boldsymbol{u}_{0,0} = \boldsymbol{U}_B$ solution of the steady nonlinear NS,

$$\mathcal{N}(\boldsymbol{u}_{0,0}) = 0 \tag{4.14}$$

4.4.2 First order

The 1st order solution corresponds to the classical linear response $\epsilon \boldsymbol{u}_{1,1} = \boldsymbol{u}_{1B}$ (Section 5.2.2) or first harmonic with the same frequency as the forcing $\boldsymbol{f}_1 = \epsilon \boldsymbol{f}_{1,1}$ with amplitude $\epsilon = A$,

$$\epsilon[i\omega + \mathcal{L}_{\boldsymbol{U}_B}]\boldsymbol{u}_{1,1} = \epsilon \boldsymbol{f}_{1,1} \tag{4.15}$$

Note that there is no mean flow contribution at first order, $\boldsymbol{u}_{0,1} = 0$

4.4.3 Second order

The 2nd order has two terms, one steady and one unsteady. Both terms are forced by the interaction of the first order response with itself,

$$\epsilon^2 \mathcal{L}_{\boldsymbol{U}_B} \boldsymbol{u}_{0,2} = -\epsilon^2 \left((\bar{\boldsymbol{u}}_{1,1} \cdot \nabla)\boldsymbol{u}_{1,1} + (\boldsymbol{u}_{1,1} \cdot \nabla)\bar{\boldsymbol{u}}_{1,1} \right) = -\epsilon^2 \boldsymbol{F}_{\boldsymbol{u}_1} \tag{4.16a}$$
$$\epsilon^2 [i2\omega + \mathcal{L}_{\boldsymbol{U}_B}]\boldsymbol{u}_{2,2} = -\epsilon^2 (\boldsymbol{u}_{1,1} \cdot \nabla)\boldsymbol{u}_{1,1} \tag{4.16b}$$

The steady term (4.16a) corresponds to the modification of the base flow to the mean flow due to the steady Reynolds stress forcing $\boldsymbol{F}_{\boldsymbol{u}_{1,1}}$. Whilst, the unsteady term (4.16b) corresponds to the second harmonic $\boldsymbol{u}'_{2,2} = \epsilon^2 \boldsymbol{u}_{2,2} e^{i2\omega t} + cc$. oscillating at double frequency 2ω. It appears as a solution of the linear system slaved by the forcing of the first harmonic interacting with itself,

4.4.4 Third order

The third order presents two unsteady equations,

$$\epsilon^3 [i\omega + \mathcal{L}_{\boldsymbol{U}_B}]\boldsymbol{u}_{1,3} = -\epsilon^3 \left((\boldsymbol{u}_{0,2} \cdot \nabla)\boldsymbol{u}_{1,1} + (\boldsymbol{u}_{1,1} \cdot \nabla)\boldsymbol{u}_{0,2} \right)$$
$$-\epsilon^3 \left((\boldsymbol{u}_{2,2} \cdot \nabla)\bar{\boldsymbol{u}}_{1,1} + (\bar{\boldsymbol{u}}_{1,1} \cdot \nabla)\boldsymbol{u}_{2,2} \right) \tag{4.17a}$$
$$\epsilon^3 [i3\omega + \mathcal{L}_{\boldsymbol{U}_B}]\boldsymbol{u}_{3,3} = -\epsilon^3 ((\boldsymbol{u}_{2,2} \cdot \nabla)\boldsymbol{u}_{1,1} + (\boldsymbol{u}_{1,1} \cdot \nabla)\boldsymbol{u}_{2,2}) \tag{4.17b}$$

The first equation (4.17a) oscillates at the harmonic forcing frequency corresponding to an adjustment of the first harmonic response. This 3rd order nonlinear adjustment is enforced by two terms which entail two independent physical meanings. The first term in (4.17a), $-\epsilon^3 \left((\boldsymbol{u}_{0,2} \cdot \nabla)\boldsymbol{u}_{1,1} + (\boldsymbol{u}_{1,1} \cdot \nabla)\boldsymbol{u}_{0,2} \right)$, relates to the mean flow modification due to the Reynolds stress, in other words, it accounts for the nonlinear interaction on the r.h.s. of the mean flow steady equation (4.13a). The second forcing term $-\epsilon^3 \left((\boldsymbol{u}_{2,2} \cdot \nabla)\bar{\boldsymbol{u}}_{1,1} + (\bar{\boldsymbol{u}}_{1,1} \cdot \nabla)\boldsymbol{u}_{2,2} \right)$ corre-

sponds to the interaction of the first harmonic $\boldsymbol{u}_{1,1}e^{i\omega t}$ with the second $\boldsymbol{u}_{2,2}e^{i2\omega t}$.

The second equation (4.17b) at 3rd order corresponds to the third harmonic oscillating at three times the forcing frequency 3ω. It is slaved by the interactions of the first ω and second harmonic 2ω.

4.4.5 Synthesis

Stopping at the third order our asymptotic expansion can be summarized as

$$\boldsymbol{U}(x) \simeq \boldsymbol{u}_{0,0}(x) + \epsilon^2 \boldsymbol{u}_{0,2}(x) \tag{4.18a}$$

$$\boldsymbol{u}'(x,t) \simeq \epsilon \boldsymbol{u}_{1,1}(x)e^{i\omega t} + \epsilon^2 \boldsymbol{u}_{2,2}(x)e^{i2\omega t} + \epsilon^3\left(\boldsymbol{u}_{1,3}(x)e^{i\omega t} + \boldsymbol{u}_{3,3}(x)e^{i3\omega t}\right) + cc. \tag{4.18b}$$

The linear equations at each order can be solved one after another to obtain the different terms. Introducing the expansion in the gain definition of the response, we obtain at lower order the modified gain

$$G_{3Ord}^2 = \frac{\|\boldsymbol{u}'\|^2}{\|\boldsymbol{f}\|^2} = G_1^2\left(1 + \frac{\epsilon^2}{G_1^2}(K_{2,2} + K_{1,3})\right), \tag{4.19}$$

where

$$K_{2,2} = \frac{\int_\Omega \boldsymbol{u}_{2,2}^2 d\Omega}{\|\boldsymbol{f}_{1,1}\|^2} > 0 \text{ and } K_{1,3} = \frac{\int_\Omega 2\boldsymbol{u}_{1,1}\cdot\boldsymbol{u}_{1,3}d\Omega}{\|\boldsymbol{f}_{1,1}\|^2}. \tag{4.20}$$

$K_{2,2}$ is the gain correction due to the energy of the second harmonic while, $K_{1,3}$ relates to energy modification due to the correction of the first harmonic at 3rd order (4.17a). In Fig. 4.4 are compared the linear gain G_1, the saturation of the fully nonlinear DNS gain G_{DNS} and the weakly nonlinear gain correction at 3rd order G_{3Ord}. As one could expect, the weakly nonlinear theory predicts well the initial saturation trend for small forcing amplitudes ϵ, and it starts failing for larger forcing amplitudes. Fig. 4.4 illustrates how the influence of the second harmonic is small compared to the first harmonic modification at 3rd order, since the elimination of its correction factor $K_{2,2}$ does not produce any change on the saturation curve, $|K_{2,2}| << |K_{1,3}|$. We thus neglect the influence of the second and third harmonic of (4.18b) and restrict our attention to the response at the same frequency as the forcing (4.15)-(4.17a). We observe that $K_{1,3} < 0$, indeed accounting for the saturation.

As expressed above, the 3rd order adjustment of the response results from two different physical phenomenons. We can separate them and account independently for their role in the saturation process thanks to the linearity of the problem. The 3rd order term forced only by the mean flow modification reads

$$\epsilon^3[i\omega + \mathscr{L}_{\boldsymbol{U}_0}]\boldsymbol{u}_{1,3}^0 = -\epsilon^3\left((\boldsymbol{u}_{0,2}\cdot\nabla)\boldsymbol{u}_{1,1} + (\boldsymbol{u}_{1,1}\cdot\nabla)\boldsymbol{u}_{0,2}\right), \tag{4.21}$$
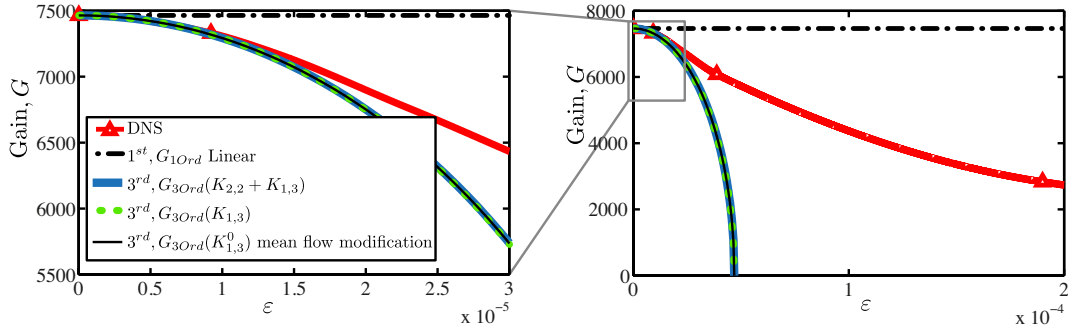
Figure 4.4 – Gain of the response for the optimal forcing at frequency $St = 0.075$ and $Re = 500$. Linear prediction (dash dot line), 3rd order weakly nonlinear correction (solid thick line), 3rd order weakly nonlinear correction of the first harmonic only at the forcing frequency (dot line), 3rd order weakly nonlinear correction only by mean flow modification (thin solid line) and DNS results (thick solid line with triangles).

and thus a new gain modification factor $K_{1,3}^0$

$$K_{1,3}^0 = \frac{\int_\Omega 2\boldsymbol{u}_{1,1} \cdot \boldsymbol{u}_{1,3}^0 d\Omega}{\|\boldsymbol{f}_{1,1}\|^2} \tag{4.22}$$

can be retrieved accounting solely for the mean flow modification effect. Fig. 4.4 shows how the new gain adjusted exclusively by the mean flow modification follows precisely the curve of the full 3rd order gain. It therefore appears that the nonlinear saturation process is captured mainly by the Reynolds stress modification and not by the second harmonic interaction, raising the importance of the mean flow in the saturation process in a similar way as for the cylinder flow (Barkley (2006) and Mantič-Lugo *et al.* (2014)).

4.5 Self-consistent model.

The results of the weakly nonlinear analysis summarised in Fig. 4.4 suggest that the energy transfer between different frequencies gathered in the RHS of (4.13b) is of less importance to capture the saturation process than the Reynolds stress nonlinearity. Therefore, we move one step further in nonlinearity and present a model that keeps the Reynolds stress nonlinear term RHS of (4.13a), while it neglects the interaction between higher harmonics RHS of (4.13b). The model is composed by the mean flow equation, which is forced by the Reynolds stress, connected to the linearized perturbation equation. Thus, the full instantaneous response is approximated by one single harmonic $\boldsymbol{u}(\boldsymbol{x}, t) = \boldsymbol{U}(\boldsymbol{x}) + \boldsymbol{u}'(\boldsymbol{x}, t) \simeq \boldsymbol{U}(\boldsymbol{x}) + \boldsymbol{u}_1'(\boldsymbol{x}, t)$, where $\boldsymbol{u}_1'(x, t) = \boldsymbol{u}_1(x)e^{i\omega t} + cc.$. The higher harmonics are neglected also because the fluctuating response signal $\boldsymbol{u}'(x, t)$ is dominated by the first harmonic even for a strongly saturated DNS response to high amplitude forcing A. Extracting the different harmonics of the nonlinear DNS response $\boldsymbol{u}'(x, t)$ by Fourier series, we have indeed obtained an energy of the second harmonic less than 3% of the fundamental frequency for a forcing amplitude $A = 0.01$. The first

harmonic approximation of a nonlinear response has been recently used for the description of combustion instabilities, where Noiray *et al.* (2008) have applied the concept of describing function (i.e. a nonlinear extension of the linear transfer function) to flames.

Notice that the weakly nonlinear solution arises from decoupled equations that are solved one after another, postulating an explanation for its limitation to small forcing amplitude $A = \epsilon$. This limitation is overcome in the present model by coupling the mean flow and perturbation equation. The coupled equations of the self-consistent model for harmonically forced flows can be written as

$$\mathcal{N}(\boldsymbol{U}) = -2\Re\left((\bar{\boldsymbol{u}}_1 \cdot \nabla)\boldsymbol{u}_1\right), \tag{4.23a}$$

$$i\omega\boldsymbol{u}_1 + \mathcal{L}_{\boldsymbol{U}}(\boldsymbol{u}_1) = \boldsymbol{f}_1, \tag{4.23b}$$

where the amplitude of the response is dictated linearly by the forcing through the mean flow resolvent operator $\mathcal{R}(\omega) = (i\omega + \mathcal{L}_{\boldsymbol{U}})^{-1}$ and ultimately the gain. Conceptually the model is the forced counterpart of the self-consistent model presented recently for amplifiers (Mantič-Lugo *et al.* (2014)) where the linear equation corresponded to an eigenvalue problem and the amplitude was dictated by the marginality criterion of the system, $\sigma = 0$. It also relates closely to the SSST theory presented by Farrell & Ioannou (2012) for turbulent flows, where the linear response to white forcing is coupled to the mean flow modification through the Reynolds stress. However, in the present case the forcing is harmonic and not uncorrelated like white noise, thus the linear response to forcing can be used and the Lyapunov equation is not required. Furthermore, the semi-linear model assumes a steady saturated mean flow while the SSST theory is characterised by a slowly varying ensemble averaged mean flow. The self-consistent model presents a simplified and more transparent system than the DNS while still capturing the saturation process.

4.5.1 Model solution

The coupled equations (4.23) of the self-consistent model need to be solved in an iterative way for a given target amplitude of the harmonic forcing A. There are two options, both starting the iterative process from the steady flow base flow $\boldsymbol{U}_B$ with its corresponding linear response $\boldsymbol{u}'_{1B}$ (4.15).

Amplitude stepping

The system (4.23) is solved for a given target forcing A subdividing it in intermediate amplitude steps $0 < A^k < A$ and coupling the nonlinear system at each amplitude step using a fixed point method. The same methodology was applied on the cylinder flow in Mantič-Lugo *et al.* (2014). The stepping is required due to the important variation of the spatial structure between the initial base flow $\boldsymbol{U}_B$ and the corresponding final mean flow $\boldsymbol{U}$, as clearly illustrated in Fig. 4.3 caused by the recirculation region variation. For a mean flow guess $\boldsymbol{U}_g^{(n)}$ (starting with the base

flow) the linear forced response $\boldsymbol{u}_{1g}^{(n)}$ is calculated. Then it is used to construct the Reynolds stress forcing in (4.23a) to obtain an updated mean flow $\boldsymbol{U}_c$, calculated nonlinearly using the Newton–Raphson method. This mean flow update $\boldsymbol{U}_c$ serves to generate a new guess $\boldsymbol{U}_g^{(n+1)} = \gamma \boldsymbol{U}_c + (1 - \gamma)\boldsymbol{U}_g^{(n)}$ using a relaxation factor $0 < \gamma < 1$ to ensure convergence. Finally, the new guess $\boldsymbol{U}_g^{(n+1)}$ is coupled back to the linear forcing equation (4.23b) to obtain the new response $\boldsymbol{u}_{1g}^{(n+1)}$, closing the loop. The convergence is very fast for small forcing amplitudes but the computational time increases substantially for larger amplitudes, reaching a maximum forcing amplitude that can be achieved (Mantič-Lugo *et al.* (2014)).

Pseudo time relaxation

The steady mean flow equation is modified to a pseudo time τ dependent equation, which represents the variation of the instantaneous mean flow from base flow $\boldsymbol{U}_B$ to the saturated mean flow $\boldsymbol{U}$. The amplitude of the forcing is a smooth ramp function of time $A(\tau)$ that goes from 0 to the objective forcing amplitude A, staying at A until the variations in the flow fields are negligible. At each pseudo time step k of the instantaneous mean flow $\boldsymbol{U}^k$ the linear forcing equation is solved and the new linearly forced response $\boldsymbol{u}_1^k$ is updated into the Reynolds stress for the next time step. The time integration is performed by a semi-implicit backward Euler method, summarized as

$$\frac{\boldsymbol{U}^{k+1} - \boldsymbol{U}^k}{\delta\tau} + \mathscr{L}_{\boldsymbol{U}^k}(\boldsymbol{U}^{k+1}) - (\boldsymbol{U}^k \cdot \nabla)\boldsymbol{U}^k = -2\Re\left((\bar{\boldsymbol{u}}_1^k \cdot \nabla)\boldsymbol{u}_1^k\right) \tag{4.24a}$$

$$[i\omega + \mathscr{L}_{\boldsymbol{U}^k}]\boldsymbol{u}_1^k = A(\tau)\boldsymbol{f}_{1,1}, \tag{4.24b}$$

where $k + 1$ represents the solution for the next step. Notice how the standard nonlinear equation for $k+1$ is approximated by its linear counterpart and a nonlinear term of the previous time step k is subtracted to retrieve exactly the nonlinear mean flow equation (4.13a) when the steady mean flow at the saturation is reached $\boldsymbol{U}_k = \boldsymbol{U}_{k+1}$, hence $\mathscr{L}_{\boldsymbol{U}^k}(\boldsymbol{U}^{k+1}) - (\boldsymbol{U}^k \cdot \nabla)\boldsymbol{U}^k = \mathscr{N}(U^k)$.

This methodology is similar to the Amplitude stepping previously described, but reducing the amplitude step between iterations to a very small value δA and adding an extra dynamical term $(\boldsymbol{U}^{k+1} - \boldsymbol{U}^k)/\delta\tau$. The advantages of this method are two fold. First, the nonlinear equation of the mean flow is replaced by a linear system requiring, however, a reduction in the amplitude step. Second, the mean flow is not locked to a steady solution for each amplitude A_k, we replace the relaxation parameter by a pseudo time step allowing for physical advection of disturbances and thus stabilizing the convergence until a purely steady solution is attained. Independently of the objective forcing amplitude A, a minimum of iterations is required thus making the method not suitable for small amplitudes. The pseudo time method should not be confused with a DNS, instead it is part of possible iterative methods that could be used to obtain a steady solution to the present nonlinear system (4.23).
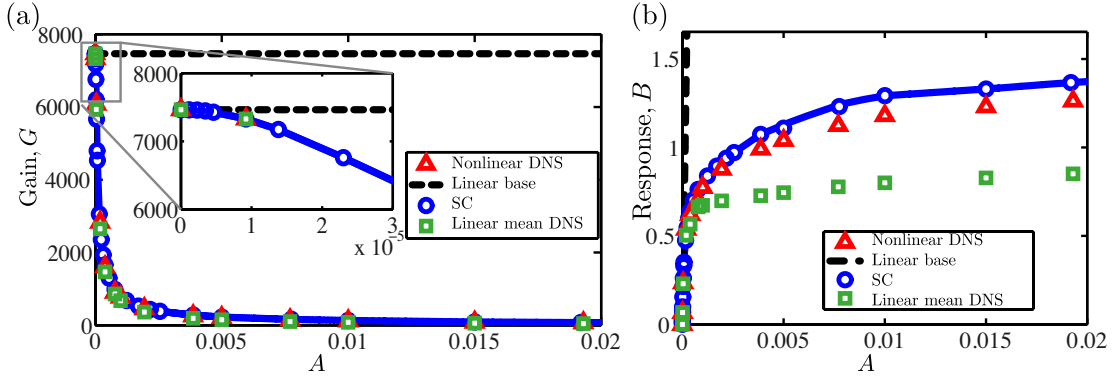
Figure 4.5 – (a) Gain and (b) response saturation as function of forcing amplitude A for DNS (triangles) compared to self-consistent results (solid line with circles) and linear response u_{1DNS} around the saturated mean flow from DNS (squares). Forcing with optimal structure at frequency $f = 0.075$ and $Re = 500$.

4.6 Results: Gain saturation and mean flow distortion

The self-consistent model predicts accurately the response and gain of the exact DNS capturing the strong nonlinear effects of the saturation as depicted in Fig. 4.5. The coupling between the mean flow and response equation inherent to the semi-linear model allows to overcome the limitations of the weakly nonlinear theory. Fig. 4.5 confirms the picture of the proposed semi-linear model where the Reynolds stress plays the main role in the saturation process while higher harmonic interactions are negligible.

In many cases reported in literature, linear stability analysis applied to the mean flow predicted the accurate frequency and structure of the fluctuations (Barkley (2006)). We therefore calculate the linear response of the harmonic forcing (4.4) around the saturated DNS mean flow $\boldsymbol{U}_{DNS}$ at each forcing amplitude A, as reported in Fig. 4.5 with squares. Surprisingly, it overpredicts the saturation (Fig. 4.5(b)), providing a poorer estimation of the gain and response amplitude when compared to the present semi-linear model. This discrepancy could be in large part because the linear response is calculated a posteriori and decoupled from the mean flow equation, suggesting that the coupling between the mean flow and perturbation equation present in the self-consistent model and also in the exact DNS is relevant.

The spatial distribution of the saturated response calculated by the self-consistent model accurately predicts the full nonlinear DNS as presented in Fig. 4.6 for a forcing $A = 0.01$. The wavelength and the position of the largest amplification of the self-consistent response match the exact DNS solution for both u'_x and u'_y fluctuations. The linear response around the DNS mean flow also resembles the full DNS structure, despite its less accurate approximation of the saturated gain (Fig. 4.5(b)). It should be noted that the discrepancies are minimal when compared to the structure of the linear response around the base flow as illustrated in Fig. 4.3.

As illustrated above in Fig. 4.3, the Reynolds stress varies strongly with the forcing amplitude,
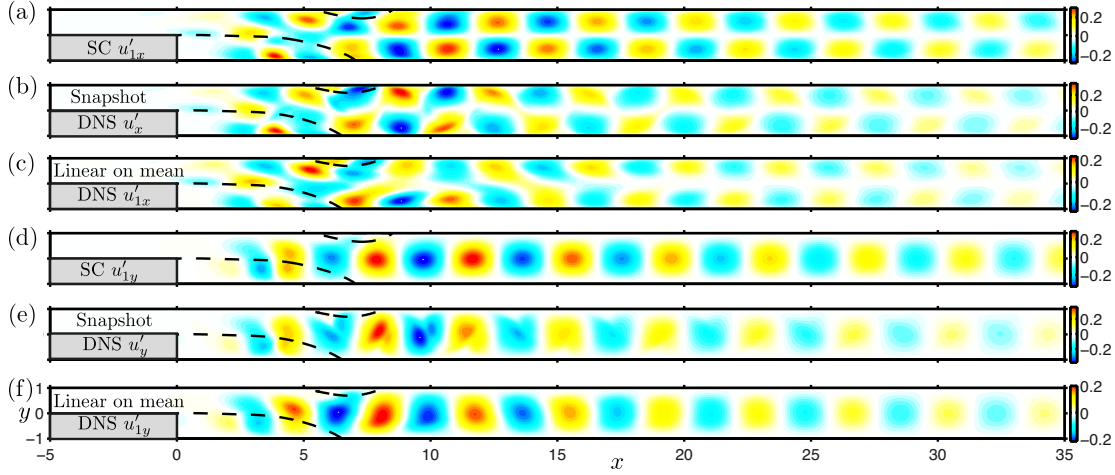
Figure 4.6 – Comparison of the response structure in x and y direction for the self-consistent model u_1 (a,d), snapshot of the DNS u' (b,e), and linear response around the DNS mean flow u_{1DNS} (c,f). High saturation level with a forcing amplitude $A = 0.01$, frequency $St = 0.075$ and $Re = 500$.

however, thanks to the coupling present in the semi-linear model, the structure of the Reynolds stress divergence of the DNS and self-consistent model compare very closely as depicted in Fig. 4.7. In this case, the Reynolds stress divergence calculated from the linear prediction around the mean flow differs substantially from the exact DNS solution. The Reynolds stress forcing is crucial to obtain the accurate mean flow with the correct recirculation region and thus, through a proper coupling, the corresponding response.
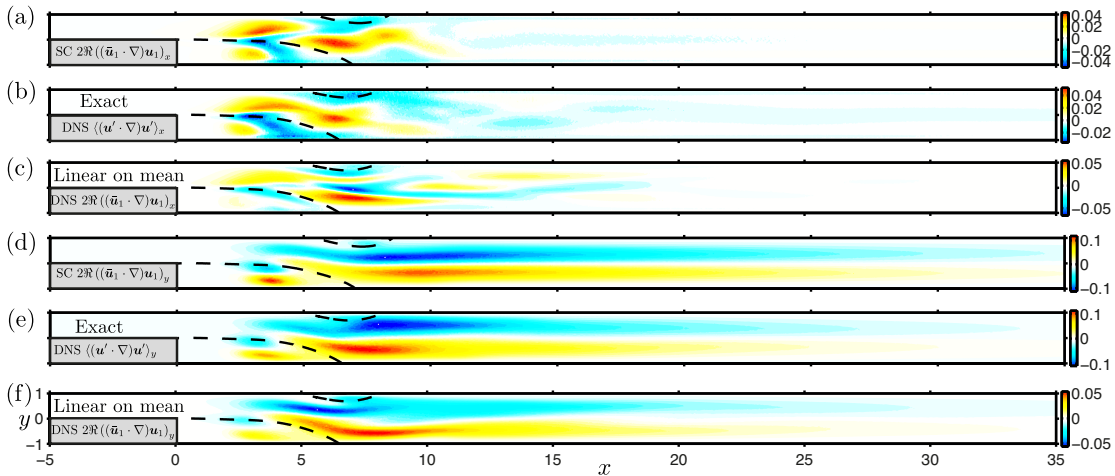
Figure 4.7 – Comparison of the Reynolds stress divergence structure in x and y direction for the self-consistent model $2\Re((\bar{\boldsymbol{u}}_1 \cdot \nabla)\boldsymbol{u}_1)$ (a,d), exact average from the DNS $\langle(\boldsymbol{u}' \cdot \nabla)\boldsymbol{u}'\rangle$ (b,e), and construction from the linear response around the DNS mean flow $2\Re((\bar{\boldsymbol{u}}_{1DNS} \cdot \nabla)\boldsymbol{u}_{1DNS})$ (c,f). High saturation level with a forcing amplitude $A = 0.01$, frequency $St = 0.075$ and $Re = 500$.
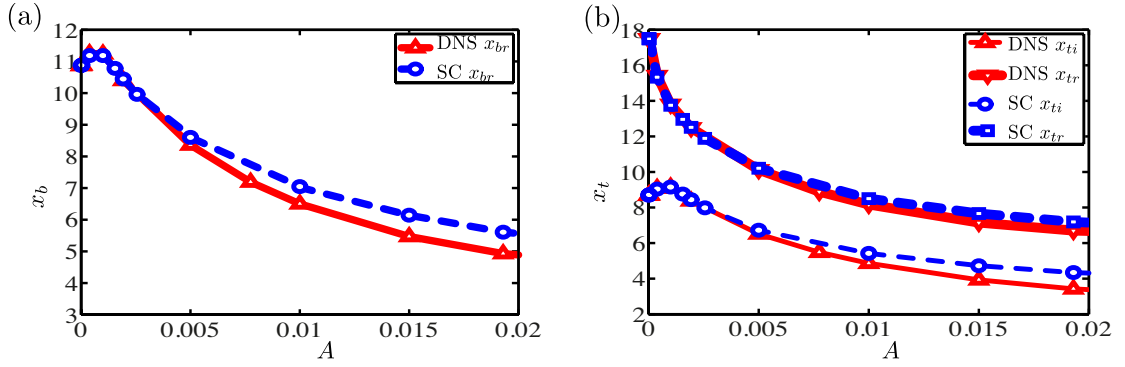
Figure 4.8 – Position of the recirculation bubbles, (a) bottom and (b) top, as a function of the forcing amplitude A for the DNS and self-consistent model for the optimal forcing frequency $St = 0.075$ and $Re = 500$.

A more quantitative comparison between the self-consistent model and DNS mean flow is summarized in Fig. 4.8, where the positions of the recirculation regions are depicted as a function of the forcing amplitude. The self-consistent model approximates precisely the exact recirculation bubbles of the nonlinear DNS, this results from the accurate calculation of the Reynolds stress by the self-consistent model which allows to obtain the correct mean flow. At high forcing the saturation is very strong and higher order nonlinear effects which are neglected in the semi-linear model start playing a more important role, explaining the slight divergence between the self-consistent model results and the DNS. Nevertheless, the self-consistent model captures even the non-monotonous trend of the recirculation bubble position present in the exact DNS solutions, which would be missed by a linear prediction around the base flow.

The frequency dependence of the saturation process of the gain starting from the linear prediction to a forcing amplitude $A = 0.001$ is presented in Fig. 4.9. The comparison of the self-consistent saturated gain and the DNS for $A = 0.001$ in Fig. 4.9 shows a very accurate prediction at all frequencies, with only a slight shift in the optimal frequency. More generally, Fig. 4.9 demonstrates that the most responsive frequency does not change much when nonlinear effects are included, as pointed out by the preliminary results of Marquet *et al.* (2010) using random noise forced DNS.

4.7 Discussion and conclusions

We presented an asymptotic expansion around the base flow, inspired by the weakly nonlinear theory applied in the Stuart-Landau amplitude equation for oscillators. The gain correction at third order enforced by the mean flow modification approximates accurately the exact DNS saturation, while the correction due to the interactions between higher harmonics appears to be negligible. A thorough interpretation of the results highlights the Reynolds stress as the key nonlinear term in the saturation process. However, the asymptotic expansion remains valid
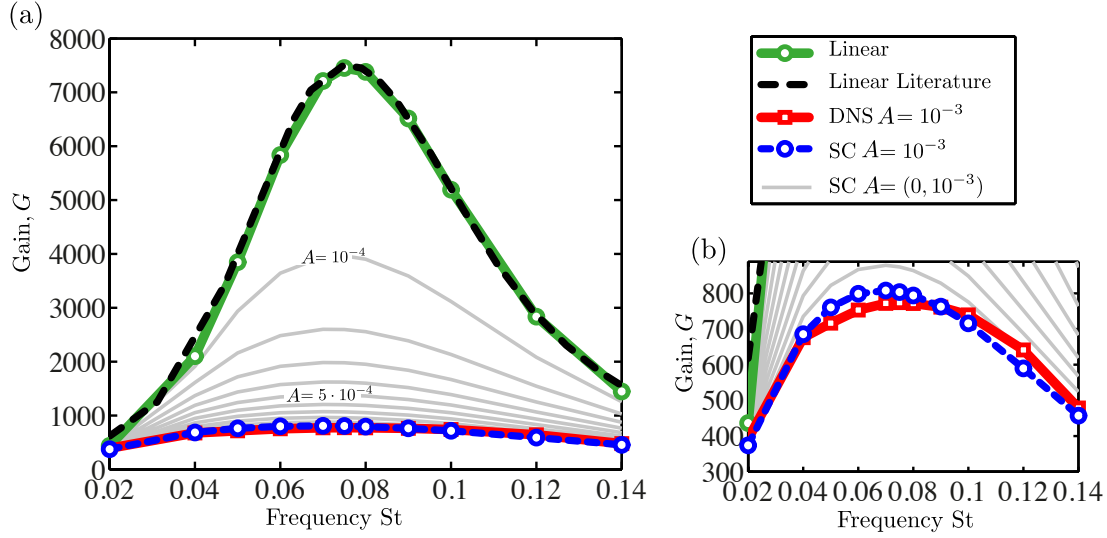
Figure 4.9 – Gain saturation as function of frequency for several forcing amplitudes A. The DNS results are compared to the self-consistent and linear response around the base flow, from literature. The forcing applied has its optimal structure at each frequency and the $Re = 500$.

only for small amplitude forcing.

A self-consistent model (SC) is introduced motivated by the weakly nonlinear results where the mean flow equation is coupled to the linear response through the Reynolds stress. Both equations are coupled by an iterative method. The linear response, around its corresponding coupled mean flow, approximates accurately the fully nonlinear response of the exact DNS simulations in terms of gain and structure. Contrary to the weakly nonlinear theory, the self-consistent model solution is not restricted to a small amplitude harmonic forcing. Furthermore, the self-consistent model calculates the precise Reynolds stress forcing which in turn allows to obtain the correct mean flow as compared to the exact DNS predicting an accurate recirculation bubble shortening related to the saturation mechanism.

The self-consistent model results highlight the Reynolds stress as the driving force for the response saturation in a forced backward-facing step flow, in the same fashion as the case of the cylinder wake flow reported in Mantič-Lugo *et al.* (2014), where a conceptually similar model is applied to the unstable cylinder flow with the saturation mechanism of the instability dominated by the most unstable eigenmode as suggested by Malkus (1956) and Stuart (1958). These oscillators and amplifiers share conceptually a similar saturation mechanism; the increasingly growing fluctuation, which could be accurately approximated by the most unstable eigenmode or the linear response respectively, saturates through the modification of the mean flow by the forcing of the Reynolds stress.

A fundamental aspect of the model is that the full nonlinear response of the DNS is approximated by only the first harmonic, neglecting the higher frequency generation. Nevertheless, the self-consistent model is still capable to approximate accurately the nonlinear gain, re-

sponse and mean flow at different forcing frequencies and amplitudes. While reminiscent of the nonlinear transfer function (the so-called describing function) used to assess the stability of flames in combustion in Noiray *et al.* (2008), it should be highlighted that the self-consistent solution is calculated *a priori*, without resorting to any DNS or experiments results, clarifying the different physical mechanisms involved in the saturation process.

It remains to be seen whether the present semi-linear model works for other globally stable laminar flows excited by harmonic forcing; i.e. jets, etc. However, it is not expected to work directly for turbulent or chaotic flows unless a separation of scales is applied and turbulent and coherent Reynolds stress terms are calculated independently.

5 | Saturation mechanism of the response to stochastic forcing

In the previous chapters the self-consistent model was applied to a prototype oscillator flow and a harmonically forced amplifier flow. In both cases a clear quasi-monochromatic fluctuation was involved. However, in general, flows are subjected to random noise. Therefore, it is of relevance to study and describe the dynamics of flows under more natural settings, like stochastic noise. Amplifiers are well known for exhibiting large response under external excitations in a particular frequency range. In general a linear study of the response describes the flow behaviour for very small amplitude of the noise. Nonetheless, once the noise or external stochastic disturbance starts to be important, the response becomes nonlinear.

In this context, this chapter presents the nonlinear dynamics of the response to noise in the two-dimensional backward-facing step flow. The previously introduced nonlinear concepts applied for harmonically oscillating flows are expanded to a stochastically forced flow. The response to stochastic forcing has been widely treated in literature with the use of the covariance matrix of the stochastic response (Farrell & Ioannou (1993, 1996, 2012)) and its dynamical behaviour governed by the linear Lyapunov equation. However, in the present approach the forcing and response are treated in the frequency domain, linking the stochastic response to its harmonic counterpart. This chapter aims at understanding, by means of the self-consistent model, if the dynamics of the non-linear response to white noise forcing remains governed mainly by the mean flow-linear response coupling, through the Reynolds stress nonlinearity, even in a stochastic setting with broad band spectrum of the excitation and response.

Paper: *The saturation of the response to stochastic forcing in the backward-facing step flow described by a self-consistent model*

The saturation of the response to stochastic forcing in the backward-facing step flow described by a self-consistent model

Vladislav Mantič-Lugo[1] and François Gallaire[1]

1) LFMI, École Polytechnique Fédérale de Lausanne, CH-1015 Lausanne, Switzerland

Selective noise amplifiers are characterised by presenting large linear amplifications to external perturbations in a particular frequency range despite their global linear stability. Applying a stochastic forcing with increasing amplitude, the response undergoes a strong nonlinear saturation when compared to the linear estimation. Rewriting conveniently the stochastic response and forcing in the frequency domain and building upon our previous work, we introduce a predictive model that describes this nonlinear dynamics and apply it to a canonical example of a selective noise amplifier: the backward-facing step flow. The model consists in a mean flow equation coupled to the linear response to forcing at each frequency by means of the Reynolds stress, which is constructed by the integral in frequency of the independent responses. We generalise the model for a response to a white noise forcing δ-correlated in space and time restricting the flow dynamics to its most energetic patterns calculated from the optimal harmonic forcing and response of the flow. The results show an accurate estimation of the response saturation when compared to Direct Numerical Simulations (DNS), while at the same time, the model describes the structure of the response and the mean flow modification. A physical picture emerges wherein the response to white noise modifies the mean flow by the Reynolds stress in the exact manner to attain the correct response amplitude as proposed by the self-consistent model.

Keywords: Shear layers, Instability, Laminar flows, Nonlinear stability, Separated flows, Stochastic

5.1 Introduction

A wide variety of open flows are characterised by their stable nature while presenting high sensitivity to background disturbances. Typically, this behaviour is encountered in boundary layers, mixing layers, jets or separated flows even in the laminar regime at low and intermediate (pre-turbulent) Reynolds numbers. Such behaviour is produced by the convective instabilities and interpreted by the non-normality of the Navier-Stokes system of equations, which is able to amplify perturbations while being advected downstream by means of non-modal mechanisms (Trefethen *et al.* (1993), Chomaz (2005), Schmid (2007)). These flows are sometimes denoted as selective noise amplifiers due to their ability to amplify perturbations in a particular frequency

ranges.

A substantial body of work has been devoted to the study of amplifiers. Nonetheless, classical modal analysis focuses on the eigenvalues and eigenmodes of the linear operator $\mathcal{L}$ that describe the linearised dynamics of the flow around a steady solution. Modal analysis fails however to describe the flow behaviour due to the subcritical nature of the amplifiers. Thereby, other non-modal techniques derived from classical linear algebra are used to characterise the physical behaviour and amplification potential in linearly stable flows. One of the standard approaches to characterise the amplifier dynamics is to look at initial disturbances which lead to the maximum growth and follow the time evolution of this perturbations, described by the leading singular vectors of the time propagator $e^{\mathcal{L}t}$ (Trefethen *et al.* (1993); Farrell & Ioannou (1996); Schmid & Henningson (2001)). Studies of optimal initial perturbation in parallel flows have been carried out by Butler & Farrell (1992); Corbett & Bottaro (2000); Schmid (2007) among others. Caluculations of optimal growth in non-parallel flows have been carried out in spatially developing boundary layers in the works of Akervik *et al.* (2008); Monokrousos *et al.* (2010), Sipp & Marquet (2012); Alizard *et al.* (2009), and in the backward-facing step by Blackburn *et al.* (2008), among others. Another alternative consists in finding the optimal harmonic forcing structures that at frequency ω lead to the most energetic responses. The optimal forcing and corresponding response are described by the singular vector of the resolvent operator $\mathcal{R}(\omega) = (i\omega + \mathcal{L})^{-1}$, see Farrell & Ioannou (1996); Schmid (2007); Garnaud *et al.* (2013); Dergham *et al.* (2013); Boujo & Gallaire (2015). Optimal forcing/response structures have been assessed in plane Couette by Jovanović & Bamieh (2005), while in spatially developing open flows by Akervik *et al.* (2008); Alizard *et al.* (2009); Sipp & Marquet (2012) and particularly for the backward-facing step in Marquet & Sipp (2010); Marquet *et al.* (2010); Boujo & Gallaire (2015); Mantič-Lugo & Gallaire (2015). A slightly different approach is undertaken by Garnaud *et al.* (2013) where, in an attempt to describe more precisely the actual physics involved in the strong noise amplification exhibited in turbulent jets, they apply the optimal gain analysis on a model mean flow instead of the stable steady solution of the NSE (Navier-Stokes equations) as in the previously mentioned studies. In general, both time and frequency approaches describe the most energetic instability mechanisms at play.

Realistic flows are in general subject to unpredictable noise created from different possible sources such as residual turbulence, acoustic disturbances, geometrical defects, etc. In this context Farrell & Ioannou (1993) have studied the response to white noise forcing for parallel flows, reformulating the linear problem as a Lyapunov equation for the covariance matrix that describe the statistically steady state of the response. Following these steps, Farrell & Ioannou (2001) have described a low order approximation of the linear dynamical system for a Couette flow forced by white noise, by extracting the energy ranked coherent structures of the stochastic response and forcing, the so-called empirical orthogonal functions (EOFs) and stochastic optima (SOs), respectively. Dergham *et al.* (2013) introduced a low dimensional model to describe the linear behaviour of the flow around the backward-facing step forced by white noise. The low dimensional model is constructed by the mentioned EOFs and SOs, which in this case are extracted from the most energetic harmonic forcing/response

structures, relating the stochastic structures to the harmonic optima. Another study of the response to white noise forcing is reported in Blackburn *et al.* (2008) for an inlet forcing in the backward-facing step and it shows that the exact stochastic response from the direct numerical simulation (DNS) is well characterised by the optimal perturbances. A relevant description is provided by the study of the sensitivity and control of the response amplification under stochastic forcing. This approach is undertaken by Boujo & Gallaire (2015) in the particular case of the backward-facing step.

The studies introduced above are limited to the linear characterisation of the flow behaviour, thus failing to describe saturation processes or the nonlinear interactions involved in the transition to turbulence in stable flows. A well known example is the saturation of the supercritical instability in the cylinder wake which can be characterised by the nonlinear interaction of the mean flow with the linear perturbation by the Reynolds stress forcing as described in the model introduced by Mantič-Lugo *et al.* (2014, 2015) and initially suggested by Stuart (1958). In other cases, the non-normality of the NSE allows the flow to escape from linearly stable solutions by means of the large amplification of external disturbances, as can be encountered in the transition to turbulence. Thereby, similar models with a coupling between the mean flow and the linear perturbation equation are also used to describe the coherent structures appearing in the transition to turbulence, as in the work of Beaume *et al.* (2015) for parallel shear flow. In a similar nonlinear spirit, the stochastic structural stability theory SSST has been introduced by Farrell & Ioannou (2003, 2012), consisting in a system of equations where the linear response to white noise forcing written as Lyapunov equation (Farrell & Ioannou (1993)) is coupled to the slowly varying ensemble average mean flow by means of the Reynolds stress. The theory is able to describe sustained coherent structures that appear during the transition to turbulence in the three-dimensional Couette flow (Farrell & Ioannou (2012)) as well as in turbulent atmospheric flows described in Farrell & Ioannou (2003), among many others. Most of the piece of work applying these nonlinear models have been devoted to the study of coherent sustained structures in turbulent flows, bu a formalised quantitative physical description of the dynamics involved in the saturation of strong amplifiers under stochastic excitations is still missing.

Motivated by the SSST and the low order modelling based on harmonic optima of Dergham *et al.* (2013), we propose a model to describe the nonlinear dynamics of the response to white noise forcing in a flow with strong amplification and hence capturing its saturation with an increasing forcing amplitude. The model is applied to a canonical amplifier flow, the incompressible backward-facing step, which is an archetypical flow in fundamental studies used to understand separation in abrupt changes of geometry. The flow is globally stable at the two Reynolds numbers considered in this study $Re = 500$ and $Re = 700$ presenting the threshold for three-dimensional global instability at $Re_{cr} \sim 748$ (Barkley *et al.* (2002); Lanzerstorfer & Kuhlmann (2012)), staying stable in two-dimensional for Reynolds at least up to $Re \sim 1500$ and presenting mainly a two dimensional response to white noise as described by Blackburn *et al.* (2008), supporting the two dimensional analysis. The work presented herein comes as an extension to white noise forcing of the model introduced in Mantič-Lugo

& Gallaire (2015) that describes the nonlinear saturation of the response to harmonic forcing. Where the mean flow is coupled to a linear response to harmonic forcing around the mean flow by means of the Reynolds stress. The term in the response equation that represents the nonlinear interaction of the response with itself is neglected following the results of asymptotic analysis. First, we reformulate the self-consistent model in the frequency domain to account for the stochastic nonlinear response to a band limited white noise forcing with a fixed spatial structure. The results illustrate an accurate estimation of the saturation as much as they describe the main structure of the response and mean flow. Finally, we generalise the approach to a δ-correlated white noise in space and time restricting the flow dynamics to its most energetic patterns extracted from the harmonic optimal forcing/response pairs at each frequency. The results show that the nonlinear stochastic response can be well treated in the frequency domain even for complex nonlinear settings and it emphasises the Reynolds stress as the key nonlinear term to describe correctly the saturation mechanism. It highlights the importance of the mean flow and its relation to the fluctuation as discussed by Barkley (2006); Mittal (2008); Turton *et al.* (2015); Mantič-Lugo *et al.* (2014) and Mantič-Lugo *et al.* (2015), among others.

The paper is structured as follows. Section 5.2 introduces the physical domain and the linear description of the response. Section 5.3 describes the temporal stochastic forcing, introduces the model and provides comparison with DNS results. The model rewritten for spatio-temporal stochastic forcing is introduced in Section 5.4, before conclusions are drawn in Section 5.5.

5.2 Problem formulation

5.2.1 Flow configuration and governing equations

We consider the response to forcing of a laminar incompressible flow around the two- dimensional backward-facing step. The flow configuration is depicted in Fig. 5.1. An inlet channel with height h and legth $L_i = 5h$ encounters a step of height h and expands into a wider channel of height $H = 2h$ and length L_o, hence determining an expansion ratio $\Xi = h/H = 0.5$. The inlet boundary condition at Γ is a plane Poiseuille profile $\boldsymbol{u}_{pois}$ with a centerline (maximum) velocity U_∞ plus a general inlet forcing $\boldsymbol{f}$. The centerline velocity U_∞ defines the Reynolds number $Re = U_\infty h/\nu$, where h is the inlet height and ν is the kinematic viscosity. A non-slip boundary condition is imposed on the side walls boundary Γ_w and an outflow condition at the end of the domain Γ_o. The non-dimensional frequency is defined by the Strouhal number $St = f_{Hz} h/U_\infty$ and related to the non-dimensional angular frequency as $St = \omega/2\pi$.
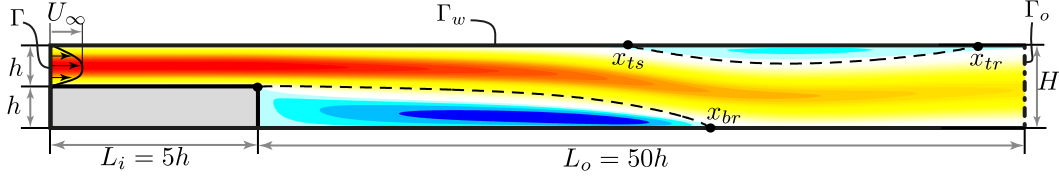
Figure 5.1 – Sketch of the flow configuration superimposed onto the velocity field x-direction of the base flow for the backward facing step at $Re = 500$. The flow presents two recirculation bubbles, one at the top and one at the bottom.

The flow is governed by the two-dimensional incompressible Navier-Stokes equations (NSE),

$$\left.\begin{aligned} \nabla \cdot \boldsymbol{u} &= 0, \\ \partial_t \boldsymbol{u} + \mathcal{N}(\boldsymbol{u}) &= 0, \\ \boldsymbol{u} = \boldsymbol{u}_{pois} + \boldsymbol{f} \text{ on } \Gamma \text{ , } \boldsymbol{u} &= 0 \text{ on } \Gamma_w \end{aligned}\right\} \tag{5.1}$$

where

$$\mathcal{N}(\boldsymbol{u}) \equiv (\boldsymbol{u} \cdot \nabla)\boldsymbol{u} + \nabla p - Re^{-1}\Delta\boldsymbol{u} \tag{5.2}$$

corresponds to the advective, pressure gradient and diffusive terms. The pressure field p is enforced by the incompressibility condition entailing divergence free velocity fields $\nabla \cdot \boldsymbol{u} = 0$, for the seek of simplicity we will not write it explicitly in the following.

The Navier-Stokes equations are solved using the Finite Element Method with the flow fields (u_x, u_y, p) spatially discretised by Taylor- Hood (P2,P2,P1) elements. The software FreeFEM++ is used to generate the domain Ω triangulation and to build all the required operators. The steady solutions of the nonlinear systems of NSE are computed using the Newton-Raphson method, while the time varying DNS (Direct Numerical Simulations) of the NSE are integrated using a second order Characteristics-Galerking method. Further details on the numerical approach can be found in Mantič-Lugo & Gallaire (2015).

5.2.2 Linear transfer function

The steady solution of NSE defines the base flow $\boldsymbol{U}_B$,

$$\mathcal{N}(\boldsymbol{U}_B) = 0, \tag{5.3}$$

illustrated in Fig. 5.1 for the backward-facing step at $Re = 500$. The two-dimensional backward-facing step is linearly stable due to the convective nature of the shear layer. For an expansion ratio $\Xi = 0.5$, the first unstable mode appears in three-dimensions at $Re_{cr} \sim 748$ (Barkley *et al.* (2002); Lanzerstorfer & Kuhlmann (2012)). First we chose Re = 500 relating to the past works by Boujo & Gallaire (2015); Blackburn *et al.* (2008); Barkley *et al.* (2002); Marquet & Sipp (2010).

Assuming a small amplitude of the forcing, the exact nonlinear response can be approximated by its linear response

$$\left.\begin{array}{l} \left[\partial_t \boldsymbol{u}'_{1B} + \mathscr{L}_{\boldsymbol{U}_B}(\boldsymbol{u}'_{1B})\right] = 0, \\ \boldsymbol{u}'_{1B} = \boldsymbol{f} \text{ on } \Gamma \,, \, \boldsymbol{u}'_{1B} = 0 \text{ on } \Gamma_w \end{array}\right\} \tag{5.4}$$

where higher order nonlinear terms are neglected, and the operator $\mathscr{L}_{\boldsymbol{U}}(\boldsymbol{u}')$ is the corresponding operator for the NSE linearized around $\boldsymbol{U}$, i.e.

$$\mathscr{L}_{\boldsymbol{U}}(\boldsymbol{u}') \equiv (\boldsymbol{U} \cdot \nabla)\boldsymbol{u}' + (\boldsymbol{u}' \cdot \nabla)\boldsymbol{U} + \nabla p' - Re^{-1}\Delta \boldsymbol{u}', \tag{5.5}$$

The focus of the study is on the response to stochastic forcing, we however first describe the harmonic response to help understanding and be able to predict in which frequency range larger amplifications are more likely to be observed, see for example Schmid & Henningson (2001); Farrell & Ioannou (1996); Dergham *et al.* (2013); Boujo & Gallaire (2015); Mantič-Lugo & Gallaire (2015). For a harmonic forcing $\boldsymbol{f}(y, t) = \boldsymbol{f}_1(y)e^{i\omega t} + cc.$ with a spatial distribution $\boldsymbol{f}_1(y)$ and frequency $St = \omega/(2\pi)$ the corresponding linear response $\boldsymbol{u}'(x, t)$ is also harmonic $\boldsymbol{u}'(x, t) \simeq \boldsymbol{u}'_{1B}(x, t) = \boldsymbol{u}_{1B}(x)e^{i\omega t} + cc.$ and oscillates at the forcing frequency, due to the linearity of the operator (5.4). The linear equation (5.4) can be rewritten formally as $\boldsymbol{u}_{1B} = \mathscr{R}_B(\omega)\boldsymbol{f}_1$ where $\mathscr{R}(\omega) = (i\omega\mathscr{I} + \mathscr{L}_{\boldsymbol{U}})^{-1}$ is the resolvent operator for any steady $\boldsymbol{U}$ and $\mathscr{R}_B(\omega) = (i\omega\mathscr{I} + \mathscr{L}_{\boldsymbol{U}_B})^{-1}$ is the resolvent operator for the base flow.

A natural way of measuring the amplification of the nonlinear dynamical system is the gain, which is defined as the ratio between the amplitude of the output response and the amplitude of the input forcing, and is related to the ratio of the energy of the output response to the energy of the input forcing. For the specific linear case of harmonic forcing it reads

$$G_B(\omega) = \frac{\|\boldsymbol{u}_{1B}\|_\Omega}{\|\boldsymbol{f}_1\|_\Gamma} = \frac{\|\mathscr{R}_B(\omega)\boldsymbol{f}_1\|_\Omega}{\|\boldsymbol{f}_1\|_\Gamma}, \tag{5.6}$$

where the L^2 norm $\|.\|$ is determined by the Hermitian inner product $(\boldsymbol{a}|\boldsymbol{b}) = \int_\Omega \overline{\boldsymbol{a}} \cdot \boldsymbol{b} d\Omega = \int_\Omega \boldsymbol{a}^H \cdot \boldsymbol{b} d\Omega$, for complex fields in the domain Ω, with straightforward restriction on the boundary Γ.

The linear gain $G_B(\omega)$ around the base flow is function of the forcing frequency ω, as illustrated in Fig. 5.2(a), where the gain $G_B(\omega)$ describes a bell-shaped curve with a maximum at $St_{opt} = \omega_{opt}/2\pi = 0.075$. Furthermore, not only the amplitude of the response depends on the forcing frequency ω but also the shape of the response as shown in the velocity contours presented in Fig. 5.2(b) for the response to a forcing in the form of a Poiseuille profile $\boldsymbol{f}_1 = y(1 - y)$. The structure of the response presents a correlation between the wave number and the frequency and shows how the response structures migrates downstream for larger gains. The linear response to white noise forcing would correspond to a combination of all the different response structures multiplied by their corresponding amplitudes since a pure white noise forces all the frequencies with the same energy.
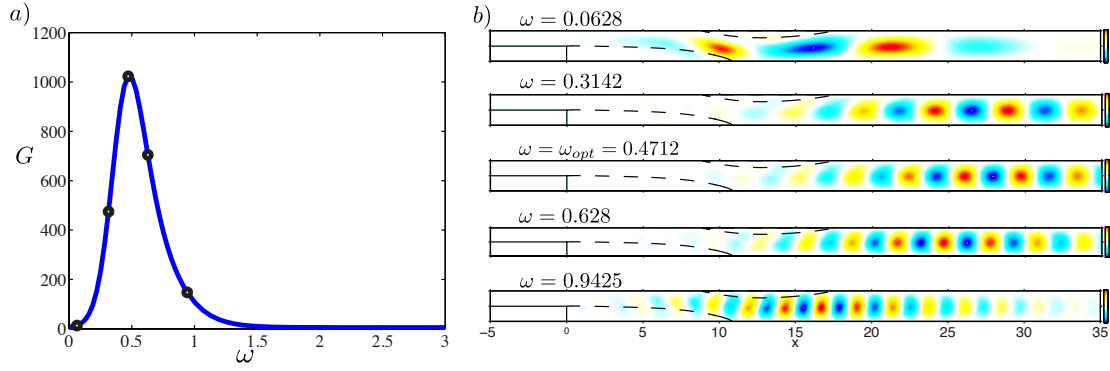
Figure 5.2 – (a) Linear gain $G_B(\omega)$ around the base flow and (b) contours of the velocity in y-direction of the linear response as function of the forcing frequency $St = \omega/2\pi$ for a harmonic forcing of the form of a Poiseuille profile $\boldsymbol{f}_1 = y(1-y)$. The maximal gain is attained at the optimal frequency $St = \omega_{opt}/(2\pi) = 0.075$. Plots for the backward facing step at $Re = 500$.

5.3 Temporal stochastic forcing

5.3.1 Forcing definition and white noise response

In more realistic cases the external disturbances are more likely characterized by a broadband frequency rather than being harmonic. Thereby, to model this physical perturbations we excite the flow by a random noise, characterised by its statistical properties. Nonetheless, there are advantages in addressing the study of the response to stochastic forcing in the frequency domain as described in Farrell & Ioannou (1996); Dergham *et al.* (2013) and whose concepts will be used herein. The power spectral density function (PSD) characterises the energy distribution of the input signal in the frequency domain. With the aid of a truncated Fourier transform for a time signal $x(t)$ of length $[0, T]$,

$$\hat{x}_T(\omega) = \frac{1}{\sqrt{T}} \int_0^T x(t) e^{-i\omega t} dt \qquad (5.7)$$

the PSD is defined as

$$S_{xx}(\omega) = |\hat{x}_T(\omega)|, \qquad (5.8)$$

and in the limit $T \to \infty$ the PSD converges to the expected value of $\hat{x}(\omega)$, $\lim_{T \to \infty} S_{xx}(\omega) = \mathscr{E}(|\hat{x}_T(\omega)|^2)$. In general, a white noise signal $\xi(t)$ is δ-correlated $\langle \xi(t)\xi^\dagger(s) \rangle = \delta(t-s)$ and defined by a constant PSD $S_{\xi\xi}(\omega) = |\hat{\xi}|^2 = S$ with infinite power P. Indeed, the power is defined as

$$P = \lim_{T \to \infty} \frac{1}{T} \int_0^T |\xi_T(t)|^2 dt = \frac{1}{\pi} \int_0^\infty |\hat{\xi}|^2 d\omega = \sigma^2 \qquad (5.9)$$

thanks to the Parseval's theorem and to the definition of the variance σ. Because $S > 0$, a pure white noise has infinite power and is not physically realisable being an idealisation of physical

noises. Physical systems usually are band-limited and are affected by the noise within this band.

A digital random signal $\xi_d(t)$ has a natural band limiting frequency given by its time step, $\omega_d/(2\pi) = 1/2\delta t$. In order to obtain time step independent results, the signal is filtered to a band limiting frequency ω_b yielding a power and variance $P_b = \sigma_b^2 = |\hat{\xi}_b|^2 \omega_b/\pi$. Fig. 5.3(a) compares a realisation of the white noise signal with unit variance and power, without filtering and filtered with a band limiting frequency $\omega_b/2\pi = 1$, while Fig. 5.3(b) compares the PSD for the actual signals and their theoretical value. The PSD is estimated using a Welch method in matlab.
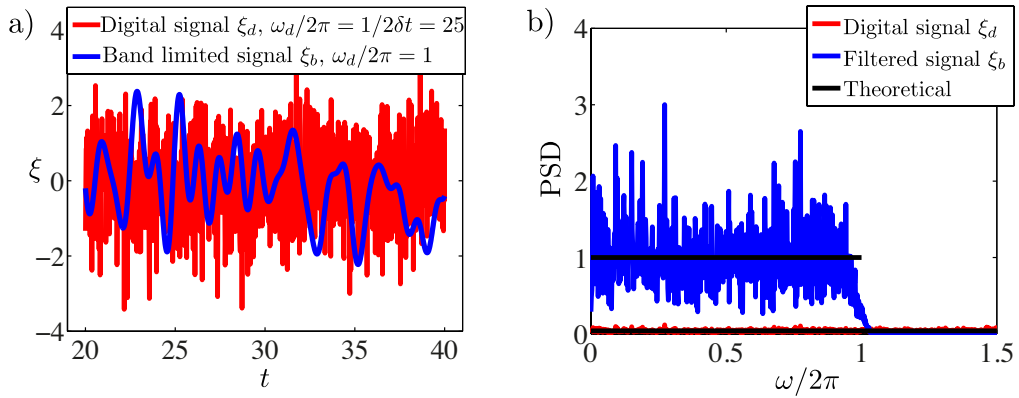
Figure 5.3 – (a) Realisation of white noise signal with unit power $P = 1$ comparing a signal without filtering $\omega_b/2\pi = 1/(2\delta t) = 25$ and filtered with a band limiting frequency $\omega_b/2\pi = 1$. (b) Comparison of the power spectral density for these two signals.

The inlet forcing used in the study is defined as $\boldsymbol{f} = A\boldsymbol{f}_1(y)\xi_b(t)$, stochastic in time by the function $\xi_b(t)$, a band limited white noise, δ-correlated with zero mean, and unit power and variance $\sigma = 1$, with constant PSD $2|\hat{\xi}_b|^2 = 2\pi/\omega_b$ that depends only on the band imitating frequency. For the sake of simplicity we start with a fixed spatial distribution in the form of a Poiseuille profile $\boldsymbol{f}_1(y) = \sqrt{30}y(1-y)$, such that $\int_\Gamma \boldsymbol{f}_1(y)^2 d\Gamma = 1$ and A is the amplitude of the forcing. Defining $\langle\cdot\rangle = \frac{1}{T}\int_0^T \cdot dt$ as the time average over a time span T long enough to achieve T independent results, the power of the forcing relates to its amplitude as

$$\langle\int_\Gamma \boldsymbol{f}^2 d\Gamma\rangle = \frac{1}{\pi}\int_0^{\omega_b} \|\hat{\boldsymbol{f}}\|_\Gamma^2 d\omega = \frac{1}{\pi}\int_0^{\omega_b} \|\boldsymbol{f}_1\|_\Gamma^2 |\hat{\xi}_b|^2 A^2 d\omega = A^2. \tag{5.10}$$

The amplitude of the response or variance is defined in general as

$$B^2 = \langle\int_\Omega \boldsymbol{u}'^2 d\Omega\rangle = \frac{1}{\pi}\int_0^{\omega_b} \|\hat{\boldsymbol{u}}\|_\Omega^2 d\omega = \frac{1}{\pi}\int_0^{\omega_b} G^2(\omega)\|\hat{\boldsymbol{f}}\|_\Gamma^2 d\omega, \tag{5.11}$$

where $\boldsymbol{u}'$ is the pure fluctuating velocity with zero mean $\langle\boldsymbol{u}'\rangle = 0$, $G(\omega)$ is the gain at each frequency, and B can be interpreted as the amplitude of the response.
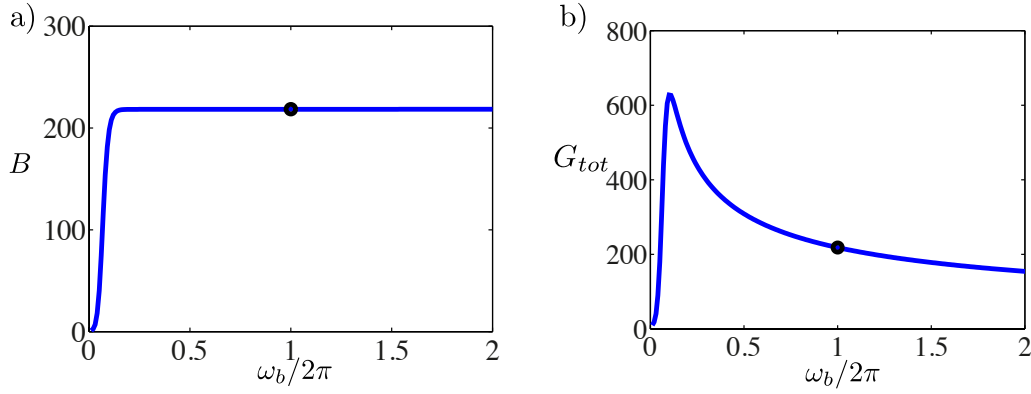
Figure 5.4 – (a) Amplitude of the linear response B and (b) total linear Gain G_{tot} as function of the band limiting frequency ω_b for a band limited white noise with constant PSD $2|\hat{\xi}_b(\omega)|^2 = 1$ and varying power $P(\omega_b)$ (5.9), where the spatial distribution is in the form of a Poiseuille profile $\boldsymbol{f}_1 = y(1-y)$. The response amplitude and total gain are computed from the integration of the linear gain $G_B(\omega)$ around the base flow for the backward facing step at $Re = 500$.

For the sake of clarity we describe a complementary view, which consists in fixing the PSD of the white noise forcing $2|\hat{\xi}_b|^2 = S = cst.$, and thus allowing the power $P(\omega_b)$ to vary with the band limiting frequency ω_b (5.9). In this setting, the amplitude and variance of the linear response B tends asymptotically to a constant value for the infinite limit of the band frequency $\omega_b \to \infty$, as shown in Fig. 5.4(a), and thus yielding infinite power P. This asymptotic behaviour to a constant limit follows from the gain curve $G(\omega)$ which tends to zero $\lim_{\omega \to \infty} G(\omega) = 0$ as described by Farrell & Ioannou (1996) and illustrated in Fig. 5.2, where large amplifications are only concentrated at low frequencies ω. It should be highlighted that this behaviour persists also in nonlinear systems, which can be described by a nonlinear gain, since in general, physical systems damp high frequencies. The study and modelling of the response of dynamical systems under white noise forcing is standard in literature due to its generality, e.g. Farrell & Ioannou (1996, 1993, 2012); Dergham *et al.* (2013) among others. The asymptotic response to pure white noise forcing $\omega_b \to \infty$ can be accurately approximated by means of a more physical forcing with a band limited white noise, providing that the band limiting frequency ω_b is far enough from the low frequency amplification (Fig. 5.2), as for $\omega_b/(2\pi) = 1$ that will be used in all the following calculations.

The total nonlinear gain for the stochastically forced system reads as the ratio between the amplitude of the response and the amplitude of the forcing, which is related to the ratio of the power of the fluctuating response $\boldsymbol{u}'$ to the power of the forcing $\boldsymbol{f}$,

$$G_{tot}^2 = \frac{\langle \int_\Omega \boldsymbol{u}'^2 d\Omega \rangle}{\langle \int_\Gamma \boldsymbol{f}^2 d\Gamma \rangle} = \frac{1}{\omega_b} \int_0^{\omega_b} G^2(\omega) d\omega. \tag{5.12}$$

The total gain tends to zero $\lim_{\omega_b \to \infty} G_{tot} = 0$ for the limiting case of white noise as illustrated in Fig. 5.4(b), since an increase of the band limiting frequency ω_b entails an increase in the power spent at higher frequencies which have small amplification $G(\omega)$ (see Fig. 5.2) and do

not contribute to the power of the response B^2, while spending power in the forcing A^2.

The backward-facing step presents a strong linear amplification of the forcing due to the non-normality of the linear operator $\mathscr{L}_{\boldsymbol{U}_B}$ (Marquet & Sipp (2010); Boujo & Gallaire (2015); Mantič-Lugo & Gallaire (2015)) as can be seen also in Fig. 5.2. This strong amplification limits the validity of the linear response to very small amplitude of the forcing. Thereby, one would expect a saturation mechanism to occur with an increase of the forcing amplitude, restraining the amplitude of the response. This nonlinear saturation of the flow under stochastic forcing calculated running DNS can be appreciated in Fig. 5.5, where the total nonlinear gain G_{tot} strongly reduces as the amplitude of the forcing A increases. Along with the amplitude saturation, the response exhibits a change in structure with a migration upstream corresponding to an increase in the forcing amplitude. This migration is connected to a shortening of the mean
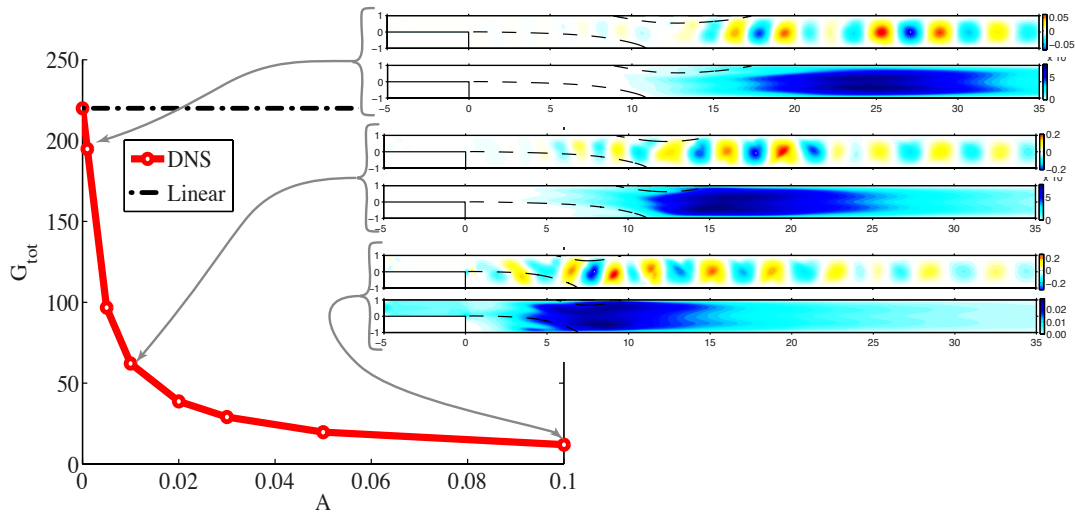
Figure 5.5 – Nonlinear total gain from DNS G_{tot} and linear total gain G_{Btot} as function of the amplitude of the forcing A. The figure shows the saturation in the gain and the variation of the response structure. The insets show the perturbation velocity in y-direction and the perturbation energy. $Re = 500$.

recirculation bubble, which is reminiscent of a similar tendency associated to a reduction of instability in the cylinder flow as described in Zielinska *et al.* (1997).

5.3.2 Self-consistent model for a temporal stochastic forcing

Saturation problems of similar nature as illustrated in Fig. 5.5 have been modelled by means of a coupled system of mean flow and linear fluctuation equations in Mantič-Lugo & Gallaire (2015) for the case of the response to harmonic forcing, and in Mantič-Lugo *et al.* (2014, 2015) for an unstable flow. Another related approach is undertaken in the SSST introduced by Farrell & Ioannou (2012) where also the slowly varying ensemble averaged mean flow, rather than a time average mean flow, is coupled to a linear response to white noise. Following the use of averaged flows in the described works we introduce the Reynolds decomposition $\boldsymbol{u}(\boldsymbol{x}, t) =$

$\boldsymbol{U}(\boldsymbol{x}) + \boldsymbol{u}'(\boldsymbol{x}, t) = \boldsymbol{U}_B(\boldsymbol{x}) + \Delta \boldsymbol{U}(\boldsymbol{x}) + \boldsymbol{u}'(\boldsymbol{x}, t)$. The instantaneous flow is expressed as a mean flow $\boldsymbol{U} = \langle \boldsymbol{u} \rangle$ plus a pure fluctuation $\boldsymbol{u}'$ with zero mean $\langle \boldsymbol{u}' \rangle = 0$ and where $\Delta \boldsymbol{U}$ corresponds to the base flow modification. Inserting the Reynolds decomposition in the full NSE we obtain a set of two coupled equations,

$$\left.\begin{aligned} \mathcal{N}(\boldsymbol{U}) &= -\langle (\boldsymbol{u}' \cdot \nabla) \boldsymbol{u}' \rangle \\ \boldsymbol{U} &= \boldsymbol{u}_{pois} \text{ on } \Gamma \, , \, \boldsymbol{U} = 0 \text{ on } \Gamma_w \end{aligned}\right\} \tag{5.13a}$$

$$\left.\begin{aligned} \partial_t \boldsymbol{u}' + \mathcal{L}_{\boldsymbol{U}}(\boldsymbol{u}') &= -(\boldsymbol{u}' \cdot \nabla) \boldsymbol{u}' + \langle (\boldsymbol{u}' \cdot \nabla) \boldsymbol{u}' \rangle \\ \boldsymbol{u}' &= \boldsymbol{f} \text{ on } \Gamma \, , \, \boldsymbol{u}' = 0 \text{ on } \Gamma_w \end{aligned}\right\} \tag{5.13b}$$

the mean flow $\boldsymbol{U}$ arises as a result of the steady mean flow equation (5.13a), while the forced response equation (5.13b) governs the time dependent fluctuating field $\boldsymbol{u}'$. Note that no simplification has been carried out so far.

The asymptotic analysis described in Mantič-Lugo & Gallaire (2015) for the backward-facing step suggests that the nonlinear interaction of the fluctuation with itself gathered in the term $-(\boldsymbol{u}' \cdot \nabla) \boldsymbol{u}' + \langle (\boldsymbol{u}' \cdot \nabla) \boldsymbol{u}' \rangle$ has a negligible influence in the saturation process. Thereby, this nonlinear interaction is dropped in the self-consistent model while keeping the nonlinearity gathered in the Reynolds stress, since the studies by Mantič-Lugo *et al.* (2014, 2015); Mantič-Lugo & Gallaire (2015) propose the Reynolds stress as the main nonlinear term required for the flow saturation. Furthermore, this idea is supported by the results obtained using SSST of Farrell & Ioannou (2012) and in Beaume *et al.* (2015), where the fluctuation equation (5.13b) is also approximated as linear while keeping the nonlinear Reynolds stress term.

The time varying fluctuation $\boldsymbol{u}'$ of the coupled system (5.13) is rewritten in the frequency domain using (5.7) and (5.9) for a band limiting frequency ω_b. The incompressibility of the velocity field allows to rewrite the Reynolds stress as $(\boldsymbol{u} \cdot \nabla) \boldsymbol{u} = \nabla \cdot (\boldsymbol{u} \otimes \boldsymbol{u})$. Therefore, the total Reynolds stress forcing that modifies the mean flow equation (5.13a) is composed by the frequency integral of the independent Reynolds stress forcings $2\Re \left((\bar{\hat{\boldsymbol{u}}} \cdot \nabla) \hat{\boldsymbol{u}} \right)$ build by the response at each frequency ω, in the same fashion as the amplitude of the response (5.11). The cross terms between different frequencies disappear in the Reynolds stress forcing thanks to the orthogonality of the frequency basis. Hence, the self-consistent system is formalised neglecting the nonlinear interaction of the fluctuation with itself, RHS in (5.13b),

$$\left.\begin{aligned} \mathcal{N}(\boldsymbol{U}) &= -\frac{1}{\pi} \int_0^{\omega_b} 2\Re \left((\bar{\hat{\boldsymbol{u}}} \cdot \nabla) \hat{\boldsymbol{u}} \right) d\omega \\ \boldsymbol{U} &= \boldsymbol{u}_{pois} \text{ on } \Gamma \, , \, \boldsymbol{U} = 0 \text{ on } \Gamma_w \end{aligned}\right\} \tag{5.14a}$$

$$\left.\begin{aligned} i\omega \hat{\boldsymbol{u}} + \mathcal{L}_{\boldsymbol{U}}(\hat{\boldsymbol{u}}) &= 0 \\ \hat{\boldsymbol{u}} &= \hat{\boldsymbol{f}} \text{ on } \Gamma \, , \, \hat{\boldsymbol{u}} = 0 \text{ on } \Gamma_w \end{aligned}\right\} \tag{5.14b}$$

It is composed by a set of independent linear equations (5.14b) that describe the response to noise at each frequency ω coupled to the mean flow equation (5.14a) by means of the Reynolds stress forcing.

The integral in the frequency domain of the Reynolds stress forcing and the total response is approximated by a discrete integral in a given set of discrete frequencies ω_i, thus the Reynolds stress forcing is rewritten as

$$\frac{1}{\pi} \int_0^{\omega_b} 2\Re\left((\bar{\bar{\boldsymbol{u}}} \cdot \nabla)\hat{\boldsymbol{u}}\right) d\omega \simeq 2 \sum_{i=1}^{n_f} \alpha_i 2\Re\left((\bar{\bar{\boldsymbol{u}}}_i \cdot \nabla)\hat{\boldsymbol{u}}_i\right), \tag{5.15}$$

and the amplitude of the response,

$$B^2 = \left\langle \int_\Gamma \boldsymbol{u}'^2 d\Gamma \right\rangle \simeq 2 \sum_{i=1}^{n_f} \alpha_i \|\hat{\boldsymbol{u}}_i\|_\Omega^2 = \frac{2\pi}{\omega_b} \sum_{i=1}^{n_f} \alpha_i G^2(\omega_i)\, A^2, \tag{5.16}$$

where α_i denote appropriate quadrature coefficients, n_f represents the number of discrete frequencies and A is the forcing amplitude previously defined in (5.10). The total nonlinear response is then approximated as

$$\boldsymbol{u}' \simeq \sum_{i=1}^{n_f} \sqrt{\alpha_i}(\hat{\boldsymbol{u}}_i e^{i(\omega t + \phi_i)} + cc.), \tag{5.17}$$

where ϕ_i is an unknown phase that is not obtained from the truncated Fourier transform of the random noise.

In order to minimise the number n_f of discrete frequencies and well enough approximate the response (5.16) we have to select appropriately the discrete frequencies ω_i and weights α_i, since the gain $G(\omega_i)$ varies strongly with the frequency (Fig. 5.2). Therefore, we rewrite the nonlinear gain as

$$G_{tot}^2 = \int_0^{\omega_b} G_B^2(\omega)\left(\frac{G^2(\omega)}{G_B^2(\omega)}\right) d\omega \simeq \frac{2\pi}{\omega_b} \sum_{i=1}^{n_f} \gamma_i \frac{G^2(\omega_i)}{G_B^2(\omega_i)}, \tag{5.18}$$

and use a weighted Gaussian quadrature rule for $\left(\frac{G^2(\omega)}{G_B^2(\omega)}\right)$ with weight function $G_B^2(\omega)$ (Press *et al.* (2007)). For a given frequency integration interval, this yields optimal quadrature coefficients γ_i and abscissas ω_i, from which the α_i in (5.15)- (5.16) are easily deduced $\alpha_i = \gamma_i/G_B^2(\omega_i)$. This formulation provides a fast convergence rate when $(G^2(\omega)/G_B^2(\omega))$ is close to a constant, in other words when the saturated gain around the mean flow $G(\omega)$ has a similar shape as the linear gain round the base flow $G_B(\omega)$.

The Reynolds stress forcing is built by the response structures $\hat{\boldsymbol{u}}_i$ multiplied by their corresponding gains $G(\omega_i)$. This approximation strongly depends on the selected discrete frequencies ω_i, since there is a strong variation in the gain $G(\omega_i)$ and response structure $\hat{\boldsymbol{u}}_i$ with the frequency, as illustrated clearly in Fig. 5.2 for the linear case. The frequencies should therefore be selected clustered around optimal gain $\omega_{opt}/2\pi = 0.075$ while spread enough to ensure a rich family of response structures $\hat{\boldsymbol{u}}_i$ from which the Reynolds stress forcing is calculated. This optimal distribution is achieved by selecting the optimal frequency as the endpoint for a Gauss-Radau quadrature rule which is applied to the two intervals that appear at the right

and left side of the optimal frequency. Referring in anticipation to Fig. 5.7(b) and looking only at the evolution of the overall gain G_{tot} with n_f (squares), we see that this scheme converges very quickly, achieving convergence for a very small number of discrete frequencies $n_f \simeq 15$.

It should be highlighted that the coupled system has to be solved iteratively, in order to obtain the correct mean flow $\boldsymbol{U}$ and responses $\boldsymbol{u}_i$ for a given forcing $\boldsymbol{f}$ that couples the system. The details on the procedure undertaken to solve the self-consistent system (5.14) can be encountered in Mantič-Lugo & Gallaire (2015) for a system with harmonic forcing. The unique difference with the present case is that the linear responses at each frequency have to be computed together to obtain the total Reynolds stress forcing in (5.14a). Nevertheless, note that the process is parallelizable since all the linear equations are decoupled and are computed independently, implying that the computational time is mainly independent on n_f provided a correct parallelisation.

The introduced approximation scheme (5.18) can be pushed to the limit $n_f = 1$ by approximating the nonlinear gain $G(\omega)$ just with a single abscissa point at ω_{opt}. In this case, the nonlinear gain $G(\omega)$ at the rest of frequencies is obtained from the weighting function $G_B(\omega)$ (see Fig. 5.2) scaled with the saturated gain around the mean flow $G(\omega_{opt})$ forcing at the optimal frequency ω_{opt}: $G^2(\omega) \sim \kappa G_B^2(\omega)$ with $\kappa = G^2(\omega_{opt})/G_B^2(\omega_{opt})$.

The system (5.14) models the nonlinear behaviour of the flow as response to stochastic forcing. It emerge as an extension of the SC model presented in Mantič-Lugo & Gallaire (2015) for harmonic forcing. It is the forced counterpart of the self-consistent model introduced first for unstable flows (Mantič-Lugo *et al.* (2014, 2015)) where the linear equation corresponds to an eigenvalue problem and the amplitude is dictated by the criterion of marginally stable with eignemode $\sigma = 0$.

5.3.3 Results: dynamics of the flow subject to temporal stochastic forcing

Applying the SC model to the backward-facing step with increasing forcing amplitude A, the model is able to capture the saturation behaviour with a remarkably accurate prediction of the gain variation as illustrated in Fig. 5.6(a) and response amplitude Fig. 5.6(b), where the DNS results are compared to the SC model. Note how the SC model with a frequency integrated Reynolds stress exhibits a slightly better prediction when compared to the SC model with the unique frequency ω_{opt} approximation of the Reynolds stress forcing, mainly due to the more restrictive construction of the latter with the information from the response field solely at the optimal frequencies. These results suggest that the findings obtained for harmonic forcing in Mantič-Lugo & Gallaire (2015) extrapolate to white noise forcing. Thereby, Fig. 5.6 confirms a picture where the mean flow modification due to the nonlinear forcing of the Reynolds stress is crucial to capture the energy saturation for the flow under white noise forcing. In other words, a larger forcing entails a larger response, which in turn generates stronger Reynolds stresses that force and modify the mean flow, shortening the recirculation bubble see Fig. 5.2 and enforcing a saturation, which reduces the response in comparison to its linear prediction.
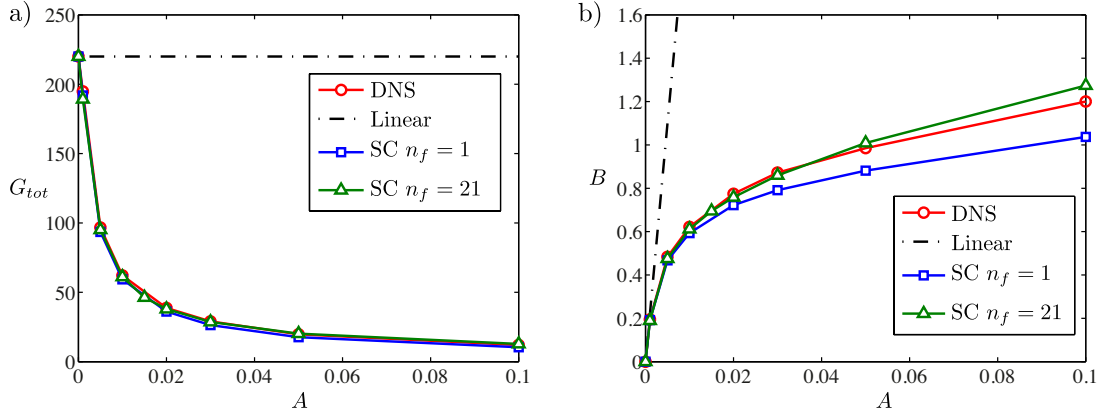
Figure 5.6 – (a) Gain and (b) response as function of the forcing amplitude A of the band limited white noise for the DNS (circles), SC model with $n_f = 21$ (triangles), SC model with $n_f = 1$ at ω_{opt} (squares) and the linear estimation (dash dotted line). $Re = 500$.

Additionally, the nonlinear interaction of the response fluctuation with itself gathered in the term $-(\boldsymbol{u}' \cdot \nabla)\boldsymbol{u}' + \langle (\boldsymbol{u}' \cdot \nabla)\boldsymbol{u}' \rangle$ does not seem to play a relevant role in the saturation and can be neglected as assumed in the SC model.

Restricting our attention to a saturated case for a forcing amplitude $A = 0.1$, Fig. 5.7(a) depicts the gain as a function of frequency for the DNS and SC model. The SC model integral in frequency with $n_f = 21$ and $n_f = 9$ marked with squares and circles show an acceptable prediction of the exact DNS gain distribution marked as continuous thick line, presenting a peaked optimal very close to the DNS optimal frequency but slightly smaller and differing only at very low frequencies. The exact DNS gain distribution is computed from a PSD of the time varying simulation at different points and then integrated over the whole domain Ω at each frequency ω. While, in the cylinder wake case, a linear stability analysis around the mean flow describes well the dynamics of the flow with an accurate estimation of the frequency and structure of the fluctuations (Barkley (2006)). In the present case, the linear response computed around the DNS mean flow (thin solid line) under-predicts the amplitude and gain of the exact DNS and the SC model, yielding a lower total gain $G_{tot} = 9.7$ which differs from the exact DNS $G_{tot} = 12$. This discrepancy could be interpreted by the lack of coupling between the mean flow and perturbation equation in the linear response suggesting that the Reynolds stress coupling is essential for a correct estimation of the saturation dynamics.

The gain distribution of the base flow scaled by the gain at the optimal frequency of the SC model at $G(\omega_{opt})$ (thick dashed line) does not approximate well the exact DNS distribution, although it is used to weight the response and the Reynolds stress (5.18) and estimates correctly the saturation (Fig. 5.7) with an integral in frequency $G_{tot} = 10.3$ rather close to the exact DNS one. One of the reasons why a single frequency approximation of the response captures the nonlinear saturation in terms of its energy is because the optimal frequency of the linear gain and the saturated gain do not differ markedly.
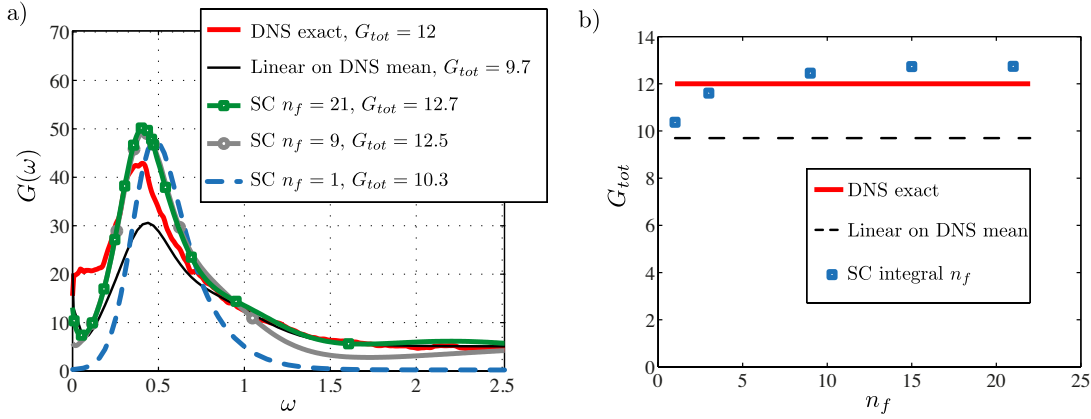
Figure 5.7 – (a) Gain distribution function of the frequency and total gain values for the DNS and SC model saturated with a forcing amplitude $A = 0.1$. The exact DNS total gain is $G_{tot} = 12$ (thick solid line) and $G_{tot} = 9.7$ for the linear prediction around the DNS mean flow (thin solid line). The SC model integrated in frequency has a total gain $G_{tot} = 12.7$ (squares) for $n_f = 21$, $G_{tot} = 12.5$ for $n_f = 9$ (circles) and $G_{tot} = 10.3$ (thick dashed line). (b) Total gain of the exact DNS (solid line), linear response aroun the DNS mean flow (dashed line) and SC model as function of the number of discrete frequencies ω_i given by n_f for the base flow and saturated mean flow with a forcing amplitude $A = 0.1$. $Re = 500$.

The nonlinear total gain is reminiscent of the idea of nonlinear transfer function, with a gain at each frequency $G(\omega)$ that depends on the amplitude of the forcing and the frequency. The concepts of nonlinear transfer function and nonlinear gain are well described in Noiray *et al.* (2008) dealing with the study of nonlinear stability of flames in burners.

Fig. 5.7(b) presents the variation of the total gain of the self-consistent model with different number n_f of discrete frequencies ω_i showing a clear decrease in accuracy with a decrease in the number of points n_f. It shows that n_f as small as 9 is enough to obtain an accurate estimation of the total gain.

The local kinetic energy of the response fluctuation and the velocity in the x-direction for the DNS and the SC model are compared in Fig. 5.8. The energy distribution of the SC model approximates acceptably the exact DNS capturing most of the upstream migration when compared to the linear response structure around the base flow Fig. 5.2. Nonetheless, the SC model exhibits a more elongated structure compared to the compact DNS energy distribution between the two recirculation bubbles. As one could expect the SC model with only single frequency approximation of the response, depicted in Fig. 5.8(c), presents a poorer approximation than its frequency integrated counterpart (Fig. 5.8(b)).

The DNS snapshot of the fluctuating velocity $\boldsymbol{u}'_x$ shows in Fig. 5.8(d) a very clear streamwise wave length. This means that in spite of a response composed by a mix of streamwise wavelengths excited at all frequencies (Fig. 5.2) inside the band ω_b, there is a clear selective process governed by the gain curve Fig. 5.7(a) promoting strongly the optimal frequency and its re-
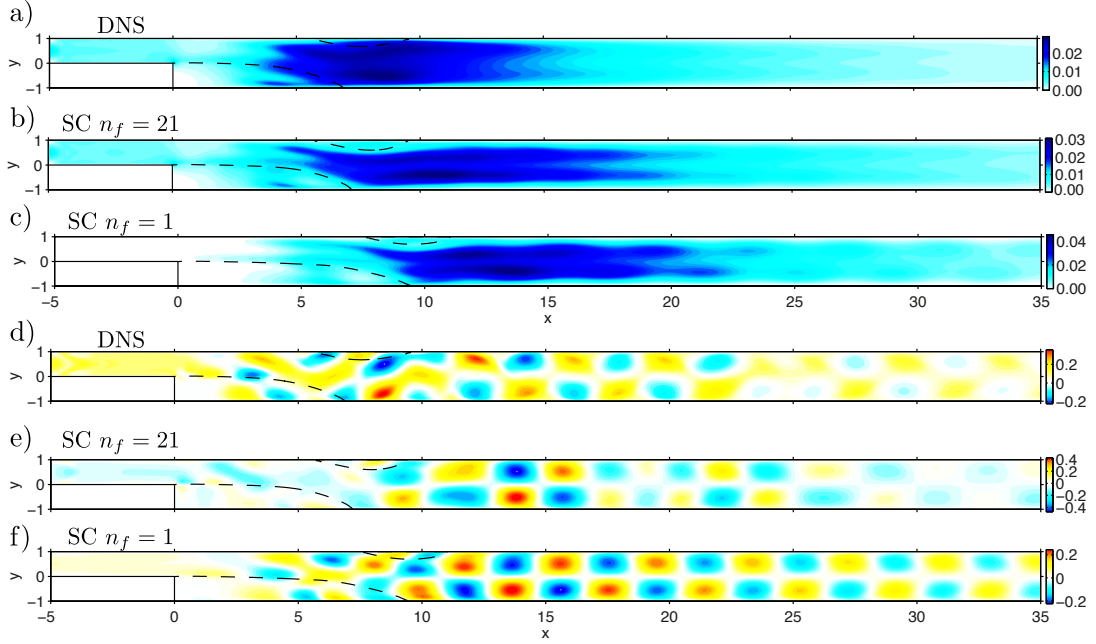
Figure 5.8 – Energy distribution of the response fluctuation for (a) DNS, (b) SC with $n_f = 21$ and (c) SC with single frequency approximation ω_{opt}. Fluctuation velocity in the x-direction, u'_x (d) DNS snapshot, (e) SC with $n_f = 21$ constructed with arbitrary ϕ_i in (5.17) and (f) SC with $n_f = 1$, single frequency approximation at ω_{opt}. Forcing amplitude $A = 0.1$ and $Re = 500$.

sponse structure. This selective process is well captured by the SC model results specially by the optimal frequency approximation Fig. 5.8(e) that approximates well the streamwise wave length when compared to the DNS snapshot Fig. 5.8(d).

A more quantitative comparison is gathered in Fig. 5.9 where the recirculation bubble lengths are compared for the DNS and SC model as function of the forcing amplitude. The SC model integrated in frequency (circles) predicts accurately the bubble positions, for the top as much as for the bottom, even capturing very closely the non-monotonous trend of the bubble at the bottom. This is of great relevance because it implies that the SC model is able to characterize properly the flow where linear estimations around the base flow would fail. The SC model with optimal frequency approximation (triangles) also follows the migration of the bubbles of the DNS solution (squares) although not as closely as the integrated form mainly describing the non-monotonous behaviour. This difference appears probably due to the restricted construction of the Reynolds stress forcing by only the optimal response structure.

The migration upstream of the response with an increase of the amplitude of the forcing illustrated in Fig. 5.5 is described in a quantitative form by the position of the maximum x_{Emax} of the fluctuation energy and plotted in Fig. 5.10(a). Although the SC model estimates very closely the trend of the DNS response migration, there is a constant difference of $\delta x_{Emax} \sim 3h$, which is slightly larger for the single frequency approximation (triangles) and is in line with the results shown in Fig. 5.8. It should be noted that the SC model is able to describe
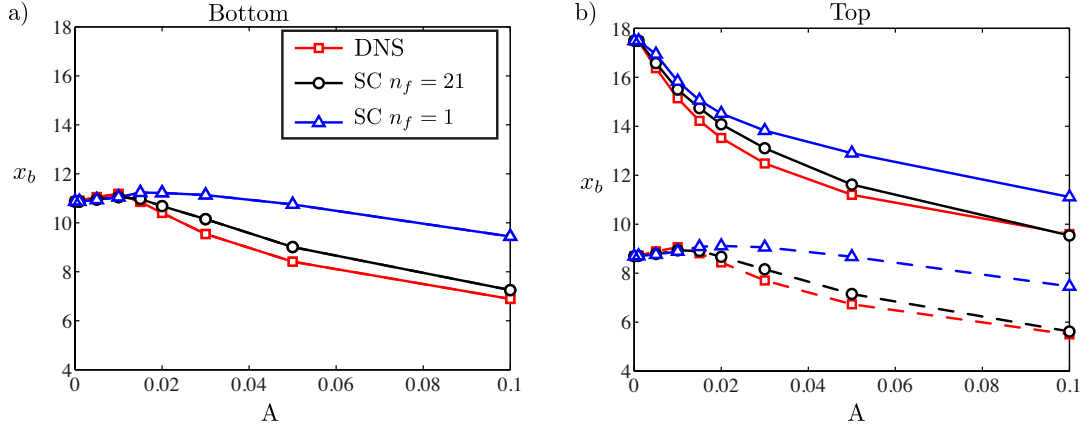
Figure 5.9 – Position of the recirculation bubbles (a) bottom and (b) top for the DNS (squares), SC integrated in frequency (circles) and SC with optimal frequency approximation (triangles) as function of the forcing amplitude A. $Re = 500$.

more accurately the response saturation in terms of amplitude Fig. 5.6 than its structure and position.

Fig. 5.10(b) presents the Power Spectral Density (PSD) of the DNS response to forcing with amplitude $A = 0.1$ at different positions x along the centreline of the domain ($y = 0$) where the response is stronger. An interesting feature is that the optimal frequency is constant at all positions, showing that there is not any zone with a strong competition between oscillating responses at different frequencies and hence the whole response oscillates mainly as a unique coherent structure with a preferred frequency as it is illustrated above for the streamwise wave length in Fig. 5.8.

5.4   Spatio-temporal stochastic forcing

Realistic disturbances to flows generally do not present a clear spatial distribution, therefore, the temporal forcing is now generalised by imposing a white noise forcing $\boldsymbol{f}$ uncorrelated in space and time (Dergham *et al.* (2013); Farrell & Ioannou (2012)). The inlet forcing $\boldsymbol{f}$ is modelled as $\boldsymbol{f} = A\boldsymbol{\xi}(t)$ where $\boldsymbol{\xi}(t)$ is now a column vector of n_k random variables, and $\boldsymbol{\xi}(t)$ is normalised in such a way that the power of $\boldsymbol{f}$ is A^2. The stochastic vector $\boldsymbol{\xi}(t)$ is a Gaussian random process that represents the band limited white noise which is δ-correlated in space and time, has zero mean and unit variance.

Instead of using the finite element basis to represent the spatial noise distribution, it is convenient to use the orthogonal basis resulting from the SVD analysis of the resolvent operator. Introducing the adjoint of the resolvent operator, the linear gain can indeed be rewritten as a
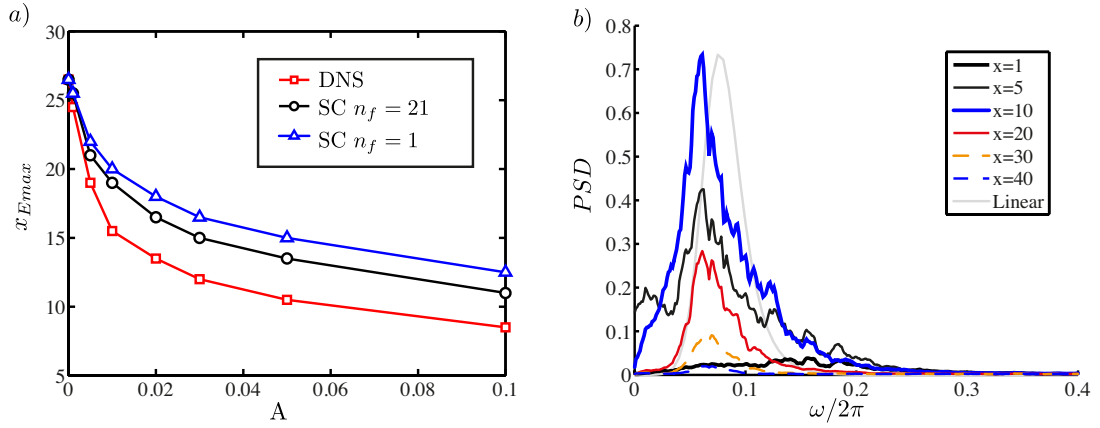
Figure 5.10 – (a) Position in the x coordinate of the maximum of the energy of the perturbation x_{max} for SC and DNS as function of the forcing amplitude A. (b) PSD as function of the frequency for different positions x at the centreline, ($y = 0$), for the DNS fluctuating velocity field for $A = 0.1$ and $Re = 500$.

Rayleigh quotient of the resolvent operator and the forcing,

$$G_1^2(\omega_i) = \frac{(\mathscr{R}\hat{\boldsymbol{f}}_1|\mathscr{R}\hat{\boldsymbol{f}}_1)}{(\boldsymbol{f}_1|\hat{\boldsymbol{f}}_1)} = \frac{(\mathscr{R}^H\mathscr{R}\hat{\boldsymbol{f}}_1|\hat{\boldsymbol{f}}_1)}{(\hat{\boldsymbol{f}}_1|\hat{\boldsymbol{f}}_1)}. \tag{5.19}$$

Subsequently, the optimal gain and forcing on the base flow $\boldsymbol{U}_B$ correspond to the leading eigenvalue $\lambda_1 = G_1^2$ and eigenvector $\tilde{\boldsymbol{f}}_1$ of the symmetrical eigenvalue problem $\mathscr{R}^\dagger\mathscr{R}\tilde{\boldsymbol{f}}_k = \lambda_k\tilde{\boldsymbol{f}}_k$ computed at each frequency ω_i. The family of eigenmodes and eigenvalues constitute a spatial orthogonal basis for the forcing $\tilde{\boldsymbol{f}}_k = \hat{\boldsymbol{f}}_{i,k}$ and corresponding response $\hat{\boldsymbol{u}}_{i,1}$ for each frequency ω_i sorted by their associated gain $G_k(\omega_i)$ as $G_1(\omega_i) > G_2(\omega_i) > G_3(\omega_i)....$ Since the different structures of optimal and suboptimal forcing are equally energetic, they can be normalised such that $\|\hat{\boldsymbol{f}}_{i,k}\|_\Gamma = \pi/n_k\omega_b$. The amplitude of the forcing comes as

$$\langle \int_\Gamma \boldsymbol{f}^2 d\Gamma \rangle = \sum_{i=1}^{n_f} \alpha_i \sum_{k=1}^{n_k} 2A^2 \|\hat{\boldsymbol{f}}_{i,k}\|_\Gamma^2 = A^2 \tag{5.20}$$

The total gain corresponds to an integral in the frequency domain and accounts at each frequency for the different possible response structures with their corresponding gains, all of them forced with equally energetic forcing. In analogy to (5.18) the total gain is written as

$$G_{tot}^2 \simeq \frac{2\pi}{\omega_b} \sum_{i=1}^{n_f} \alpha_i \frac{1}{n_k} \sum_{k=1}^{n_k} G_k(\omega_i)^2, \tag{5.21}$$

where α_i are quadrature coefficients previously introduced.

Truncating the flow dynamics to its most energetic patterns is common in turbulence studies (Berkooz *et al.* (1993)). Thereby, we reduce the complexity of modelling a whole spatio-

temporal stochastic forcing by extracting the most amplified structures of the response $\hat{\boldsymbol{u}}_1$ with their corresponding forcing $\hat{\boldsymbol{f}}_1$ at each frequency in a set of selected frequencies ω_i. At each frequency ω_i, the optimal gain $G_1(\omega_i)$ retrieves the most amplified structures. Hence, knowing that the suboptimal gains are orders of magnitude lower (Boujo & Gallaire (2015); Dergham *et al.* (2013)), we approximate the full response by the most amplified one. The total gain is approximated as

$$G_{tot}^2 \simeq \frac{2\pi}{\omega_b} \sum_{i=1}^{n_f} \alpha_i \frac{1}{n_k} \left(\sum_{k=1}^{n_k} \frac{G_{B,k}^2(\omega_i)}{G_{B,1}^2(\omega_i)} \right) G_1^2(\omega_i) = \frac{2\pi}{\omega_b} \sum_{i=1}^{n_f} \alpha_i \frac{\beta_i}{n_k} G_1^2(\omega_i), \qquad (5.22)$$

where energy weights β_i are calculated at the base flow, where they are known in order to obtain the relation of gains and assuming a constant ratio of the suboptima along the saturation. This procedure recalls (Dergham *et al.* (2013)) where a low rank approximation of the covariance matrix is built by the most energetic responses integrated discretely in the frequency domain. The amplitude of the response is then approximated as

$$B^2 \simeq \sum_{i=1}^{n_f} \alpha_i \beta_i 2 \|\hat{\boldsymbol{u}}_{i,1}\|_\Omega^2, \qquad (5.23)$$

and the coupled system of equations of the self-consistent model is rewritten as

$$\left. \begin{aligned} \mathcal{N}(\boldsymbol{U}) &= -\sum_{i=1}^{n_f} \alpha_i \beta_i 2\Re\left((\bar{\hat{\boldsymbol{u}}}_{i,1} \cdot \nabla) \hat{\boldsymbol{u}}_{i,1} \right) \\ \boldsymbol{U} &= \boldsymbol{u}_{pois} \text{ on } \Gamma, \ \boldsymbol{U} = 0 \text{ on } \Gamma_w \end{aligned} \right\} \qquad (5.24a)$$

$$\left. \begin{aligned} i\omega_i \hat{\boldsymbol{u}}_{i,1} + \mathcal{L}_{\boldsymbol{U}}(\hat{\boldsymbol{u}}_{i,1}) &= 0 \\ \hat{\boldsymbol{u}}_{i,1} = \hat{\boldsymbol{f}}_{i,1} \text{ on } \Gamma, \ \hat{\boldsymbol{u}}_{i,1} = 0 \text{ on } \Gamma_w \end{aligned} \right\} \qquad (5.24b)$$

In general, n_k depends on the spatial number of the degrees of freedom (NDOF) of the white noise, for our simulations $n_k = 80$ coinciding with the NDOF of the mesh at the inlet Γ. Changing the underlaying mesh while maintaining the n_k number yielded the same total gain G_{tot}, showing that n_k is equivalent to the frequency band limit but in space, it represents the band limit of the spatial distribution of the noise, limiting it to a restricted base of n_k degrees of freedom. Similarly to what happens in the frequency domain in (5.12), increasing the number n_k decreases the total gain because energy is spent in finer spatial structures with higher wave number that do not provide large response. Thereby, to obtain a large amplification given a fine enough spatial resolution we need to increase the Reynolds number from $Re = 500$ to $Re = 700$, since the gain increases rapidly with the Reynolds number (Boujo & Gallaire (2015)).

5.4.1 Results: dynamics of the flow subject to spatio-temporal stochastic forcing

The self-consistent model is applied to the backward-facing step problem forced at the inlet Γ with white noise δ-correlated in space and time, with an increasing amplitude A. The SC
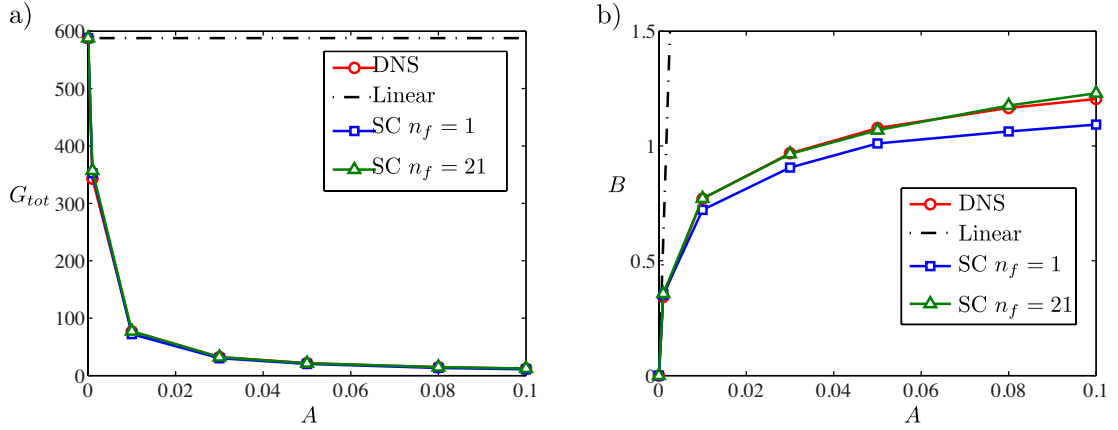
Figure 5.11 – (a) Gain and (b) response as functions of the forcing amplitude A of the band limited white noise for the DNS (circles), SC model integral in frequency with $n_f = 21$ (triangles), SC model with $n_f = 1$ at ω_{opt} (squares) and the linear estimation (dash dotted line). Re=700.

model estimates distinctively well the saturation of the gain and response as illustrated in Fig. 5.11. The SC with the optimal frequency approximation presents a slightly lower response when compared to DNS, but a minimal difference when compared to the linear prediction, which is incorrect in orders of magnitude for a strong saturation. It should be highlighted that the Reynolds stress coupling in the self-consistent model allows to capture the nonlinear response to white noise approximating the whole stochastic response that varies in space and time with the structure of the response solely at the optimal frequency.

A more quantitative comparison of the flow features between the SC model and the exact DNS reveals that the SC model captures the main trends in the variation of the flow configuration as presented in Fig. 5.12, however, surprisingly not as accurately as the estimation of the global energy of the response. Focusing on the recirculation bubbles of the mean flow
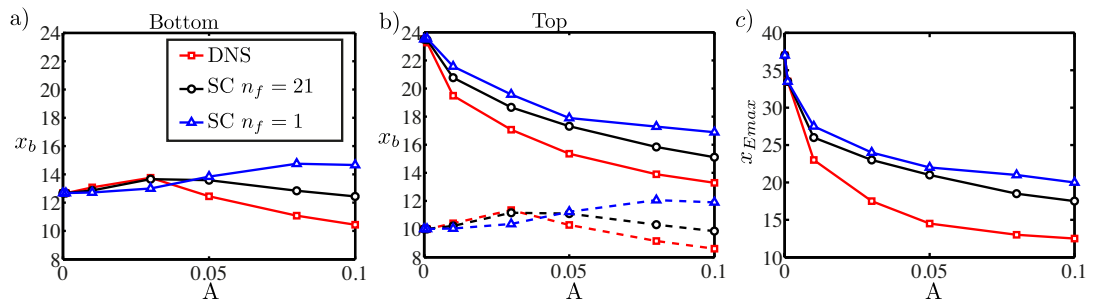
Figure 5.12 – Position of the recirculation bubbles (a) bottom and (b) top for the DNS (squares), SC model integrated in frequency (circles) and SC model with optimal frequency approximation (triangles) as function of the forcing amplitude A. (c) Position maximum of the energy of the perturbation x_{Emax} for the SC model and DNS as function of the forcing amplitude A. Re=700.

Fig. 5.12(a)-(b), the frequency integrated SC model follows approximately the DNS capturing

the non-monotonous behaviour, however, the SC model with a single frequency approximation provides only a very coarse estimation of the recirculation bubble migration failing to capture the non-monotonous trend. In terms of the position of the maximum of the fluctuating energy, depicted in Fig. 5.12(c), the SC model captures well the migration upstream but maintaining a mismatch for large saturations. As one could expect, this mismatch is stronger for the SC model with a single frequency approximation of the response. It should be noted that the self-consistent model is able to approximate considerably well the flow behaviour given the strong assumptions involved, consolidating the Reynolds stress as the key nonlinear term implicated in the saturation process.

5.5 Discussion and conclusions

The backward-facing step is a well known example of an amplifier, where small perturbations to the steady base state produce large amplifications due to the non-normality of the linearised equations. This amplifications depend strongly on the frequency of the perturbations (Marquet & Sipp (2010); Boujo & Gallaire (2015)) showing a low frequency band pass filtering with an optimal frequency. In the present work the backward-facing step is forced at the inlet with a band limited white noise to model disturbances that appear naturally in flows. We apply a semi-linear model to describe the nonlinear dynamics of the filtering, and the saturation of the response with an increasing amplitude of the stochastic forcing.

The study of the stochastic forcing and response is addressed in the frequency domain, introducing the self-consistent model (5.14) which consists in a coupled system of the mean flow equation and the linear response equation around the aforementioned mean flow at different frequencies. The coupling is attained by the Reynolds stress that forces the mean flow and it is constructed from the integration of the different responses in the frequency domain using a proper energy weighting by the linear gain distribution at the base flow. The model is applied to the nonlinear saturation problem, starting with a forcing with fixed Poiseuille structure but stochastic in time, obtaining a remarkably accurate prediction of the global saturation of the response when compared to the DNS results. A more quantitative comparison describes an accurate estimation of the shortening of the mean recirculation bubble, capturing the non-monotonous trend. In addition, the comparison of the fluctuating response shows that the model predicts considerably well the upstream migration of the response, while providing an estimation of the streamwise wave length despite the stochasticity of the response. An interesting feature of the DNS response is that it presents the same optimal frequency at different stages in the streamwise direction and thus it is governed mainly by a single coherent structure oscillating at the preferred frequency.

The response to a more realistic disturbances, described by a stochastic forcing δ-correlated in space and time, is modelled by extracting the most energetic structures (Dergham *et al.* (2013)) as commonly used in turbulence studies (Berkooz *et al.* (1993)). Based on this optimal structures, the SC model is rewritten (5.24) using the optimal forcing and corresponding

response at each frequency with their proper energetic weights. The reformulated model is able to estimate accurately the saturation of the response and considerably well the decrease of the mean recirculation bubble and migration of the response, despite a purely stochastic forcing.

The results obtained suggest that the nonlinear dynamics of the saturation process in the backward-facing step is mainly governed by the nonlinear Reynolds stress forcing even for a stochastically forced flow, and that the nonlinear interaction of the fluctuation with itself has a secondary effect. Besides, it should be noted that the full response to stochastic noise is well approximated by the most energetic structure at the optimal frequency. The presented model follows as an extension to stochastic flows of the self-consistent model proposed for harmonic fluctuations. It was applied to an amplifier to calculate the saturation of the response to harmonic forcing on the backward-facing step (Mantič-Lugo & Gallaire (2015)), and to an oscillator, the unstable cylinder wake (Mantič-Lugo *et al.* (2014, 2015)), where the instability is dominated by the most unstable eigenmode, and its saturation is dictated by the unstable eigenmode marginality criterion (Malkus (1956); Stuart (1958); Barkley (2006)). Thereby, a common physical picture is revealed; as the fluctuations grow due to an increasing response to forcing or an instability mechanism respectively, it creates a Reynolds stress forcing that modifies the mean flow reducing its amplification and thus saturating the flow response.

One of the fundamental aspects behind the self-consistent model is that the full nonlinear response to stochastic forcing is approximated by a linear response at different forcing frequencies, still being capable to estimate the non-linear transfer function of the system, and approximate the nonlinear filtering of the white noise forcing, flat in the frequency domain, into a low frequency band pass with a preferred frequency and response structure. This concept of nonlinear transfer function named describing function is defined for the first harmonic approximation of the nonlinear response in Noiray *et al.* (2008) and applied to the stability behaviour of flames in burners Nevertheless, it should be highlighted that the solutions of the self-consistent model are obtained *a priori* without using any DNS or experimental data. Similar models where the mean flow is coupled to the linear perturbation equations through the Reynolds stress forcing can be found in the study of turbulent flows, as for example in Beaume *et al.* (2015) to compute coherent structures that appear during the transition in a parallel shear flow. Another example is the stochastic structural stability theory (SSST) introduced by Farrell & Ioannou (2003, 2012) where the ensemble average mean flow equation is coupled to the linear response formulated in the terms of covariance matrix and governed by the Lyapunov equation. The SSST has been applied to parallel turbulent flows describing well the nonlinear behaviour that produces sustained coherent structures. Nonetheless, the requirement of solving a Lyapunov equation limits the domain size and geometry due to the computational cost. In this sense, low order approximation to the covariance matrix have been proposed to approximate the linear response (Farrell & Ioannou (2001); Dergham *et al.* (2013)) and in which case our present model is an extreme case with strong assumptions but still being able to capture the main nonlinear behaviour of the system.

As a final note, the present model is not conceived as a substitute for the Navier-Stokes equations. In contrast, its significance lies on the integration of only the essential ingredients required to provide a fairly accurate description of the physics. It remains to be seen whether the present self-consistent model works in other globally stable laminar flows excited by stochastic forcing.

6 | Discussion

6.1 Mean flow and base flow: Marginal stability criterion and influence of higher harmonics

Linear stability analysis around a steady solution of a general dynamical system has been a well known tool to study and describe the dynamical behaviour of systems. In this context, stability analysis of the linearised Navier-Stokes equations around a steady solution has been adopted many times to describe the dynamics of different flow configurations. Restricting our attention to oscillators, and specifically to the cylinder wake flow, we have seen that the linear stability analysis around the base flow does not provide an accurate prediction of the flow dynamics, in terms of frequency and structure of oscillations.

Why base flow linear stability analysis is condemned to fail?

To clarify, the standard global linear stability analysis around the steady NSE comes from the solution of the system

$$\mathcal{N}(\boldsymbol{U}_B)\boldsymbol{U}_B = 0, \tag{6.1a}$$

$$\partial_t \boldsymbol{u}'_{1B} + \mathcal{L}(\boldsymbol{U}_B)\boldsymbol{u}'_{1B} = 0 \iff \lambda_1 \boldsymbol{u}_{1B} + \mathcal{L}(\boldsymbol{U}_B)\boldsymbol{u}_{1B} = 0, \tag{6.1b}$$

where $\mathcal{N}$ and $\mathcal{L}$ are the nonlinear and linear operators described before in (2.1), $\boldsymbol{U}_B$ is the base flow or steady solution of the NSE. The linearized Navier-Stokes equations around the base flow $\boldsymbol{U}_B$ (6.1a) are rewritten as a standard eigenvalue problem where the perturbation can be expanded into the basis of its eigenmodes $\boldsymbol{u}'_{nB} = A\boldsymbol{u}_{nB}e^{\lambda_n t} + cc.$, with $\boldsymbol{u}_{1B}$ being the unstable eigenmode with complex eigenvalue $\lambda_1 = \sigma_1 + i\omega_1$, $cc.$ is the complex conjugate, and the amplitude A is an unknown and free.

In previous sections the discrepancy between linear stability analysis around the base flow and mean flow has been highlighted, however, this issue is addressed here in more detail. We start by using the Reynolds decomposition as applied previously in Section 2.2. Thus, the full

velocity field $\boldsymbol{u}$ is decomposed as

$$\boldsymbol{u} = \boldsymbol{U} + \boldsymbol{u}' = \boldsymbol{U}_B + \Delta\boldsymbol{U} + \boldsymbol{u}', \tag{6.2}$$

where we define $\boldsymbol{U}$ as the time averaged mean flow $\boldsymbol{U} = \langle\boldsymbol{u}\rangle$, where $\langle\cdot\rangle$ denotes the time average, $\boldsymbol{u}'$ denote the pure fluctuating field which has zero mean $\langle\boldsymbol{u}'\rangle = 0$ by construction, $\boldsymbol{U}_B$ denotes the base flow, steady solution of the NSE (6.1a), and $\Delta\boldsymbol{U}$ represents the steady modification between the mean flow and base flow. Using this Reynolds decomposition the NSE are rewritten as

$$\mathcal{N}(\boldsymbol{U}) = -\langle(\boldsymbol{u}'\cdot\nabla)\boldsymbol{u}'\rangle, \tag{6.3a}$$

$$\partial_t\boldsymbol{u}' + \mathcal{L}(\boldsymbol{U})\boldsymbol{u}' = -(\boldsymbol{u}'\cdot\nabla)\boldsymbol{u}' + \langle(\boldsymbol{u}'\cdot\nabla)\boldsymbol{u}'\rangle. \tag{6.3b}$$

Note that no simplification has been performed and that the fluctuation $\boldsymbol{u}'$ does not have to be small compared to the mean $\boldsymbol{U}$. The system (6.3) is composed of two coupled equations. The mean flow $\boldsymbol{U}$ is not a solution of the NSE, as remarked by Barkley (2006) but instead a solution of the steady mean flow equation (6.3a) forced by the Reynolds stress divergence $\langle(\boldsymbol{u}'\cdot\nabla)\boldsymbol{u}'\rangle$. The second fluctuation equation (6.3b) describes the fluctuating field $\boldsymbol{u}'$.

The linear global stability analysis performed around the mean flow can be written in the following system of equations

$$\mathcal{N}(\boldsymbol{U}) = -\langle(\boldsymbol{u}'\cdot\nabla)\boldsymbol{u}'\rangle, \tag{6.4a}$$

$$\partial_t\boldsymbol{u}'_1 + \mathcal{L}(\boldsymbol{U})\boldsymbol{u}'_1 = 0 \iff \lambda_1\boldsymbol{u}_1 + \mathcal{L}(\boldsymbol{U})\boldsymbol{u}_1 = 0, \tag{6.4b}$$

where $\boldsymbol{u}_1$ represents the most unstable eigenmode, and the nonlinear interactions between the different harmonics have been neglected.

Looking in detail at (6.1) and (6.2) we can see that the linear stability around the base flow approximates the flow behaviour as $\boldsymbol{u} \simeq \boldsymbol{U}_B + \boldsymbol{u}'_{1B}$, where $\boldsymbol{u}'_{1B}$ is a purely time dependent fluctuation like $\boldsymbol{u}'$. Therefore, there is little chance that this approximation can estimate correctly the flow behaviour unless $\Delta\boldsymbol{U}$ is zero, or at least much smaller than $\boldsymbol{u}'_{1B}$, which is only true at the onset of the instability since the mean flow modification $\Delta\boldsymbol{U}$ grows along with the perturbation $\boldsymbol{u}'_1$ due to the Reynolds stress divergence (6.4a), see also Chapter 3 for more details. In contrast, the stability analysis around the mean flow (6.4) approximates the flow as $\boldsymbol{u} = \boldsymbol{U} + \boldsymbol{u}' \simeq \boldsymbol{U} + \boldsymbol{u}'_1$, which means that the full fluctuating velocity is approximated by the most unstable mode. This comparison is illustrated in Fig. 6.1 where the full multidimensional state variables of the unsteady attractor $\boldsymbol{u}$ that represents the limit cycle solution of the exact NSE is projected in two-dimensions to clarify the concept. We can see that, unless $\Delta\boldsymbol{U} = 0$, or at least negligible when compared to $\boldsymbol{u}'$, the eigenmode $\boldsymbol{u}_{1B}$ of the base flow (in blue) would not approximate correctly the full velocity field $\boldsymbol{u}'$. However, the eigenmode around the mean flow $\boldsymbol{u}_1$ (in red) is just a one frequency approximation of the full fluctuating field $\boldsymbol{u}'$.
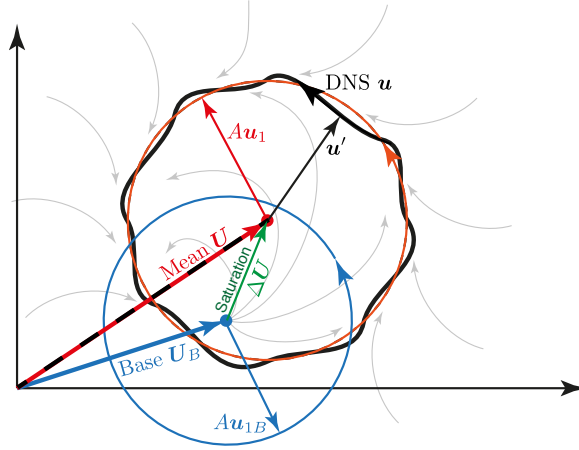
Figure 6.1 – Illustrative sketch of the phase portrait of a supercritical oscillator during the saturation into a limit cycle. The multidimensional state variable that defines the system is projected into two-dimensions for the sake of clarity. The attractor of the limit cycle that represents the exact periodic solution is represented by u (black) and obtained from Direct Numerical Simulation (DNS) of the time varying Navier-Stokes equations. The unstable steady solution of the Navier-Stokes equation is denoted as the base flow U_B (blue), along with its unstable eigenmode u_{1B} (blue) from linear stability analysis around the base flow (6.1). The time averaged solution is represented by the mean flow U (red), along with its most unstable eigenmode u_1 (red) from linear stability analysis around the mean flow (6.4). Notice that the amplitude A of the eigenmodes is unknown.

Particularly for the unstable cylinder wake the difference between the base flow and mean flow is very strong as depicted previously in Fig. 1.5 -2.2–3.5, thus explaining the obvious failure of the base flow stability analysis to describe the dynamical behaviour of the limit cycle. Furthermore a phase portrait of the velocity field at the point ($x = 2$, $y = -1$) is presented in Fig. 6.2, where the saturation to the limit cycle from the base flow steady unstable solution to the mean flow limit cycle is clear. The mean flow marginally stable mode represents a good approximation of the limit cycle but missing the amplitude of the fluctuating term. Nonetheless, the fluctuation amplitude is estimated by the self-consistent model, *a priori*, without resorting to the DNS mean flow, approximates the structure of the vortex shedding even better than the linear stability analysis around the mean flow, see Chapter 3, highlighting the relevance of the model. It should be noted, that the mean flow is not a steady solution of the NSE as seen in the phase portraits Fig. 6.1 and Fig. 6.2. The description presented above seems natural to other flows exhibiting supercritical bifurcations, although its generality should be verified.

Mean flow stability and one harmonic approximation

As described in Section 3.2, the complex nonlinear interactions of the full NSE is decomposed into several different nonlinear effects in the coupled equations (6.3). The mean flow linearised
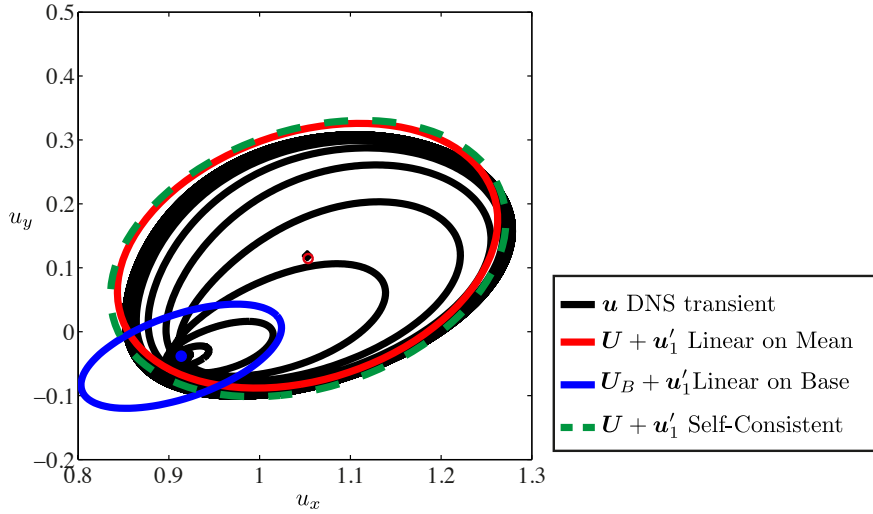
Figure 6.2 – Phase portrait of the velocity in $(\boldsymbol{u}_x, \boldsymbol{u}_y)$ at the point $(x = 2, y = -1)$ for the cylinder wake flow at Re=100. The DNS exact path of the full velocity $\boldsymbol{u}$ during the transient to the limit cycle is in black. The linear fluctuation approximated by the linear stability around the mean flow $\boldsymbol{u}'_1$ is represented in red. The linear fluctuation approximated by the stability around the base flow is in blue. The self-consistent model approximation is in dotted green.

fluctuation equation neglects the RHS of (6.3b), $(\boldsymbol{u}' \cdot \nabla)\boldsymbol{u}' - \langle(\boldsymbol{u}' \cdot \nabla)\boldsymbol{u}'\rangle$, and thus restricts the fluctuation to one harmonic approximation which is described by the most unstable eigenmode $\boldsymbol{u}' \simeq \boldsymbol{u}'_1$, since the rest of eigenmodes would eventually decay. In several oscillators, such as the cylinder flow, this approximation holds very well and the most unstable mode provides a very good description of the flow behaviour, in terms of fluctuating structure and frequency in many cases (Triantafyllou *et al.* (1986); Hammond & Redekopp (1997); Pier (2002); Barkley (2006); Sipp & Lebedev (2007)). A particular feature is that the mean flow is marginally stable, also called the real-zero imaginary-frequency (RZIF) property (Barkley (2006); Sipp & Lebedev (2007); Turton *et al.* (2015)), which means that the flow is purely fluctuating, neither growing nor decaying, as appropriate for a limit cycle.

Reynolds stress and higher harmonics in linearly unstable mean flows

The described linear stability approximation does not hold for all configurations, and many flow, standing waves (Turton *et al.* (2015)) or turbulent cases (Meliga *et al.* (2012)), present an unstable mode around the mean flow. This means that the fluctuation equation around the mean flow (6.3b) is linearly unstable with $\sigma > 0$ (Meliga *et al.* (2012)), but nonlinearly stable oscillating in a limit cycle. In other words, the nonlinearity retained in the Reynolds stress is not enough to obtain a pure fluctuation and therefore, the neglected nonlinear term in the RHS of (6.3b), which accounts for the higher harmonic interactions, plays a relevant role in the saturation into a limit cycle. In Turton *et al.* (2015) the authors provide a general demonstration that the behaviour of a flow with peaked temporal power spectrum, that is

to say a quasi-monochromatic oscillation dominated by the fundamental frequency, can be predicted well from the linear global stability around the mean. In contrast, flows where the nonlinear interactions of the different harmonics is relevant to the saturation process into a limit cycle present in general a broad spectrum, and thus the mean flow linear stability would exhibit a positive growth rate and would not predict the correct nonlinear frequency. Therefore, the self-consistent model presented in Chapters 2, 3 and 4 is restricted to quasi-monochromatic flows.

It is of interest to highlight that simple models that are used to describe the nonlinear flow behaviour in limit cycles, like the Stuart-Landau amplitude equation, do indeed account for the neglected nonlinear interactions of harmonics, at least at leading order. To explore this in details, let us start by recalling the asymptotic expansion introduced in Section 4.4 for amplifiers that can be also extrapolated to oscillators with the small parameter ϵ corresponding to the amplitude of the linear perturbation $\boldsymbol{u}_1'$ with eigenvalue $\lambda_1 = \sigma_1 + i\omega_1$ around the base flow $\boldsymbol{U}_B$. The first non-linear terms appear at second order ϵ^2 from the two nonlinearities described above;

- The mean flow modification $\boldsymbol{U}_0$: $\mathscr{L}_{\boldsymbol{U}_B}\boldsymbol{U}_0 = -((\bar{\boldsymbol{u}}_1 \cdot \nabla)\boldsymbol{u}_1 + (\boldsymbol{u}_1 \cdot \nabla)\bar{\boldsymbol{u}}_1) \propto |\boldsymbol{u}_1|^2$

- The second harmonic $\boldsymbol{u}_2$: $[i2\omega_1 + \mathscr{L}_{\boldsymbol{U}_B}]\boldsymbol{u}_2 = -(\boldsymbol{u}_1 \cdot \nabla)\boldsymbol{u}_1 \propto |\boldsymbol{u}_1|^2$

both proportional to the square of the perturbation and where the overbar represents complex conjugate. The saturation dynamics appears at third order ϵ^3 from the correction of the perturbation $\boldsymbol{u}_1$, with the interactions of the second order nonlinear terms with the perturbation itself,

$$[i\omega_1 + \mathscr{L}_{\boldsymbol{U}_B}]\boldsymbol{u}_1 = ((\boldsymbol{U}_0 \cdot \nabla)\boldsymbol{u}_1 + (\boldsymbol{u}_1 \cdot \nabla)\boldsymbol{U}_0) + \propto |\boldsymbol{u}_1|^2 \boldsymbol{u}_1 \tag{6.5a}$$

$$((\boldsymbol{u}_2 \cdot \nabla)\bar{\boldsymbol{u}}_1 + (\bar{\boldsymbol{u}}_1 \cdot \nabla)\boldsymbol{u}_2) \propto |\boldsymbol{u}_1|^2 \boldsymbol{u}_1 \tag{6.5b}$$

and thus there are two main sources of non-linear saturation; first, the mean flow modification and, second, the interaction with the second harmonic. The degenerate nature of the linear operator for the unstable mode with eignenvalue $\lambda = \sigma + i\omega$ can be circumvented by assuming the correction of the perturbation $\boldsymbol{u}_1$ as a response to a forcing at frequency ω_1, which is natural for $\sigma \neq 0$.

These two non-linear saturation mechanisms are accounted in the cubic term of the Stuart Landau amplitude equation (Stuart (1960)),

$$\frac{dA}{dt} = \lambda A - (\mu + \nu)|A|^2 A, \tag{6.6}$$

in the coefficients μ for the mean flow correction and ν for the second harmonic interaction, that can be extracted from a weakly nonlinear analysis around the base flow at critical Reynolds number; see Sipp & Lebedev (2007) for more details. It should be noted that the amplitude equation does not provide any information about the spatial structure of the oscillations.

When the mean flow linear stability analysis is performed, only the term μ is accounted, since it represents the mean flow modification by the Reynolds stress forcing, and the ν coefficient is neglected. Therefore, this approach works when ν is small and the higher harmonic interaction is negligible in the saturation process. The self-consistent model suffers from the same pathology.

A simplified approach, as an alternative to solving the full nonlinear fluctuation equation, could be to slave the higher harmonics to the fundamental unstable mode, following the asymptotic expansion of Section 4.4 and build a coupled set of equations for the harmonic interactions. Nonetheless, this coupling is not obvious since the amplitude of the most unstable mode is not set uniquely in absence of the equivalent of the marginal stability criterion for an unstable mean flow with $\sigma > 0$, see Chapters 2 and 3. In contrast, in the case of amplifiers, the amplitude of the fluctuation is not a free parameter, thus allowing the introduction of higher harmonics, as addressed in the following.

Amplifiers, white noise and higher harmonics

Similar reasoning as explained for oscillators in Fig. 6.2 applies to amplifiers, in terms of the base flow modification to the mean flow, when looking at the response to forcing. The steady mean flow modification $\Delta \boldsymbol{U}$ is required to obtain a correct description of the flow by the linear response to forcing, which in this case substitute the linear stability equation. The main difference is related to the mean flow dependency on the amplitude of the forcing, and that there is not a unique limit cycle given by the saturation of the unstable mode as in the oscillators. In contrast, for each amplitude of the forcing there is a different response, in terms of structure and amplitude as seen in Fig. 4.3.

It should be highlighted that in general, a broad band frequency of the response to forcing does not imply directly that the nonlinear terms of RHS of the fluctuating equation (6.3b) are relevant. For example, as seen in Chapter 5, the backward-facing step flow is forced by white noise presenting a broad band spectrum of the response, however, a coupling between the mean flow and a linear response equation at each frequency captures the nonlinear saturation in terms of energy and structure, thus suggesting that at least in this case the nonlinear terms of the RHS of the fluctuation equation are negligible. Nonetheless, in the case where there is a fundamental harmonic driven by the response to harmonic forcing or by a unique unstable mode, the fundamental harmonic grows and can interact, creating higher harmonics, which, when large, exhibit a broad band frequency spectrum and influence the flow behaviour revealing the nonlinear harmonic interaction as important.

When the nonlinear interaction of the different harmonics plays an important role in the nonlinear behaviour of the flow, the self-consistent model can be expanded to account for these interactions for amplifiers. In contrast to oscillators where the amplitude of the response is unclear, for the amplifiers the amplitude of the different harmonics is slaved to the response to forcing. For example, introducing the second harmonic in the self-consistent model, it is

formalised as

$$\mathcal{N}(\boldsymbol{U}) = -2\Re\left((\bar{\boldsymbol{u}}_1 \cdot \nabla)\boldsymbol{u}_1\right) - 2\Re\left((\bar{\boldsymbol{u}}_2 \cdot \nabla)\boldsymbol{u}_2\right), \tag{6.7a}$$

$$i\omega\boldsymbol{u}_1 + \mathcal{L}_{\boldsymbol{U}}(\boldsymbol{u}_1) = \left((\boldsymbol{u}_2 \cdot \nabla)\bar{\boldsymbol{u}}_1 + (\bar{\boldsymbol{u}}_1 \cdot \nabla)\boldsymbol{u}_2\right) + \boldsymbol{f}_1, \tag{6.7b}$$

$$i2\omega\boldsymbol{u}_2 + \mathcal{L}_{\boldsymbol{U}}(\boldsymbol{u}_2) = -(\boldsymbol{u}_1 \cdot \nabla)\boldsymbol{u}_1, \tag{6.7c}$$

where the harmonic forcing is given by $\boldsymbol{f}_1$. Note that for the numerical solution there is an extra iterative loop to couple the first and second harmonic equations before they retroact in the mean flow through the Reynolds stress. In addition, the increase in order of harmonics hampers the numerical accuracy since their interaction introduces large order of derivatives requiring a very fine mesh or high order polynomials in the discretisation, not to increase the numerical errors.

6.2 Self-consistent model for turbulent flows

So far, the introduced model has been applied only to laminar flows at low or moderate Reynolds numbers. However, the self-consistent formalism can be formally expanded to turbulent flows at high Reynolds numbers. Following the approach proposed by Reynolds & Hussain (1972); Viola *et al.* (2014), the unsteady flow $\boldsymbol{u}(x,t)$ is decomposed into a steady time average mean flow $\bar{\boldsymbol{u}} = \boldsymbol{U}$, a coherent motion $\tilde{\boldsymbol{u}}$ that describes the slowly varying structures, and the fast fluctuating turbulent motion $\boldsymbol{u}'$,

$$\boldsymbol{u} = \boldsymbol{U} + \tilde{\boldsymbol{u}} + \boldsymbol{u}', \tag{6.8}$$

where the sum of coherent structure plus the time averaged mean flow coincide with ensemble averaged flow, $<\boldsymbol{u}> = \boldsymbol{U} + \tilde{\boldsymbol{u}}$. The nonlinear evolution of the coherent structures is described by

$$\mathcal{N}(\boldsymbol{U}) = -\overline{(\tilde{\boldsymbol{u}} \cdot \nabla)\tilde{\boldsymbol{u}}} - \overline{(\boldsymbol{u}' \cdot \nabla)\boldsymbol{u}'}, \tag{6.9a}$$

$$\partial_t\tilde{\boldsymbol{u}}_1 + \mathcal{L}(\boldsymbol{U})\tilde{\boldsymbol{u}}_1 = -[(\tilde{\boldsymbol{u}} \cdot \nabla)\tilde{\boldsymbol{u}} - \overline{(\tilde{\boldsymbol{u}} \cdot \nabla)\tilde{\boldsymbol{u}}}] - [\langle(\boldsymbol{u}' \cdot \nabla)\boldsymbol{u}'\rangle - \overline{(\boldsymbol{u}' \cdot \nabla)\boldsymbol{u}'}], \tag{6.9b}$$

where $\mathcal{L}(\boldsymbol{U})$ and $\mathcal{N}(\boldsymbol{U})$ are the linear and Nonlinear NS operators around the steady mean flow $\boldsymbol{U}$. The stability analysis of the flow is verified by the modal analysis of the linearised dynamics of the coherent structures, given by the tendency of $\tilde{\boldsymbol{u}}$ to grow or decay, as described in the literature, e.g. Meliga *et al.* (2012); Viola *et al.* (2014). For this purpose, the nonlinear term $[(\tilde{\boldsymbol{u}} \cdot \nabla)\tilde{\boldsymbol{u}} - \overline{(\tilde{\boldsymbol{u}} \cdot \nabla)\tilde{\boldsymbol{u}}}]$ of the coherent interaction with itself is neglected as usual in linear stability analysis, however, the system of equations is not closed and the coherent turbulent fluctuation $[\langle(\boldsymbol{u}' \cdot \nabla)\boldsymbol{u}'\rangle - \overline{(\boldsymbol{u}' \cdot \nabla)\boldsymbol{u}'}]$ need to be modelled by using the standard Boussinesq hypothesis and a turbulence model (Reynolds & Hussain (1972); Pope (2000); Cossu *et al.* (2009); Meliga *et al.* (2012); Viola *et al.* (2014)).

Subsequently, the self-consistent model is constructed to describe the coherent linear equa-

tion and couple it to the mean flow equation, through the Reynolds stress. The full nonlinear coherent fluctuation $\tilde{\boldsymbol{u}}$ is approximated by a unique harmonic $\tilde{\boldsymbol{u}}_1$ that comes from stability analysis or linear response to forcing as described in Chapters 2, 3 and 4 for laminar flows. An important point is that the Reynolds stresses of the coherent $\tilde{\boldsymbol{u}}$ and the turbulent fluctuations $\boldsymbol{u}'$ are not mixed, and are independent (6.9a). This independence can be interpreted by the different averaging methods, ensemble and time average, or also by the frequency independence as described in Chapter 5. Thus, different approaches can be applied to calculate separately each term of the Reynolds stresses. The turbulent Reynolds stress divergence is calculated using the Bousinessq hypothesis and any standard turbulence model, while the coherent Reynolds stress divergence is computed by the unique harmonic $\tilde{\boldsymbol{u}}_1$ as described in Chapters 2, 3 and 4 .

Extending the linearisation of (6.9b) described in Viola *et al.* (2014) or Meliga *et al.* (2012) the self-consistent model can be formalised to describe the dynamics of the coherent structures $\tilde{\boldsymbol{u}}$ in the following form

$$\mathcal{N}^*(\boldsymbol{U}) - \nabla \cdot \left(\nu_t [\nabla + \nabla^T] \boldsymbol{U} \right) = -\overline{(\tilde{\boldsymbol{u}}_1 \cdot \nabla) \tilde{\boldsymbol{u}}_1}, \tag{6.10a}$$

$$\partial_t \tilde{\boldsymbol{u}}_1 + \mathcal{L}(\boldsymbol{U}) \tilde{\boldsymbol{u}}_1 = \nabla \cdot \left(\nu_t [\nabla + \nabla^T] \tilde{\boldsymbol{u}}_1 \right) + \nabla \cdot \left((\nabla_{\boldsymbol{U}} \nu_t \cdot \tilde{\boldsymbol{u}}_1) [\nabla + \nabla^T] \boldsymbol{U} \right), \tag{6.10b}$$

$$\nu_t = \mathrm{TM}(\boldsymbol{U}), \tag{6.10c}$$

where $\tilde{\boldsymbol{u}}_1$ represents the most unstable eigenmode, and $\mathcal{N}^*$ is the standard nonlinear NS operator but written for the corrected pressure p^* that takes into account the isotropic term of the turbulent Reynolds stress tensor, while the turbulence model $\mathrm{TM}(\boldsymbol{U})$ models the deviatoric part. Whether this extended self-consistent model provides a correct approximation of the coherent structures in turbulent flows remains an open issue and a natural extension of my work.

6.3 Is the Reynolds stress forcing always staturating?

All the examples proposed in this work dealt with cases in which the interaction of the fluctuation and the mean flow resulted in a stabilisation (saturation) of the fluctuation. In other words, the nonlinear interaction of the mean flow and the linear approximation of the fluctuating part inherent to the self-consistent model yielded a nonlinear saturation. In oscillators, particularly in the cylinder flow (Chapters 2 and 3), this interaction resulted in a stabilisation of the unstable mode, until marginal stability was achieved and the flow was saturated in a pure periodic limit cycle. In amplifiers, as the backward-facing step flow (Chapters 4 and 5), it resulted in a saturation of the amplification of the response to forcing in both cases; harmonic and stochastic.

There are flows like Poiseuille or Couette flow that are linearly stable, but undergo a transition into different flow configurations once sufficiently forced or even exhibit unsteady self-sustained coherent structures that are present in the transition to turbulence and con-

tinue to exist even once the initial forcing is eliminated. This nonlinear evolution has been captured by different semi-linear models where the averaged mean flow is coupled to a linear fluctuating equation through the Reynolds stress, as described in Chapter 1, see for example, Farrell & Ioannou (2012); Beaume *et al.* (2015); Thomas *et al.* (2014).

I hypothesise that the non-linear behaviour that accounts for the appearance of self-sustained coherent structures in stable flows like Poiseuille or Couette could also be described by the self-consistent model since it maintains key similarities to the above models. The following picture can be evoked: the linear response to a strong enough forcing entails such a variation in the mean flow, due to the Reynolds stress, that the linear operator of the response to forcing would change from linearly stable to unstable and thus explaining the appearance of self-sustained coherent structures. This idea can be viewed also in the context of subritical flows, where, as already reviewed in Godreche & Manneville (1998) and described in Ehrenstein & Koch (1991), nonlinear travelling waves can appear below the critical Reynolds number in plane Poiseuille flow. This would mean that open flows can be categorised into two groups depending on their nonlinear dynamics.

- Reynolds stress forcing stabilisation: The nonlinear interactions of the Reynolds stress and the linear fluctuation result in a saturation of the fluctuation, reducing he instability growth rate in oscillators or its gain in amplifiers. This would correspond to a supercritical bifurcation.

- Reynolds stress forcing destabilisation: Stable flows where the nonlinear interaction of the Reynolds stress and the linear fluctuation results in a destabilisation, increasing the growth rate of unstable flows and the gain of the nonlinear response when compared to the linear response and eventually leading to a new dynamical setting. This would correspond to a subcritical bifurcation.

This conjecture is supported by the preliminary results obtained by applying the self-consistent model in two-dimensional parallel flows. The full flow field $\boldsymbol{u}(x, y, t)$ is decomposed by a streamwise averaged mean flow only in the streamwise x-direction $\boldsymbol{U}_x(y)$, plus a linear approximation of the full nonlinear fluctuation in the form of $\boldsymbol{u}'(x, y, t) \simeq A\boldsymbol{u}_1(y)e^{ikx+\lambda t} + cc.$, for $\lambda = \sigma + i\omega$ and where a wave number expansion with spatial real wave number k is applied in the streamwise direction as standard of linear local analyses, see Schmid & Henningson (2001) for more details. The self-consistent model is constructed following the same philosophy of Chapters 2 and 3 under the parallel flow restrictions,

$$-\frac{1}{Re}\frac{d^2 U_x}{dy^2} + \frac{dP}{dx} = -A^2\left(\bar{u}_{1y}\frac{du_{1x}}{dy} + u_{1y}\frac{d\bar{u}_{1x}}{dy}\right), \qquad (6.11\text{a})$$

$$\lambda_1 \boldsymbol{u}_1 + \mathscr{L}_U(\boldsymbol{u}_1) = 0. \qquad (6.11\text{b})$$

where $\boldsymbol{u}_1 = [u_{1x}, u_{1y}]$ is the most unstable eigenmode, P is the fixed base flow pressure and $\mathscr{L}$ is the reformulated linear operator around the parallel mean flow. Two different flows are
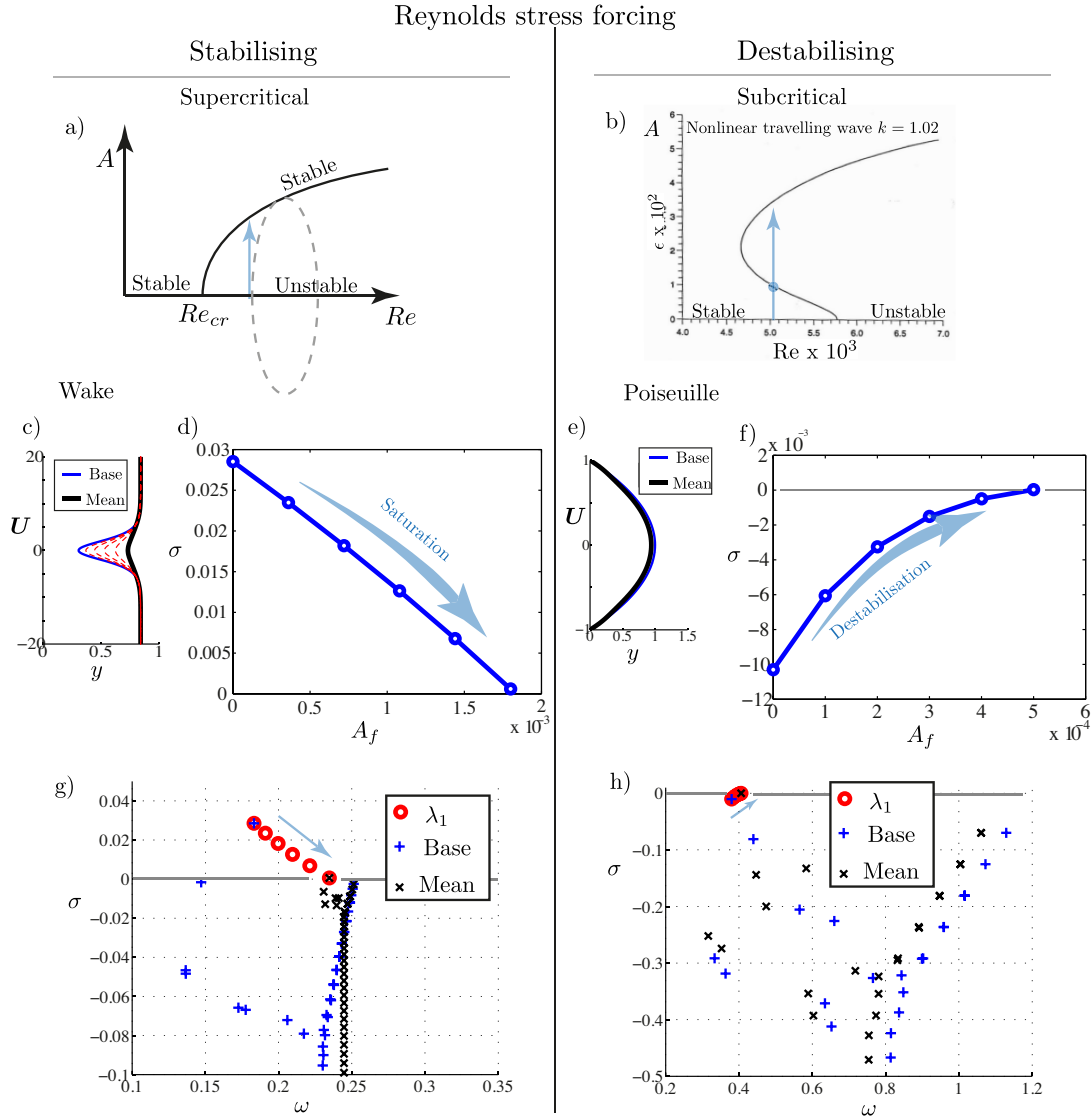
Reynolds stress forcing

Figure 6.3 – Categorisation of flows depending on whether the Reynolds stress forcing stabilises or destabilises the flow. Sketch of a supercritical Hobf bifurcation (a), nonlinear travelling wave in a subcritical Poiseuille for $k = 1.02$ (b) (Godreche & Manneville (1998); Ehrenstein & Koch (1991)). Applying the self-consistent model to 2D parallel flows; a stabilising case, an unstable synthetic wake (c) for $Re = 100$ and wavenumber $k = 0.3$, similar to the one studied in Pier & Huerre (2001), (left), and a destabilising case, the stable Poiseuille flow (e) at $Re = 3000$ and a wavenumber $k = 1.2$, (right). The evolution of the growth rate as function of the amplitude is shown in (d,f). The eigenspectrum of the mean flow and base flow is shown in (g,h).

studied: a synthetic wake at $Re = 100$ similar to the one presented in Pier & Huerre (2001) and the well known Poiseuille flow at $Re = 3000$. The wave number is fixed and chosen from the most unstable combination from the linear dispersion relation of the base flow. The wake base flow is described by $\boldsymbol{U}_x = 0.84 - 0.54 \operatorname{sech}(0.35y)^2$ and it is linearly unstable at $Re = 100$ for the selected wavenumber $k = 0.3$ with an eigenvalue $\lambda_{1B} = \sigma_{1B} + i\omega_{1B} =$

$0.183 + 0.0285i$. In contrast, the Poiseuille flow $\boldsymbol{U}_x = (1 - y^2)$ is linearly stable at $Re = 3000$, the selected wavenumber from the dispersion relation is $k = 1.2$ with a least stable eigenvalue $\lambda_{1B} = -0.1 + 0.38i$. Note that the first linearly unstable mode of the parallel Poiseuille appears at $Re = 5772$ for $k = 1.02$ and $\omega = 0.2639$ see for instance Schmid & Henningson (2001).

The comparison between the wake and the Poiseuille flow illustrated in Fig. 6.3 shows a clear opposite behaviour. The unstable wake becomes more and more stable as the amplitude of the most unstable eigenmode increases (Fig. 6.3(d)), while the stable Poiseuille is destabilised by an increase in the mode amplitude (Fig. 6.3(f)). It is interesting to remark the minimal change of the Poiseuille profile (Fig. 6.3(e)) between the base flow and the increasingly unstable instantaneous mean flow, probably related to the high sensitivity of the non-normal linear operator $\mathcal{L}$ as reported by Bottaro *et al.* (2003), while for the wake the mean flow modification is significant (Fig. 6.3(c)). It is very important to highlight that the coupling of the most unstable eigenmode $\boldsymbol{u}_1$ in the stable Poiseuille is equivalent to couple the optimal response to forcing at each stage, since the most unstable eigenmode and the optimal response are practically the same as can be seen in Fig. 6.4(c,d).The frequency of the most unstable eigenmode also coincides with the optimal forcing frequency (Fig. 6.4(b)). Furthermore, as seen in Chapter 5 the structure of the response to white noise can be well approximated by the optimal response, therefore, in this context, approximating the full fluctuation by the most unstable eigenmode $\boldsymbol{u}_1$ provides a good estimation of the structure that would appear when forcing the flow with white noise. The evolution of the optimal gain is depicted in Fig. 6.4(a) presenting a very pronounced increase with the fluctuating amplitude. The presented results suggest the following physical picture for flows like Poiseuille, in which the Reynolds stresses are destabilising: the background noise generates a response that modifies the mean flow through the Reynolds stress, and make it more unstable increasing the gain and thus the response to background noise and hence destabilising it further.

Contrary to the plane Poiseuille case, there are stable flows like plane Couette flow that do not present a bifurcation point at finite control parameter, and thus do not exhibit any preferred mode but are victim of stronger non-normality. Therefore, the nonlinear fluctuation, which is a response to a presumably white noise excitation, cannot be approximated by the linearly most unstable mode, and should instead be approximated by a stochastic linear response, in the spirit of the existing works of Farrell & Ioannou (2012); Thomas *et al.* (2014). In the context of the self-consistent model this stochastic response could in turn be approximated by a sum of modes at different frequencies as introduced in Chapter 5. Whether this approximation would hold for flows with no preferred mode, and the generality of the presented hypothesis remain open questions and a promising research perspective.
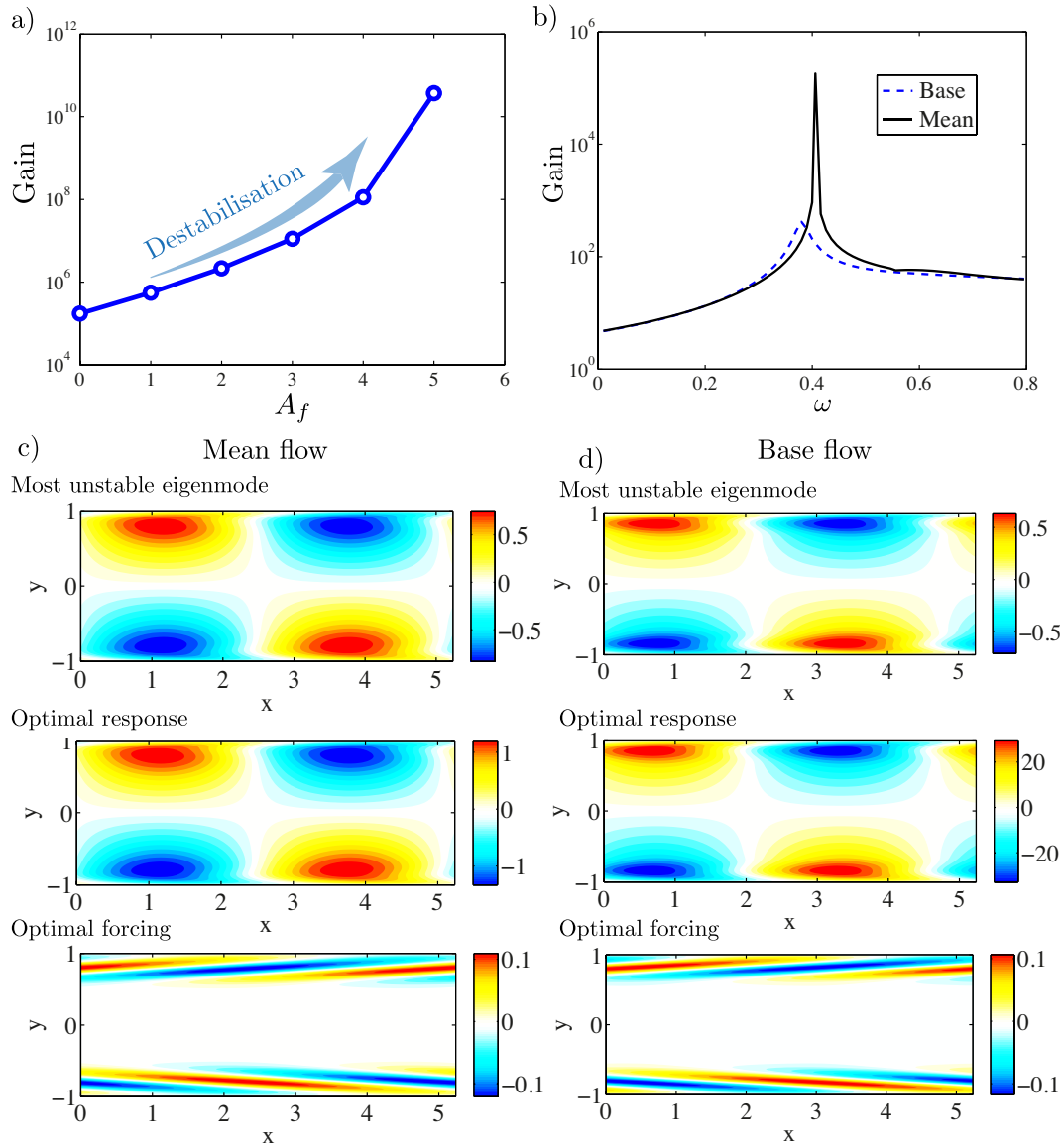
Figure 6.4 – (a) For the Poiseuille stable case, the optimal gain increases with an increase of the Reynolds stress amplitude A_f . (b) Optimal gain as function of the forcing frequency ω, comparing the base flow and mean flow. Comparison of the most unstable eigenmode, the optimal response $\boldsymbol{u}_1$ and the optimal forcing of the x-component for the mean flow (c) and the base flow (d). Plane Poiseuille flow for $k = 1.2$ and $Re = 3000$.

7 Conclusions and future perspectives

This thesis formalises a simplified physical description that accurately accounts for the non-linear saturation of the instability in unstable flows as well as the saturation of the response to disturbances in stable flows. A semi-linear or self-consistent model (SC) is introduced inspired by the weakly nonlinear analysis and mainly by the works of Stuart (1960); Sipp & Lebedev (2007); Pier & Huerre (2001); Farrell & Ioannou (2003); Barkley (2006), in an attempt to generalise the existing descriptions close to threshold (Stuart (1958, 1960); Waleffe (1995))

The model consists of the mean flow equation coupled to the linear fluctuation through the Reynolds stress divergence, which is solved iteratively. One of the fundamental aspects behind the present model is that the full nonlinear fluctuating motion is approximated by a linear equation. This simplification is encountered in other works where non-linear dynamics of flows are studied as well (Farrell & Ioannou (2003, 2012); Beaume *et al.* (2015); Thomas *et al.* (2014)). The model provides a simple description of the saturation mechanism for oscillators and amplifiers and quantitatively predicts the saturated amplitude and flow fields, *a priori*, without resorting to any numerical or experimental data in contrast to, for example, standard stability around mean flows. Thus, the self-consistent model describes the physical picture of the nonlinear interaction between the fluctuating fields and the mean flow, where the fluctuation, approximated linearly, grows around the mean flow and modifies it by the Reynolds stress forcing. This mean flow modification reduces the fluctuation growth until it saturates in a limit cycle.

The model is successfully applied to an oscillator, the unstable laminar cylinder wake, describing even the fully nonlinear dynamics of the saturation process. Furthermore, the model is also applied to an amplifier, the backward-facing step, describing the saturation of the response to harmonic and stochastic forcing. Despite the difference in the dynamics of oscillators and amplifiers, similar saturation dynamics appear to happen in both cases. The present model is in no way envisioned as a substitute for the Direct Numerical Simulations; instead, its significance lies in the clarification and formalisation of all the essential ingredients to provide a fairly accurate description of the physics.

It remains to be seen whether the present semi-linear model works also for other oscillators and amplifiers which would generalise the ideas and concepts behind the non-linear saturation process as suggested in this work. The flows studied herein are all two-dimensional although there is not any restriction for the model to be conceptually expanded to three-dimensional problems. As a simplified first attempt, periodic boundary conditions can be used in the third dimension with Fourier expansion, since the linearity of the fluctuation allows the treatment of each wave number independently. In general, it would be very interesting to address different flow configurations and geometries, like the flow behind airfoils, shear layers, boundary layers, or axisymmetric geometries like jets, nozzles, etc.

In the case of unstable oscillators, the model in principle should be able to describe any quasi-monochromatic fluctuations. However, it would be interesting to try to expand the model to account for different harmonics that could describe the dynamics of oscillators with broad band temporal spectrum. In addition, the study of the response to noise can be enhanced by including higher harmonics for cases where the linear approximation of the response to forcing fails.

Regarding turbulence, the model can be generalised by applying scale separation to the description of the coherent fluctuations in turbulent flows, that are typical, for example, in turbulent wakes.

A preliminary study of the model in the stable Poiseuille flow shows that there are certain flows for which the Reynolds stress nonlinearity is destabilising the flow, in contrast to the wake and backward-facing step. This suggests a classification of flows as Reynolds stress stabilising or destabilising and has a natural link with the supercritical/subcritical bifurcation classification. Thus, it is of interest to extend the preliminary study presented of the self-consistent model to the dynamics of the coherent structures that appear during the transition to turbulence in Poiseuille (Tuckerman *et al.* (2014)) and Couette flows, as Rolls and Streaks, in the same spirit as the works performed with other semi-linear theories, e.g. Farrell & Ioannou (2012); Thomas *et al.* (2014); Beaume *et al.* (2015), which would shed some light on the nonlinear dynamics that come into play during the transition.

As a final note, the self-consistent model sets a new framework for the linearisation around the mean flow, where the influence of the fluctuation and the mean flow modification are taken into account in the coupled equations, which eventually can be useful in optimisation and control. Furthermore, the self-consistent model may open new possibilities as a model reduction for flow control, since the coupled mean flow-perturbation equations are solved as a closed system independent of time.

A Critical aspects of the self-consistent model

As described in Chapters 2, 3, 4, the self-consistent model consists in a coupled set of equations that have to be solved iteratively through a double nested iterative loop.

Inner loop: Equation coupling for fixed A. For a chosen amplitude A of the fluctuations, there is an inner loop that couples both equations: mean flow and perturbation.

Outer loop: Amplitude A^*. It parametrises the evolution of the instantaneous mean along the external parameter amplitude A in Chapter 3 or represents the external forcing strength in Chapter 4.

In the case of amplifiers the inner loop can be replaced by a pseudo time integration, for any arbitrarily large final amplitude A of the outer loop, for details see Section 4.5.1. Different initial conditions and iterative procedures have been tried, always converging to the same mean flow and fluctuation solution, showing that the solution to the coupled system is robust and not path dependent. However, the iterative coupling of this system of equations does not come without difficulties, which are discussed below.

A.1 Sensitivity of the model

The fact that the model describes unsteady dynamics of flows that are strongly advected downstream by coupling two steady equations, strongly restricts the solution of the unsteady dynamical system in steady equations. This restriction for steady solutions creates a very sensitive setting for the iterative process, hindering its convergence.

This sensitivity is clear since it requires the use of a relaxation factor γ when coupling the inner loop as described in details in Tab. 3.2, see Chapters 2, 3 and 4 for more details. In addition, the steps in amplitude A of the outer loop are also restricted and related to the relaxation factor γ. Thus, the relaxation factor γ and amplitude A can be varied to ensure quick convergence to the correct solution that couples both equations of the model, and to overcome the oscillations and other difficulties that might appear.

Appendix A. Critical aspects of the self-consistent model

As described in Section 3.4 there is a clear increase in difficulty to attain convergence for an increasing Reynolds number, enforcing a reduction of the relaxation factor γ and increasing the number of iterations. Eventually, at $Re = 120$ the model did not converge. Similar difficulties of converging to steady solutions of the NSE for an increasing Re have been previously reported (Fornberg (1980)). Furthermore, in the backward-facing step problem, a limitation in the amplitude of the forcing was also encountered; see details in Section 4.5.1. The reasons for this increase in difficulty could be interpreted by two related factors:

- First, the sensitivity of the linear $\mathscr{L}$ and nonlinear $\mathscr{N}$ operators to disturbances as described in Section 1.2;

- Second, the similarity of the structures of the Reynolds stress forcing which are solutions of the coupled system at increasing amplitude as can be seen in Fig. 3.3.

Due to these two factors, as the Reynolds number increases together with the amplitude of the fluctuation, the coupled system is locking itself into a nonlinear solution that is more and more sensitive to variations in its structure, thus making it more and more difficult to obtain a converged solution. In order to avoid this locking, a pseudo time was introduced, as described in Section 4.5.1. However, it can only be used in amplifiers where the flow is linearly stable. In addition, the high sensitivity of the Reynolds stress forcing with a very fine structure suggests a need of a very fine mesh to approximate correctly the space derivatives. Therefore, the source of the problem could be attributed to the approach presented to solve the coupled equations or the nature of the equations itself, which may produce an ill posed problem that is difficult to solve numerically even though a physical and mathematical solution should exist. It is possible (and desired) that a different method or approach to solve the coupled equations might allow to a more robust, quick and efficient solution solving the issue of large number of iterations at high Reynolds number, or the amplitude restriction of the forcing.

The described problems can be a drawback when implementing the model in different flows, as a certain tuning and familiarisation of the iterative procedure for each flow configuration is required and in certain cases the sensitivity of the coupled system might prevent the model from converging. As an example, the attempt of Turton *et al.* (2015) to implement the model to describe the dynamics of the thermosolutal convection for a linearly marginally stable mean flow was unsuccessful.

A.2   Reynolds stress forcing normalisation

It is important to emphasise another relevant restriction, which is related to the normalisation of the Reynolds stress as discussed in Section 3.4. For oscillators such as the cylinder wake, the inner iterative loop converges robustly to a solution if the system is controlled by fixing the amplitude of the Reynolds stress forcing $A_f \equiv A^2 \|2\Re\left(\left(\bar{\boldsymbol{u}}_1 \cdot \nabla\right)\boldsymbol{u}_1\right)\|$ instead of the amplitude A of the perturbation.

Most unstable eigenmode
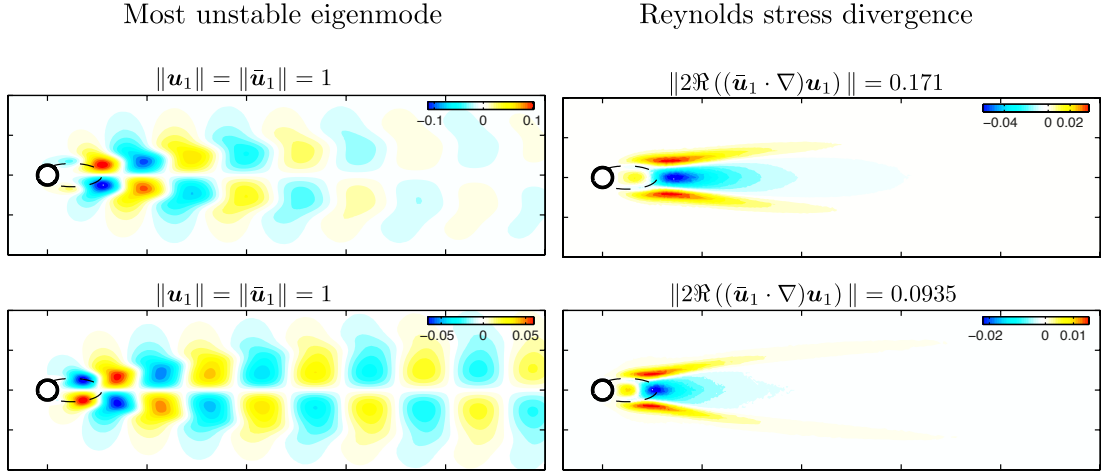
Reynolds stress divergence

Figure A.1 – Comparison of the unstable eigenmode $\boldsymbol{u}_1$ and the Reynolds stress divergence in the x-direction for two different steps during the iterations to converge to the solution of the self-consistent model for the cylinder flow at $Re = 100$. The modes are both normalised as $\|\boldsymbol{u}_1\| = 1$ and show how very similar structures of the Reynolds stress divergence yield very different norms due to the derivatives involved in the advective term $\cdot\nabla$.

To explain this idea in depth, let us imagine that one naively controls the system convergence by the amplitude A of the approximated fluctuation by the unstable eigenmode $\boldsymbol{u}' \sim A\boldsymbol{u}_1 e^{i\omega t} +$ $cc.$, with $\boldsymbol{u}_1$ of unit L^2 norm determined by the Hermitian inner product $(\boldsymbol{a}|\boldsymbol{b}) = \int_\Omega \overline{\boldsymbol{a}} \cdot \boldsymbol{b} d\Omega = \int_\Omega \boldsymbol{a}^H \cdot \boldsymbol{b} d\Omega$, for complex fields in the domain Ω, and where $cc.$ is the complex conjugate.

For a fixed amplitude A the convergence of the inner loop consists in computing the Reynolds stress divergence $A^2 2\Re((\overline{\boldsymbol{u}}_1 \cdot \nabla)\boldsymbol{u}_1)$, which forces and modifies the mean flow in each iteration, see Tab. 3.2, and updating the modified mean flow into the linear equation. Thus, between each iteration the mean flow $\boldsymbol{U}^n$ and thus the most unstable eigenmode $\boldsymbol{u}_1$ have different structures. This different structures imply that for a fixed amplitude A and normalised mode $\boldsymbol{u}_1$ the Reynolds stress forcing varies its norm in each iteration and thus changes the strength with which it forces the mean flow $\boldsymbol{U}$. This variation of Reynolds stress forcing for a fixed norm $\boldsymbol{u}_1$ can be seen in Fig. A.1, where for two very similar structures of the normalised mode $\boldsymbol{u}_1$ and Reynolds stress divergence, the norm of the Reynolds stress forcing varies drastically, in a manner similar to that encountered between iterations. The variation in the norm is related to the spatial derivatives included in the advective term $\cdot\nabla$ in the Reynolds stress divergence $2\|\Re((\overline{\boldsymbol{u}}_1 \cdot \nabla)\boldsymbol{u}_1)\|$; although it scales as $\propto \|\boldsymbol{u}_1\|^2$ its exact value depends strongly on the spatial distribution of the eigenmode $\boldsymbol{u}_1$. Summarising, a fixed amplitude A implies a variation of the norm of the forcing in the mean flow equation on top of a variation in its spatial shape at each iterative step, which was found to result in a destabilising effect in the iterative process.

One way to prevent these oscillations in the forcing of the mean flow is to control the forcing amplitude by the amplitude of the Reynolds stress forcing A_f, which is related to the amplitude

of the mode as

$$A_f \frac{2\Re\left((\bar{\boldsymbol{u}}_1 \cdot \nabla)\boldsymbol{u}_1\right)}{\|2\Re\left((\bar{\boldsymbol{u}}_1 \cdot \nabla)\boldsymbol{u}_1\right)\|} = A^2 2\Re\left((\bar{\boldsymbol{u}}_1 \cdot \nabla)\boldsymbol{u}_1\right), \tag{A.1}$$

for a normalised mode $\|\boldsymbol{u}_1\| = 1$. Fixing A_f, the norm of the RHS of the mean flow equation is kept constant despite the changes in the structure of $\boldsymbol{u}_1$. It should be highlighted that this change in normalisation of the Reynolds stress forcing does not have any influence on the physics of the results, since there is a unique relation between A and A_f for the converged system at a given A_f as the mode structure $\boldsymbol{u}_1$ is unique thus fixing the relation (A.1).

A.3   Model algorithmic convergence and limitations

The relaxation factor γ and the steps in amplitude A_f are two parameters that can be varied to ensure a quick and stable convergence of the double iterative procedure to close the coupled equations of the self-consistent model, leading to two distinct approaches for enhanced converging speed:

- Large steps δA_f in the amplitude A_f in the outer loop and small relaxation factor γ in the inner loop as described in Fig. A.2(a).

- Small steps δA_f in the amplitude A_f of the outer loop large relaxation factor, soft damping in the inner loop as described in Fig. A.2(b).

Both procedures are illustrated in Fig. A.2 for the residual convergence during one step in the outer loop or amplitude δA_f. Their comparison shows that the most efficient approach is to use a large amplitude stepping δA_f of the outer loop with a strong relaxation factor γ in the inner loop. Since a step in $\delta A_f = 1e^{-3}$ of Fig. A.2(a) converges approximately with the same number of iterations as in Fig. A.2(b) for a step 10 times smaller, $\delta A_f = 1e^{-4}$.

Newton-Raphson method for the non-linear mean flow equation

The amplitude steps δA_f are bounded by the convergence capability of the Newton-Raphson method of the nonlinear mean flow equation for a given Reynolds stress (which acts as forcing) amplitude A_f which is related directly to the forcing amplitude through the perturbation equation. There is a maximum amplitude of the forcing (and therefore of the Reynolds stress) for which the Newton-Raphson method converges in the mean flow equation. Picard's method for nonlinear mean flow equation works worse than a Newton-Raphson scheme and converges much more slowly, and for smaller amplitude steps ceases to converge. An internal amplitude loop was attempted inside the Newton method loop to be able to converge for larger amplitudes. However, it was found, since an increase of less than 50% of the threshold amplitude step δA could be achieved. Therefore, having in mind the complexity of the automatic internal amplitude loop in the Newton-Raphson method in the mean flow equation
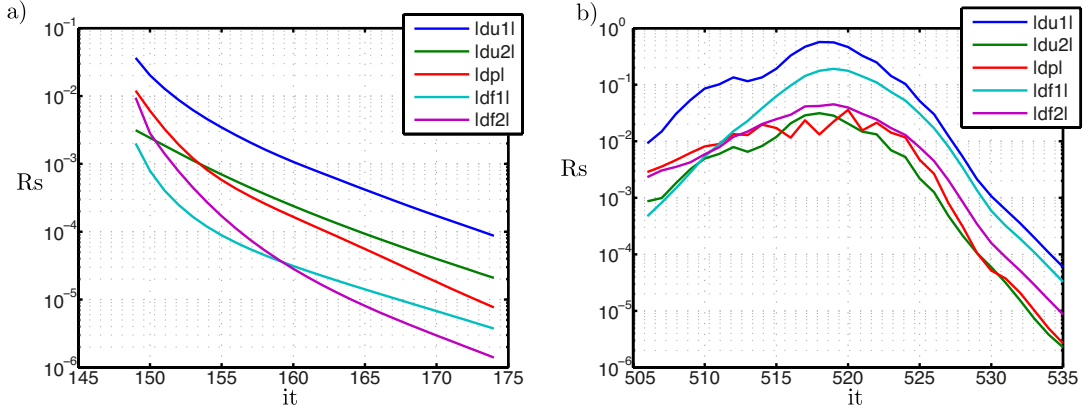
Figure A.2 – Residuals for different forcing amplitude steps and relaxation factors, for the step flow described in Chapter 4 at $Re = 500$. a) Forcing $A_f = 1.5e^{-3}, \gamma = 0.2$, amplitude step is $\delta A_f = 1e^{-3}$, b) Forcing $A_f = 1.5e^{-3}, \gamma = 0.8$ and amplitude step $\delta A_f = 1e^{-4}$.

and the lack of robustness, including a much higher computational time, does not justify a slightly larger amplitude steps δA_f in the outer loop. An extra relaxation factor inside the Newton Raphson method of the mean flow equation, does not allow either for a relevant increase in the amplitude step δA_f, allowing only for a very slight increase in the amplitude step δA_f while entailing a huge cost in computational time.

Amplitude step δA_f

Probably the problem of not being able to converge the mean flow equation for higher amplitude steps δA_f is related to the fact that the spatial structure of the Reynolds stress forcing $2\|\Re\left((\bar{\boldsymbol{u}}_1 \cdot \nabla)\boldsymbol{u}_1\right)$ is that of the previous amplitude, and therefore, it is difficult to accommodate a new velocity field $\boldsymbol{U}$ that would close the steady mean flow equation for a much larger forcing $A_f + \delta A_f$ with an incorrect structure. This explains why the cost of solving the nonlinear mean flow equation by the Newton-Raphson method increases. There is a trade off between the number of iterations required to solve the mean flow equation for higher amplitude steps δA_f and the number of iterations in the outer loop due to smaller amplitude steps.

Most efficient parameters

The relaxation factor of the inner loop γ also influences the amplitude steps δA_f of the outer loop. The relaxation factor used is the same for the convergence of the inner loop for a fixed amplitude A_f and when the amplitude is changed, $A_f + \delta A_f$, since varying the relaxation factor automatically is not convenient. Based on different tests, the most efficient way to achieve higher total amplitude A_f is to take the biggest steps in amplitude δA_f and small relaxation factor γ, to ensure that the method does not blow up quickly, Fig. A.2(a). If smaller amplitude steps are tried with higher relaxation factor, the iterative method blows up more quickly, Fig. A.2(b). The restricting parameter for the convergence in amplitude is the relaxation factor
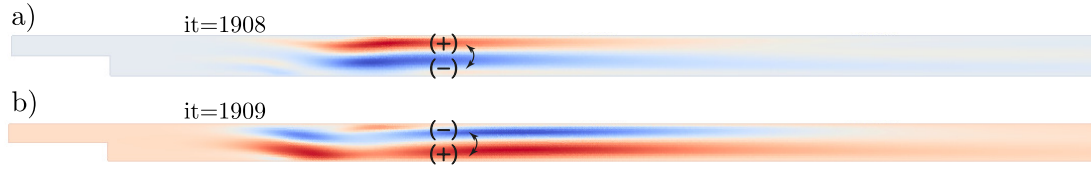
Figure A.3 – Comparison of the mean flow velocity variation $\delta U_x^n = U^n - U^{n-1}$ for two different consecutive steps a) for iteration it= 1908 and b) it= 1909. Convergece of the backward facing step flow (Chapter 4) for $A_f = 0.034, \gamma = 0.2$ and $\delta A_f = 1e^{-3}$. The steps are just the first two steps after changing amplitude from $A_f = 0.033$ to $A_f = 0.034$; this occurs at step 1907-1908.

γ, not the amplitude steps.

Comments on convergence

The problem when the coupled system of loops ceases to converge for a given forcing amplitude A_f seems to be related to the relaxation factor γ used. In the backward-facing step for example, when a step δA_f in amplitude is performed in the outer loop, the velocity field oscillates between two close solutions, as illustrated in Fig. A.3, where the velocity field of the mean flow solutions U of two consecutive iterations ($it = 1908, 1909$) are compared, just after a change in amplitude $A_f + \delta A_f$, that is to say, one step in the outer loop. Eventually, due to the relaxation factor γ, the velocity fields start to converge to a unique solution and allow the closure of the internal loop for a given amplitude A_f. When an amplitude step δA_f is performed with a given relaxation factor γ and the relaxation factor is not small enough, the method starts oscillating between two solutions, preventing the desired convergence.

Bibliography

AKERVIK, E., EHRENSTEIN, U., GALLAIRE, F. & HENNINGSON, D. S. 2008 Global two-dimensional stability measures of the flat plate boundary-layer flow. *Eur. J. Mech. B/Fluids* **27** (5), 501–513.

ALIZARD, F., CHERUBINI, S. & ROBINET, J.-C. 2009 Sensitivity and optimal forcing response in separated boundary layer flows. *Phys. Fluids* **21** (6), 064108.

BAKAS, N. A. & IOANNOU, P. J. 2011 Structural stability theory of two-dimensional fluid flow under stochastic forcing. *J. Fluid Mech.* **682**, 332–361.

BAKAS, N. A. & IOANNOU, P. J. 2014 A theory for the emergence of coherent structures in beta-plane turbulence. *J. Fluid Mech.* **740**, 312–341.

BARKLEY, D. 2006 Linear analysis of the cylinder wake mean flow. *Europhys. Lett.* **75**, 750–756.

BARKLEY, D., GOMES, M. G. M. & HENDERSON, R. D. 2002 Three-dimensional instability in flow over a backward-facing step. *J. Fluid Mech.* **473**, 167–190.

BARRÉ, S., FLEURY, V., BOGEY, C., BAILLY, C. & JUVÉ, D. 2006 Experimental study of the spectral properties of near-field and far-field jet noise. In *12th AIAA/CEAS Aeroacoustics Conf.*, , vol. 6, pp. 73–92. Cambridge Massachusetts: American institute of Aeronautics and Astronautics.

BEAUME, C., CHINI, G. P., JULIEN, K. & KNOBLOCH, E. 2015 Reduced description of exact coherent states in parallel shear flows. *Phys. Rev. E* **91**, 1–18.

BENITEZ, M. & BERMUDEZ, A. 2011 A second order characteristics finite element scheme for natural convection problems. *J. Comput. Appl. Math.* **235**, 3270–3284.

BERKOOZ, G., HOLMES, P. & LUMLEY, J. 1993 The proper orthogonal decomposition in the analysis of turbulent flows. *Annu. Rev. Fluid Mech.* **25**, 539–575.

BERS, A. 1975 Linear waves and instabilities. *Physique des Plasmas* **6**, 113–215.

BLACKBURN, H. M., BARKLEY, D. & SHERWIN, S. J. 2008 Convective instability and transient growth in flow over a backward-facing step. *J. Fluid Mech.* **603**, 271–304.

Bibliography

BOTTARO, A., CORBETT, P. & LUCHINI, P. 2003 The effect of base flow variation on flow stability. *J. Fluid Mech.* **476**, 293–302.

BOUCHET, F., NARDINI, C. & TANGARIFE, T. 2013 Kinetic theory of jet dynamics in the stochastic barotropic and 2D Navier-Stokes equations. *J. Stat. Phys.* **153** (4), 572–625.

BOUJO, E. & GALLAIRE, F. 2014 Controlled reattachment in separated flows: a variational approach to recirculation length reduction. *J. Fluid Mech.* **742**, 618–635.

BOUJO, E. & GALLAIRE, F. 2015 Sensitivity and open-loop control of stochastic response in a noise amplifier flow : the backward-facing step. *J. Fluid Mech.* **762**, 361–392.

BUTLER, K. M. & FARRELL, B. F. 1992 Three-dimensional optimal perturbations in viscous shear flow. *Phys. Fluids A* **4**, 1637–1650.

CAMARRI, S. 2015 Flow control design inspired by linear stability analysis. *Acta Mech.* **1010**, 979–1010.

CAMPBELL, L. & GARNETT, W. 1882 *The Life of James Clerk Maxwell*. London: Macmillan and Co.

CHARRU, F. 2011 *Hydrodynamic Instabilities*. Cambridge: Cambridge University Press.

CHOMAZ, J.-M. 2005 Global instabilities in spatially developing flows: Non-Normality and Nonlinearity. *Annu. Rev. Fluid Mech.* **37**, 357–392.

CHOMAZ, J.-M., HUERRE, P. & REDEKOPP, L. G. 1988 Bifrucations to local and global modes in spatially developing flows. *Phys. Rev. Lett.* **60**, 25–28.

CORBETT, P. & BOTTARO, A. 2000 Optimal perturbations for boundary layers subject to streamwise pressure gradient. *Phys. Fluids* **12** (1), 120–130.

COSSU, C., PUJALS, G. & DEPARDON, S. 2009 Optimal transient growth and very large scale structures in turbulent boundary layers. *J. Fluid Mech.* **619**, 79.

CROW, S. C. & CHAMPAGNE, F. H. 1971 Orderly structure in jet turbulence. *Journal of Fluid Mechanics* **48**, 547–591.

DERGHAM, G., SIPP, D. & ROBINET, J.-CH. 2013 Stochastic dynamics and model reduction of amplifier flows: the backward facing step flow. *J. Fluid Mech.* **719**, 406–430.

DRAZIN, P.G. & REID, W.H. 2004 *Hydrodynamic stability*, 2nd edn. Cambridge: Cambridge Univ Press.

DRAZIN, P. G. 2002 *Introduction to Hydrodynamic Stability*. Cambridge: Cambridge University Press.

DRAZIN, P. G. & REID, W. H. 1981 *Hydrodynamic Stability*. Cambridge: Cambridge University Press.

DUŠEK, J., LE GAL, P. & FRAUNIÉ, P. 1994 A numerical and theoretical study of the first Hopf bifurcation in a cylinder wake. *J. Fluid Mech.* **264**, 59–80.

EHRENSTEIN, U. & KOCH, W. 1991 Three-dimensional wavelike equilibrium states in plane poiseuille flow. *Journal of Fluid Mechanics* **228**, 111–148.

FARRELL, B. F. & IOANNOU, P. J. 1993 Stochastic forcing of the linearized Navier-Stokes equations. *Phys. Fluids A* **5**, 2600–2609.

FARRELL, B. F. & IOANNOU, P. J. 1996 Generalized stability theory. Part 1 Autonomous operators. *J. Atmos. Sci.* **53**, 2025–2040.

FARRELL, B. F. & IOANNOU, P. J. 2001 Accurate low-dimensional approximation of the linear dynamics of fluid flow. *J. Atmos. Sci.* **58**, 2771–2789.

FARRELL, B. F. & IOANNOU, P. J. 2003 Structural stability of turbulent jets. *J. Atmos. Sci.* **60** (17), 2101–2118.

FARRELL, B. F. & IOANNOU, P. J. 2007 Structure and spacing of jets in barotropic turbulence. *J. Atmos. Sci.* **64** (10), 3652–3665.

FARRELL, B. F. & IOANNOU, P. J. 2009*a* A theory of baroclinic turbulence. *J. Atmos. Sci.* **66** (8), 2444–2454.

FARRELL, B. F. & IOANNOU, P. J. 2009*b* Emergence of jets from turbulence in the shallow-water equations on an equatorial beta plane. *J. Atmos. Sci.* **66** (10), 3197–3207.

FARRELL, B. F. & IOANNOU, P. J. 2012 Dynamics of streamwise rolls and streaks in turbulent wall-bounded shear flow. *J. Fluid Mech.* **708**, 149–196.

FORNBERG, B. 1980 A numerical study of steady viscous flo w past a circular cylinder. *J. Fluid Mech.* **98**, 819–855.

GARNAUD, X. 2012 Modes , transient dynamics and forced response of circular jets. PhD thesis, Ecole Polytechnique, Palaiseau.

GARNAUD, X., LESSHAFFT, L., SCHMID, P. J. & HUERRE, P. 2013 The preferred mode of incompressible jets: linear frequency response analysis. *J. Fluid Mech.* **716**, 189–202.

GIANNETTI, F. & LUCHINI, P. 2007 Structural sensitivity of the first instability of the cylinder wake. *J. Fluid Mech.* **581**, 167–197.

GMBH, SMART BLADE 2010 Smart Blade GmbH, wikimedia commons.

GODRECHE, CLAUDE & MANNEVILLE, PAUL, ed. 1998 *Hydrodynamics and Nonlinear Instabilities*. Cambridge University Press, cambridge Books Online.

HAMMOND, D. A. & REDEKOPP, L. G. 1997 Global dynamics of symmetric and asymmetric wakes. *J. Fluid Mech.* **331**, 231–260.

Bibliography

HUERRE, P. & MONKEWITZ, P. A. 1985 Absolute and convective instabilities in free shear layers. *Journal of Fluid Mechanics* **159**, 151–168.

HUERRE, P. & MONKEWITZ, P. A. 1990 Local and global instabilities in spatially developing flows. *Annu. Rev. Fluid Mech.* **22**, 473–537.

JACKSON, C. P. 1987 A finite-element study of the onset of vortex shedding in flow past variously shaped bodies. *Journal of Fluid Mechanics* **182**, 23–45.

JOVANOVIĆ, M. R. & BAMIEH, B. 2005 Componentwise energy amplification in channel flows. *J. Fluid Mech.* **534**, 145–183.

VON KARMAN, T 1911 Über den mechanismus des widerstandes, den ein bewegter körper in einer flüssigkeit erfährt. *Göttingen Nachr. Math. Phys* **12**, 509—-517.

LANZERSTORFER, D. & KUHLMANN, H. C. 2012 Three-dimensional instability of the flow over a forward-facing step. *J. Fluid Mech.* **695**, 390–404.

MALKUS, W. V. R. 1956 Outline of a theory of turbulent shear flow. *Journal of Fluid Mechanics* **1**, 521–539.

MANTIČ-LUGO, V., ARRATIA, C. & GALLAIRE, F. 2014 Self-Consistent Mean Flow Description of the Nonlinear Saturation of the Vortex Shedding in the Cylinder Wake. *Phys. Rev. Lett.* **113**, 084501.

MANTIČ-LUGO, V., ARRATIA, C. & GALLAIRE, F. 2015 A self-consistent model for the saturation dynamics of the vortex shedding around the mean flow in the unstable cylinder wake. *Phys. Fluids* **27**, 074103.

MANTIČ-LUGO, V. & GALLAIRE, F. 2015 Self-consistent model for the saturation mechanism of the response to harmonic forcing in the backward-facing step flow. *Submitted to J. Fluid Mech.* .

MARQUET, O., LOMBARDI, M., CHOMAZ, J.-M., SIPP, D. & JACQUIN, L. 2009 Direct and adjoint global modes of a recirculation bubble: lift-up and convective non-normalities. *J. Fluid Mech.* **622**, 1–21.

MARQUET, O. & SIPP, D. 2010 Global sustained perturbations in a backward-facing step flow. *IUTAM Bookseries*, vol. 18. Dordrecht: Springer Netherlands.

MARQUET, O, SIPP, D & JACQUIN, L 2008 Sensitivity analysis and passive control of cylinder flows. *J. Fluid Mech.* **615**, 221–252.

MARQUET, O., SIPP, D. & LESSHAFFT, L. 2010 Global stability analysis of open shear flows without global modes. *Tech. Rep.*.

MAUREL, A., PAGNEUX, V. & WESFREID, J. E. 1995 Mean-flow correction as non-linear saturation mechanism. *Europhys. Lett.* **32**, 217–222.

MELIGA, P., CHOMAZ, J.-M. & SIPP, D. 2009*a* Global mode interaction and pattern selection in the wake of a disk: a weakly nonlinear expansion. *J. Fluid Mech.* **633**, 159–189.

MELIGA, P., CHOMAZ, J. M. & SIPP, D. 2009*b* Unsteadiness in the wake of disks and spheres: Instability, receptivity and control using direct and adjoint global stability analyses. *J. Fluids Struct.* **25**, 601–616.

MELIGA, P., PUJALS, G. & SERRE, E. 2012 Sensitivity of 2-D turbulent flow past a D-shaped cylinder using global stability. *Phys. Fluids* **24**, 061701.

MELIGA, P., SIPP, D. & CHOMAZ, J.-M. 2009*c* Elephant modes and low frequency unsteadiness in a high Reynolds number, transonic afterbody wake. *Phys. Fluids* **21**, 054105.

MITTAL, S. 2008 Global linear stability analysis of time-averaged flows. *Int. J. Numer. Methods Fluids* **58**, 111–118.

MONOKROUSOS, A., AKERVIK, E., BRANDT, L. & HENNINGSON, D. S. 2010 Global three-dimensional optimal disturbances in the Blasius boundary-layer flow using time-steppers. *J. Fluid Mech.* **650**, 181–214.

NAZARENKO, S., KEVLAHAN, N. K. & DUBRULLE, B. 2000 Nonlinear RDT theory of near-wall turbulence. *Phys. D* **139**, 158–176.

NICHOLS, J. & LELE, S. 2010 Global mode analysis of turbulent high-speed jets. *Annu. Res. Briefs* .

NOACK, B. R., AFANASIEV, K., MORZYNSKI, M., TADMOR, G. & THIELE, F. 2003 A hierarchy of low-dimensional models for the transient and post-transient cylinder wake. *J. Fluid Mech.* **497**, 335–363.

NOIRAY, N., DUROX, D., SCHULLER, T. & CANDEL, S. 2008 A unified framework for nonlinear combustion instability analysis based on the flame describing function. *J. Fluid Mech.* **615**, 139–167.

PIER, B. 2002 On the frequency selection of finite-amplitude vortex shedding in the cylinder wake. *J. Fluid Mech.* **458**, 407–417.

PIER, B. & HUERRE, P. 1998 Fully nonlinear global modes in spatially developing media. *Phys. Fluids* **10**, 2433–2435.

PIER, B. & HUERRE, P. 2001 Nonlinear self-sustained structures and fronts in spatially developing wake flows. *J. Fluid Mech.* **435**, 145–174.

POPE, S. B. 2000 *Turbulent Flows*. Cambridge University Press.

PRESS, W. H., TEUKOLSKY, S. A., VETTERLING, W. T. & FLANNERY, B. P. 2007 *Numerical Recipes 3rd Edition: The Art of Scientific Computing*, , vol. 1. Cambridge: Cambridge University Press.

Bibliography

PROVANSAL, M., MATHIS, C. & BOYER, L. 1987 Bénard-von kámán instability: transient and forced regimes. *Journal of Fluid Mechanics* **182**, 1–22.

REYNOLDS, W.C. & HUSSAIN, A. K. M. F. 1972 The mechanism of an organized wave in turbulent shear flow. Part 3. Theoretical models and comparison with experiments. *J. Fluid Mech.* **54**, 263–288.

SCHMID, P. J. 2007 Nonmodal Stability Theory. *Annu. Rev. Fluid Mech.* **39**, 129–162.

SCHMID, P. J. & HENNINGSON, D. S. 2001 *Stability and transition in shear flows.* Springer.

SCHNEIDER, T. M., GIBSON, J. F. & BURKE, J. 2010 Snakes and ladders: Localized solutions of plane couette flow. *Phys. Rev. Lett.* **104**, 1–4.

SIPP, D. & LEBEDEV, AN. 2007 Global stability of base and mean flows: a general approach and its applications to cylinder and open cavity flows. *J. Fluid Mech.* **593**, 333–358.

SIPP, D. & MARQUET, O. 2012 Characterization of noise amplifiers with global singular modes: the case of the leading-edge flat-plate boundary layer. *Theor. Comput. Fluid Dyn.* **27**, 1–19.

STRYKOWSKI, P. J. & SREENIVASAN, K. R. 1990 On the formation and suppression of vortex shedding at low Reynolds numbers. *J. Fluid Mech.* **218**, 71–107.

STUART, J. T. 1958 On the non-linear mechanics of hydrodynamic stability. *Journal of Fluid Mechanics* **4**, 1–21.

STUART, J. T. 1960 On the non-linear mechanics of wave disturbances in stable and unstable parallel flows. Part 1. The basic behaviour in plane Poiseuille flow. *J. Fluid Mech.* **9**, 353–370.

TADMOR, G., LEHMANN, O., NOACK, B. R., CORDIER, L., DELVILLE, J., BONNET, J.-P. & MORZYŃSKI, MAREK 2011 Reduced-order models for closed-loop wake control. *Philos. Trans. A. Math. Phys. Eng. Sci.* **369**, 1513–24.

TADMOR, G., LEHMANN, O., NOACK, B. R. & MORZYNSKI, M. 2010 Mean field representation of the natural and actuated cylinder wake. *Phys. Fluids* **22**, 034102.

THEOFILIS, V. 2011 Global Linear Instability. *Annu. Rev. Fluid Mech.* **43**, 319–352.

THIRIA, B., BOUCHET, G. & WESFREID, J. E. 2015 On the relation between linear stability analysis and mean flow properties in wakes. *arXiv* .

THIRIA, B. & WESFREID, J. E. 2009 Physics of temporal forcing in wakes. *J. Fluids Struct.* **25**, 654–665.

THOMAS, V. L., LIEU, B. K., JOVANOVIĆ, M. R., FARRELL, B. F., IOANNOU, P. J. & GAYME, DENNICE F. 2014 Self-sustaining turbulence in a restricted nonlinear model of plane Couette flow. *Phys. Fluids* **26**, 105112.

TREFETHEN, L. N., TREFETHEN, A. E., REDDY, S. C. & DRISCOLL, T. A. 1993 Hydrodynamic Stability Without Eigenvalues. *Science* **261**, 578–584.

TRIANTAFYLLOU, G. S., TRIANTAFYLLOU, M. S. & CHRYSSOSTOMIDIS, C. 1986 On the formation of vortex streets behind stationary cylinders. *Journal of Fluid Mechanics* **170**, 461–477.

TUCKERMAN, L. S., KREILOS, T., SCHROBSDORFF, H., SCHNEIDER, T. M. & GIBSON, J. F. 2014 Turbulent-laminar patterns in plane Poiseuille flow. *Phys. Fluids* **26**, 1–11.

TURTON, S. E., T., LAURETTE S. & BARKLEY, D. 2015 Prediction of frequencies in thermosolutal convection from mean flows. *Phys. Rev. E* **91**, 043009.

VAN DYKE, M. 1988 *An Album of Fluid Motion.* Stanford: The Parabolic Press.

VIOLA, F., IUNGO, G. V., CAMARRI, S., PORTÉ-AGEL, F. & GALLAIRE, F. 2014 Prediction of the hub vortex instability in a wind turbine wake: stability analysis with eddy-viscosity models calibrated on wind tunnel data. *J. Fluid Mech.* **750**, R1.

WALEFFE, F. 1995 Transition in shear flows. Nonlinear normality versus non-normal linearity. *Phys. Fluids* **7**, 3060–3066.

WALEFFE, F. 1997 On a self-sustaining process in shear flows. *Phys. Fluids* **9** (4), 883–900.

WERLE, H. 1980 *La Recherche Aérospatiale* **5**, 35–49.

WILLIAMSON, C. H. K. 1988 Defining a universal and continuous Strouhal-Reynolds number relationship for the laminar vortex shedding of a circular cylinder. *Phys. Fluids* **31** (10), 2742–2744.

ZAOUALI, Y., JAY, J. & AISSIA, H. B. 2009 Etude Experimentale des Instabilites dans un Jet Rond Evouant a Bas Nombre de Reynolds. *Leban. Sci. J.* **10**, 63–76.

ZEBIB, A. 1987 Stability of viscous flow past a circular cylinder. *J. Eng. Math.* **21**, 155–165.

ZIELINSKA, B., GOUJON-DURAND, S., DUSEK, J. & WESFREID, J. 1997 Strongly Nonlinear Effect in Unstable Wakes. *Phys. Rev. Lett.* **79**, 3893–3896.

Vladislav Mantič-Lugo

Personal information

Nationality: **Cuban, Slovak, Spanish**.

Birth: **La Habana, 25 March 1987**.

Education

2011–2015 **Ph.D. in mechanical engineering**, *EPFL, Lausanne, Swizerland*
Laboratory of Fluid Mechanics and Instabilities,
Thesis title: "Too Big to Grow: Self-Consistent Model for Nonlinear Saturation
in Open Shear Flows,"
under the supervision of Prof. F. Gallaire.

2009–2010 **MSc Thermal Power, Aerospace Propulsion**, *Cranfield University, UK*,
(awarded Director's Price)
Part of a double degree program
Thesis title: "Effects of Boundary Layer Ingestion and Thrust Vectoring in
Distributed Propulsion",
under the supervision of Dr. G. Doulgeris and Prof. R. Singh.

2005–2010 **MEng Aeronautical Engineering, Option: Aircrafts**, *University of
Seville*.

2004–2009 **Professional Conservatory: piano**, *Music Conservatory Francisco Guerrero*,
Seville.

2005 **High School diploma**, *Colegio Compañía de María*, Seville.

Work Experience

2011 **Center for Advanced Aerospace Technologies (FADA CATEC)**, *Seville*,
(Internship).

2011 **University of Seville**, *Group of Elasticity and Strength of Materials*,
(Researcher).

2009–2010 **Rolls Royce**, *UTC group in Cranfield University*, (Internship).

Languages

Spanish (Native), Slovak (Native), English (Fluent), French (B2)

2005 **Physics Olympiad**, National silver medal, Spain.

2005 **Mathematics Olympiad**, Regional silver medal, Spain.

2005 **1st prize engineering contest**, School of Engineering, University of Seville.

Teaching

2011–2015 **EPFL**, *Fluid flow*, teaching assistant.

2012–2015 **EPFL**, *Hydrodynamics*, teaching assistant.

Publications

V Mantič-Lugo and F Gallaire. Self-consistent model for the saturation mechanism of the response to harmonic forcing in the backward-facing step flow. *Submitted to J. Fluid Mech.*, 2015.

V Mantič-Lugo, C Arratia and F Gallaire. A self-consistent model for the saturation dynamics of the vortex shedding around the mean flow in the unstable cylinder wake. *Phys. Fluids*, 27(7):074103, 2015.

V Mantič-Lugo, C Arratia and F Gallaire. Self-Consistent Mean Flow Description of the Nonlinear Saturation of the Vortex Shedding in the Cylinder Wake. *Phys. Rev. Lett.*, 113(8):084501, 2014.

V Mantič-Lugo, G Doulgeris and R Singh. Computational analysis of the effects of a boundary layer ingesting propulsion system in transonic flow. *Proceedings of the Institution of Mechanical Engineers, Part G: Journal of Aerospace Engineering*, 227(8):1215–1232, 2013.

V Mantič-Lugo, L J Gray, V Mantič, E Graciani and F París. A Galerkin projection technique for the evaluation of potential derivatives on a smooth boundary in 2D BEM. *Eng. Anal. Bound. Elem.*, 36:1502–1512, 2012.

V Mantič-Lugo, G Doulgeris, A Gohardani and R Singh. Computational analysis of the aerodynamic performance of a jet-flap airfoil in transonic flow. *Proceedings of the Institution of Mechanical Engineers, Part G: Journal of Aerospace Engineering*, 226(6):664–678, 2012.

V Mantič-Lugo, L J Gray, V Mantič, E Graciani and F París. Galerkin projection for the potential gradient recovery on the boundary in 2D BEM. In Ch Zhang, M H Aliabadi, M Schanz (Eds.), *Proc. Int. Conf. Advances in Boundary Element Techniques XI*, 298–305, 2010.